New Probes and Targets for Hypoxia Imaging

by

Babak Moghadas

A Dissertation Presented in Partial Fulfillment
of the Requirements for the Degree
Doctor of Philosophy

Approved April 2021 by the
Graduate Supervisory Committee:

Vikram Kodibagkar , Chair
Scott Beeman
Jitendran Muthuswamy
Mehdi Nikkhah
Gregory Turner

ARIZONA STATE UNIVERSITY

August 2021

ABSTRACT

Magnetic resonance imaging (MRI) is a noninvasive imaging modality, which is used for many different applications. The versatility of MRI is in acquiring high resolution anatomical and functional images with no use of ionizing radiation. The contrast in MR images can be engineered by two different mechanisms with imaging parameters (TR, TE, α) and/or contrast agents. The contrast in the former is influenced by the intrinsic properties of the tissue (T_1, T_2, ρ), while the contrast agents change the relaxation rate of the protons to enhance contrast. Contrast agents have attracted a lot of attention because they can be modified with targeting groups to shed light on some physiological and biological questions, such as the presence of hypoxia in a tissue. Hypoxia, defined as lack of oxygen, has many known ramifications on the outcome of therapy in any condition. Hence its study is very important. The standard gold method to detect hypoxia, immunohistochemical (IHC) staining of pimonidazole, is invasive; however, there are many research groups focused on developing new and mainly noninvasive methods to investigate hypoxia in different tissues.

Previously, a novel nitroimidazole-based T_1 contrast agent, gadolinium tetraazacyclododecanetetraacetic acid monoamide conjugate of 2-nitroimidazole (GdDO3NI), has been synthesized and characterized on subcutaneous prostate and lung tumor models. Here, its efficacy and performance on traumatic brain injuries and brain tumors are studied. The pharmacokinetic properties of the contrast agent the perfusion properties of brain tumors are investigated. These results can be used in personalized therapies for more effective results for patients.

Gadolinium (Gd), which is a strongly paramagnetic heavy metal, is routinely and widely used as an MR contrast agent by chelation with a biocompatible ligand which is typically cleared through the kidneys. While widely used, there are serious concerns for patients with impaired kidney function, as well as recent studies showed Gd accumulation in the bone and brain. Iron as a physiological ion is also capable of generating contrast in MR images. Here synthesis and characterization of an iron-based hypoxia targeting contrast agent is proposed to eliminate Gd-related complications and provide a cheaper and more economical alternative contrast agent to detect hypoxia.

DEDICATION

I dedicate this dissertation to my family especially my mother; without her love, support, and sacrifice I would not have been able to come this far.

ACKNOWLEDGEMENTS

I would like to thank the many who helped me in improving my scientific career and personal life to make a better version of myself over the past 4.5 years of my Ph.D. journey. Firstly, I would like to express my special appreciation and thanks to my advisor Dr. Kodibagkar. The man who gave me the opportunity to grow, the man who taught me a lot in science and how to conduct impactful research. I want to thank my dissertation committee members Dr. Scott Beeman, Dr. Jitendran Muthuswamy, Dr. Mehdi Nikkhah, Dr. Gregory Turner for serving as my committee members, and their invaluable input in my research. I want to thank Dr. Sarah Stabenfeldt, Dr. Chad Quarles, Dr. Matthew Green, Dr. Ryan Trovitch, Dr. Yanqing Tian, Dr. Brian Cherry and Dr. Samrat Amin for their help, scientific input and contributions in my research. I would especially like to thank Crystal Willingham, Alberto Fuentes, Debbie Healey and Xiaowei Zhang for their help in data collection and for teaching me the required skills over the course of my PhD. I want to thank Dr. Erfan Dashtimoghadam, Dr. Shubhangi Agarwal, Dr. Vimala Bharadwaj, Dr. Chris Rock, Dr. Munish Chauhan and Dr. Matthew Scarpelli for their help, support, and everything they taught me. I would like to thank my lab members Dr. Nutandev Bikkamane Jayadev, Sulagna Sahu, Yuka Sugamura and Talia Hertzberg. A sincere thanks to SBHSE and ASU, especially Ms. Laura Hawes, Ms. Tamera Cameroon, and Ms. Tomi St. John, for being supportive.

Lastly, and most importantly, I would like to thank my family and my friends (my chosen family). They provide me with the motivation and energy to explore and find the best version of myself.

TABLE OF CONTENT

Page

LIST OF TABLES.....vii

LIST OF FIGURES.....ix

CHAPTER

INTRODUCTION ON TISSUE HYPOXIA AND ITS DETECTION METHODS.....1

1. Introduction……...1

2. Tissue microenvironment……..2

2.1. Oxygen and Tissue Hypoxia.....2

2.2. Importance of Hypoxia, and Techniques to Study Tissue Oxygenation 5

3. Nitroimidazole and hypoxia……..7

4. Magnetic Resonance Imaging……...9

4.1. T_1, T_2, T_2^* Relaxation Mechanisms 11

4.2. Paramagnetic Relaxation 12

4.3. Targeting MR Contrast Agents.....15

ASSESSMENT OF HYPOXIA IN TRAUMATIC BRAIN INJURY USING HYPOXIA TARGETING CONTRAST AGENT.....18

1. Introduction…….19

2. Materials and Methods……22

2.1. Materials 22

CHAPTER Page

2.2. Animal Preparation 23

2.3. Magnetic Resonance Imaging 23

2.4. Data Processing 24

2.5. Statistics 25

2.6. Tissue Collection 25

2.7. Histology and Immunohistochemistry 26

3. Results…….27

4. Discussion and Conclusions……36

ASSESSMENT OF HYPOXIA IN TWO DIFFERENT TYPES OF BRAIN TUMORS 40

1. Introduction…….41

2. Materials and methods…….44

2.1. Materials 44

2.2. Relaxivity Measurements 45

2.3. Animal Models 45

2.4. PET and MRI 46

2.5. Immunohistochemistry Assay 46

2.6. Image and Data Processing 47

2.7. Pharmacokinetic Modeling 48

2.8. Statistical Analysis 52

CHAPTER Page

3. Results…….52

4. Discussions and conclusion…….99

DEVELOPING A NOVEL HYPOXIA TARGETING CONTRAST AGENT 103

1. Introduction……...104

2. Materials and Methods……..109

2.1. Materials 109

2.2. Synthesize 109

2.3. Chelation 111

2.4. Cytotoxicity.....111

2.5. Relaxometry 112

2.6. In vitro Studies 112

2.7. MRI imaging 113

2.8. Statistics 114

3. Results……...114

4. Discussion……..124

5. Conclusion…….128

CONCLUSIONS AND FUTURE DIRECTIONS 130

REFERENCES 133

APPENDIX

A GDDO3NI ALLOWS IMAGING OF HYPOXIA AFTER BRAIN INJURY 1500

APPENDIX Page

B EMERGING TRENDS IN MR BASE CELL LABELING AND TRACKING TECHNIQUES (IN PREPARATION) 163

C DFOBNI: AN IRON-BASED HYPOXIA TARGETING CONTRAST AGENT (IN PREPARATION) 165

D QUANTITATIVE MAPPING OF BRAIN TISSUE OXYGENATION AROUND NEURAL INTERFACES^{+} (IN PREPARATION) 168

E MAPPING HYPOXIA IN BRAIN TUMORS USING GDDO3NI : VALIDATION WITH PET AND IHC (IN PREPARATION) 170

LIST OF TABLES

Table Page

Table 1. The T1 and T2 Values for Some of the Well-known Tissues in MRI……10

Table 2. Injury Volume, Normalized Differential Enhancement and Contrast Agent Retention Fraction for Each Animal in the Gadoteridol (Control) and GdDO3NI Cohorts.....33

Table 3. The Tumor Size and the NDE Value of the Animals in the 9l Cohort……61

Table 4. The Tumor Size and the NDE Value of the Animals in the C6 Cohort……..61

Table 5. Summarized K1 Values of Each Animal in 9l Cohort 1h Post Injection in the Tumor, Contralateral Brain, and Muscle ROI s…….....91

Table 6. Summarized K2 Values of Each Animal in 9l Cohort 1h Post Injection in the Tumor, Contralateral Brain, and Muscle ROI s……...……...91

Table 7. Summarized Vp Values of Each Animal in 9l Cohort 1h Post Injection in the Tumor, Contralateral Brain, and Muscle ROI s…….……...91

Table 8. Summarized K1 Values of Each Animal in C6 Cohort 1h Post Injection in the Tumor, Contralateral Brain, and Muscle ROI s……...…...92

Table 9. Summarized K2 Values of Each Animal in C6 Cohort 1h Post Injection in the Tumor, Contralateral Brain, and Muscle ROI s…….....92

Table 10. Summarized Vp Values of Each Animal in C6 Cohort 1h Post Injection in the Tumor, Contralateral Brain, and Muscle ROI s…….....92

Table 11. Summarized K1 Values of Each Animal in 9l Cohort 2h Post Injection in the Tumor, Contralateral Brain, and Muscle ROI s…….....93

Table Page

Table 12 Summarized K2 Values of Each Animal in 9l Cohort 2h Post Injection in the Tumor, Contralateral Brain, and Muscle ROI s…….....93

Table 13 Summarized Vp Values of Each Animal in 9l Cohort 2h Post Injection in the Tumor, Contralateral Brain, and Muscle ROI s……...……..93

Table 14 Summarized K1 Values of Each Animal in C6 Cohort 2h Post Injection in the Tumor, Contralateral Brain, and Muscle ROI s……...…..94

Table 15 Summarized K2 Values of Each Animal in C6 Cohort 2h Post Injection in the Tumor, Contralateral Brain, and Muscle ROI s……...…..94

Table 16 Summarized Vp Values of Each Animal in C6 Cohort 2h Post Injection in the Tumor, Contralateral Brain, and Muscle ROI s…….....94

Table 17 the Relaxation Times Calculated for the Control Cells, FOB Exposed Cells Under Normoxic (N) and Hypoxic (H) Conditions and FOBNI Exposed Cells Under Normoxic (N) and Hypoxic (H) Conditions. 120

LIST OF FIGURES

Figure Page

Figure 1. Chemical Structure of GdDO3NI , and Its Relaxivity at 7T. GdDO3NI (Mw = 839 g/mol), Revealed the Relaxivity Values as r_1=4.75±0.04 $s^{-1}mM^{-1}$ and r_2=7.52±0.07 $s^{-1}mM^{-1}$ at 37 °C and 7 T…..……..16

Figure 2. MRI T_2 Weighted Scout Images and Signal Enhancement (%) Overlay on T_1 Weighted Images of Mice Brains Pre- and Post-injection of Conventional Gd Agent Gadoteridol (Top Row), and GdDO3NI (Bottom Row) over 3 hrs after Injection. White Arrow Shows Location of Injury……. 26

Figure 3. Signal Intensity Enhancement Data in the Injured Brain, Contralateral Brain, and Muscle Regions (%) for the Individual Animals in the Gadoteridol Cohort. Gadoteridol, the Conventional, Nontargeting Contrast Agent Served as Control in This Study. The ROI Analysis Was a Voxel-wise Comparison and Was Performed in Matlab by Measuring the Percentage Enhancement of Signal Intensity in T_1 Weighted Images over Three Hours of the Experiment Compared to the Pre-injection Image……...……28

Figure 4. Signal Intensity Enhancement Data in the Injured Brain, Contralateral Brain, and Muscle Regions (%) for the Individual Animals in the GdDO3NI Cohort. The ROI Analysis Was a Voxel-wise Comparison and Was Performed in MATLAB by

Figure Page

Measuring the Percentage Enhancement of Signal Intensity in T_1 Weighted Images over Three Hours of the Experiment Compared to the Pre-injection Image……...30

Figure 5. Time Course Mean Normalized Differential Enhancement (NDE) Results for Gadoteridol and GdDO3NI Injected Cohort During 3 hrs after Injection. NDE Is Calculated as the Difference Between the % Enhancements of the Injury Region and a Contralateral Brain Region of Interest (ROI) Normalized to the Peak % Enhancement for a Muscle ROI …….31

Figure 6. 3d Rendering of Hypoxic Regions in Brains of Representative (a) Gadoteridol and (B) GdDO3NI Injected Animal. Color Scale Represents Percentage Enhancement at 3 Hrs Post Injection of Respective Contrast Agent. 3d Rendering Shows Both the Spatial Extent as Well as the Severity of Hypoxia in the GdDO3NI Cohort and the Degree of Residual Agent Retention in the Gadoteridol Cohort. Color Scale= 10% -100%, Scale Bar = 5 mm. …….32

Figure 7 Immunohistochemical Staining for Hypoxia in Injured Animals (Corresponding to Fig 1), DAPI Is Visualized in Blue and Pimonidazole Staining Is Visualized in

Figure Page

Green in Representative Animals Injected with (a) Gadoteridol or (B) GdDO3NI . Both Cohorts Display Presence of Hypoxia Post Injury. Scale Bar = 1 Mm……...34

Figure 8. T_1 Relaxometry of Two Batches of GdDO3NI at 7 T at 37 ºC, the Equation for the Line on the Left Graph Is r_1=0.09+3.70[C] and for the Right Graph Is r_1= .26+4.78[C]……49

Figure 9. The Left Is Representative of the Small 9L Tumor from Top: Pimonidazole Staining Overlaid on MRI T_2, Pet Scan Overlaid on Mri, Mri and the Difference Image of Before Injection and the 2h Post Injection Time Point. The Right Is Representative of the Big 9L Tumor from Top: Pimonidazole Staining Overlaid on Mri T2, Pet Scan Overlaid on Mri, Mri and the Difference Image of Before

Figure Page

Injection and the 2h Post Injection Time Point. The IHC and Pet Images Are Acquired by Dr. Matthew Scarpelli……50

Figure 10. Percentage Enchantment Results from Dce Experiment over 2h, Representative of Big(Top) and Small(Bottom) Tumors……51

Figure 11 Water Phantom and Result of DCE Sequence Running for 2h…….52

Figure 12. Time Course Data for the Tumor, Contralateral Brain and Muscle Region after Applying Conditional Smoothening and Drift Algorithm for 9L Cohort……56

Figure 13. Time Course Data for the Tumor, Contralateral Brain and Muscle Region after Applying Conditional Smoothening and Drift Algorithm for C6 Cohort……...60

Figure 14. Correlation Between NDE and Tumor Volume in the C6 Cohort. The Equation of Fit Curve and the r^2 Representing the Line Is NDE=-0.011×vol.+0.843 and r^2=0.11……62

Figure 15 Correlation Between NDE and Tumor Volume in the 9L Cohort. The Equation of the Fitted Curve and the r^2 of the Red Line, Which Shows the Correlation Between All the Data Points and Tumor Volume Is NDE=0.016×vol.-0.237 and

Figure Page

r^2=0.53 and the Blue Line, Which Shows the Correlation Between All the Positive NDE Values and Tumor Volume Is NDE=0.011×vol.+0.036 and r^2=0.9……...63

Figure 16. T_1 Map of the Animals Before Injection in 9L Cohort the Color Bar Is Represented in ms Units……..…68

Figure 17. T_1 Map of the Animals Before Injection in C6 Cohort the Color Bar Is Represented in ms Units……..…72

Figure 18. T_1 Map of the Brain (a) and ROI Analysis for Tumor, Contralateral Brain and Muscle Region on R_1 (B) and Concentration Map Respectively (C)……..73

Figure 19. The Pharmacokinetic Parameters Representing a) Ktrans, B) K2 and C) v_p…..74

Figure 20. The Computed Concentration Map from the MR Data (a), the Reconstructed Concentration Map Using Pharmacokinetic Parameters (B) and the Difference Map (C)……..75

Figure 21. the T_2 Weighted Anatomical Image and the Pharmacokinetic Maps and Concentration Maps of the Individual Animals in 9L Cohort over 1h Post-injection in a, C, E, G, I, K, M, O and 2h Post-injection in B, D, F, H, J, L, N, P……83

Figure 22. the T_2 Weighted Anatomical Image and the Pharmacokinetic Maps and Concentration Maps of the Individual Animals in C6 Cohort over 1h Post-injection in a, C, E, G, I, K, M, O and 2h Post-injection in B, D, F, H, J, L, N, P……91

Figure 23. 1h Nmr (550 Mhz, Dmso-d6): Δ 7.8 (2h, Amide), 3.46 (6h, -ch2-(N-oh)-), 3 (4h, -ch2-(Nh)-). Nmr Spectra of Dfob in Dmso-d6 Without Further Modifications...112

Figure Page

Figure 24. ^{1}H NMR (550 Mhz, Dmso-d6): Δ 7.8 (2h, Amide), 3.46 (6h, -ch2-(N-oh)-), 3 (6h, -ch2-(Nh)-). Nmr Spectra of Dfobni in Dmso-d6 after Column Chromatography……..……113

Figure 25. Result of Esi-ms of Dfob. 50/50 A/B, A: 20 Mm Ammonium Formate in Water, and B: 20 Mm Ammonium Formate in Meoh……...114

Figure 26. Result of Esi-ms of a)Dfobni and B)Fobni after Dialysis. 50/50 A/B, A: 20 Mm Ammonium Formate in Water, and B: 20 Mm Ammonium Formate in Meoh….115

Figure 27. Fibroblast 3T3 Cell Viability Assay Using Alamar Blue after Being Exposed to Fobni over Different Periods in Normoxic Condition a) Represents the Data Using the Control for 4h for All the Time Points and B) Represents the Data Using the Control in Each Time Point the * in Each Case Shows the Statistical Significance Compared to Control……116

Figure 28. Fibroblast 3t3 Cell Viability Assay Using Alamar Blue after Being Exposed to Fobni over Different Periods in Hypoxic Condition a) Represents the Data Using the Control for 4h for All the Time Points and B) Represents the Data Using the Control in Each Time Point the * in Each Case Shows the Statistical Significance Compared to Control……117

Figure 29. T_1, T_2 Maps in ms and Concentration Maps in Mm Fe for a) DFOB and B) DFOBNI……...119

Figure 30. Relaxivity Study of a) dfob with the Fit Curves Representing the Data as r_1=2.06±0.06C+0.49± .04(in Red) and r_2=2.75±0.06C+3.75±0.08 (in Gray) and B)

Figure Page

Fobni with the Linear Fit Equations as R1=0.51±0.1c+0.44±0.03 (in Red) and R2=4.51±0.14c+3.87±0.19 (in Gray)……...120

Figure 31. T1 (Upper Row) and T2 (Lower Row) Maps of Cell Pellets, a) and B) Control, C) and D) Exposed to FOB, and E) and F) Exposed to FOBNI…….121

CHAPTER 1

INTRODUCTION ON TISSUE HYPOXIA AND ITS DETECTION METHODS

1. Introduction

Among hypoxia targeting compounds, the 2-nitroimidazole, pimonidazole, has been shown to result in reliable outcomes in spotting hypoxic regions in tissues. Pimonidazole molecule gets reductively activated and under very low concentrations of oxygen binds to thiol-containing proteins, and the new adducts can be detected by immunohistochemistry under a fluorescent microscope[1]. The results from immunohistochemistry assay in detecting and locating hypoxia are universally accepted; however, the method is invasive in nature. Recently, Gulaka et al. have used a novel nitroimidazole-based T_1 contrast agent, gadolinium tetraazacyclododecanetetraacetic acid monoamide conjugate of 2-nitroimidazole (GdDO3NI), to measure hypoxia of tissue in vivo and non-invasively using magnetic resonance imaging (MRI)[2]. Due to the fact that GdDO3NI has the same targeting moiety as pimonidazole, it is assumed to follow the same mechanism of reactivity under the hypoxic conditions with proteins. This translates into retaining Gd chelate in the binding sites and revealing high-intensity regions on T_1 weighted MR images for hypoxic regions. The successful studies[2],[3] promise new opportunities to use GdDO3NI in other pathologies and cancers. In this study report, we deal with the performance of GdDO3NI in detecting hypoxia in brain injuries and brain tumors. In addition, we will introduce a novel iron-based contrast agent to detect hypoxia. In the following, we introduce the important concepts that help familiarize us with the biology and physics playing an important role in this study.

2. Tissue microenvironment

In healthy biological tissues, ensembles of cells and biological materials work together in a healthy microenvironment to ensure the necessary functions of different organs. However, an altered microenvironment can be a sign of disease. For example, in malignant cancers genetic and epigenetic changes of the cells result in the inability of the cells to restructure the microenvironment despite the innate regulatory processes in cells to balance between health and disease[4]. In addition, reported changes in the extracellular matrix (ECM), cerebral blood flow and perfusion, blood brain barrier (BBB) integrity, brain oxygenation, cerebral metabolism, brain temperature and accumulation of toxic molecules in traumatic brain injury is another example that shows the tissue microenvironment is different between a normal and diseased state[5]. The evidence suggest the correlation between tissue microenvironment changes and its dysfunction, while the challenging problem is to choose the best tissue microenvironmental targets to proceed with therapy. This approach can shed light on the most effective therapeutic result because it can guide a patient specific and personalized treatment.

2.1. Oxygen and tissue hypoxia

One key factor in the survival of most living organisms, especially mammalian cells, is to maintain oxygen homeostasis. Oxygen is the second most abundant gas in the earth's atmosphere, which is nonpolar and paramagnetic. Its solubility in an aqueous condition is controlled with temperature and salinity. Oxygen is used to generate energy and enhance enzymatic reactions to produce vital products. However, in order to temporarily survive or producing high amounts of energy in small amount of time, aerobic cells have developed

a glycolysis pathway to reduce their energy production dependence on oxygen[6]. In general, any perturbation of the normal balance in oxygen supply and demand, mainly its decrease, will result in microenvironment alteration and consequently generates pathological states and death of the cells. The importance of oxygen in mammalian tissue results in developing sophisticated mechanisms to tightly regulate and maintain its concentrations[6]. Regulating oxygen levels in the body occur through cell chemoreceptors and cause adjusting of cardiovascular and ventilator rates or adaptive pathways and thus survival. Moreover, cells play an important role in regulating oxygen levels utilizing pre-existing proteins and the regulation of gene transcription. Under hypoxic conditions, cells switch their metabolism from oxygen-dependent to oxygen-independent pathways; this observation was first made by Pasteur, hence named the "Pasteur effect." If the decrease in pO_2 is not dramatic, cells adapt to new conditions with some changes in protein synthesis; this process is called "penumbra" and is characterized by reversibility[7]. However, it is reported cancerous cells can adapt permanently to low O_2 levels called the Warburg effect. This adaptation changes the cells' metabolism and function. Therefore, oxygen can be an important marker in most living organisms to assess viability, metabolic status and functionality in addition to study their response to environmental changes and therapies. Lack of oxygen, known as hypoxia, occurs when sufficient amounts of oxygen are not provided to tissues or cells to meet their metabolic needs. Different tissues have different tolerance to hypoxia; some can survive under hypoxic conditions for a long-time while others get damaged or die under low oxygen concentration. Hypoxia can be the result of decreased oxygen delivery because of hypoventilation, a low oxygen content of inhaled gas, abnormal vascular network and

interstitial edema, interstitial inflammation or fibrosis[8]. In general hypoxia is categorized into chronic hypoxia, which results from limitations in diffusion, and acute hypoxia, which is because of limitation in perfusion[9–15].

Hypoxia as one of the posttraumatic insults in patients affected by TBI renders mortality and negatively impacts the neurological outcome. It can emerge immediately or over a few hours to days after the insult. Even though it has been discussed in literature why hypoxia happens after TBI and it is accepted it can be the result of impaired brain perfusion, extracranial trauma and peripheral hemorrhage[16], there is no solid practical study in quantifying brain hypoxia[17–19]. The pathology of TBI occurs from both immediate and delayed mechanisms such as edema, ischemia, hemorrhage, finally resulting in highly heterogeneous tissue damage[20]. Specifically, early posttraumatic hypoxia plays a significant role in treatment outcome[16]. Studies have reported about 30-50% of TBI patients in a traumatic coma have hypoxia upon arrival at an emergency room and the time to resuscitation significantly affects the outcome[21]. The current diagnostic techniques for TBI lack the sensitivity to detect events such as hypoxia that will provide information for better therapeutic intervention and management.

An organized network of arteries, veins and capillaries maintains adequate amounts of oxygen in normal tissues; however, the excess proliferative capacity of cancerous cells, which results in a tortuous, leaky and disorganized vascular network cannot provide sufficient oxygen to the tissue and leads to hypoxia[22–24]. The main variable in regulating the tumor angiogenesis is hypoxia inducible factor-α (HIF1- α) and its upregulation under hypoxia results in the expression of the VEGF-A and VEGFR2[25]. It is reported in normal

tissues, the oxygen diffusible distance from the blood vessels to avoid hypoxia is 100-150 μm and the regions beyond this develop chronic hypoxia.

2.2. Importance of hypoxia, and techniques to study tissue oxygenation

There are a large number of scientific publications dealing with the contribution of hypoxia in different pathologies such as TBI[26–28], cancer[29], stroke[30] and injuries and its effects. Oxygen is the most important biomolecule in the body which can influence the efficacy of therapy and its outcomes. For example, in TBI, it is reported hypoxia results in poor neurological outcomes, it induces neuroinflammation, it is frequently considered as the secondary insult to brain tissue resulting in neuronal cells' dysfunction and death[16]. Hypoxia plays an important role in the characterization and studying of the tumor microenvironment, and its evaluation is critical in studying tumors and developing personalized treatments[3,9,31–34]. It is reported hypoxia decreases the sensitivity of tumors to chemo- and radio- therapy; it promotes angiogenesis and invasiveness of the tumor[35–40]. The presence of hypoxia alters the genetic properties of cells and the adapted cells can survive very harsh conditions compared to normal cells and the increased survival ability limits the outcome of potential therapies. The distribution and severity of hypoxia can vary over time in different pathologies in different patients. Hypoxia as an important characteristic of tissue can provide information to select treatment approaches, design hypoxia targeted therapies and techniques to image hypoxia imaging. In summary hypoxia can result in the following complications, especially in TBI and tumors[9,28]:

1. Secondary insult to brain tissue,

2. Poor neurological outcomes,
3. Resistance to chemotherapy and radiotherapy,
4. Genomic instability,
5. Increased aggressiveness, invasiveness, and metastasis.

A variety of different methods and techniques have been developed to measure and quantify oxygen levels. Initially, those were simply divided into physicochemical and instrumental analysis[6]. The most important and common downside of these approaches was that they were not providing real time measurements. However, because of the importance of oxygen and the need to study it to understand its effects scientists are developing novel techniques. These techniques usually overcome the limitations of the previous methods. An ideal platform is noninvasive, has high resolution and sensitivity and is reliable. The interested reader is referred to the detailed review article about oxygen sensing by Papkovsky et al.[6]. Some of the well-known techniques to assess oxygen tension that are currently in practice are Clark-type oxygen electrode[41], fiber optic probe[42], pulse oximetry[43], and immunohistochemical staining methods like pimonidazole staining[44]. While it is invasive, pimonidazole staining is considered the gold standard to study hypoxia. Some of the newly developed techniques dealing with oxygen tension measurements and hypoxia include Electron Paramagnetic Resonance[45], Positron Emission Tomography (PET)[46], BOLD fMRI[47], ^{19}F-MRI[48], PISTOL[49], and hypoxia targeting contrast agents[2].

3. Nitroimidazole and hypoxia

Among the various procedures to detect hypoxia the immunohistochemical hypoxia marker technique[50] has shown promising results. Especially, the 2-nitroimidazole hypoxia marker, pimonidazole is proved to result in excellent outcomes in spotting hypoxic regions. Nitroimidazoles are originally developed for antibacterial purposes, but now their derivatives are used in imaging hypoxia with different modalities like microscopy[1], PET[51] and MRI[2]. The currently accepted mechanism for pimonidazole is demonstrated in Scheme 1. In the proposed mechanism pimonidazole gets activated in the presence of nitro-reductases the reduced state of nitroimidazole group is reversible if the molecule is in normoxic conditions. However, in case of lack of oxygen the nitroimidazole group undergoes one more reduction step and subsequently binds to thiol-containing proteins in hypoxic regions. This bond is covalent and the reaction is irreversible, which ensures the retention of pimonidazole.

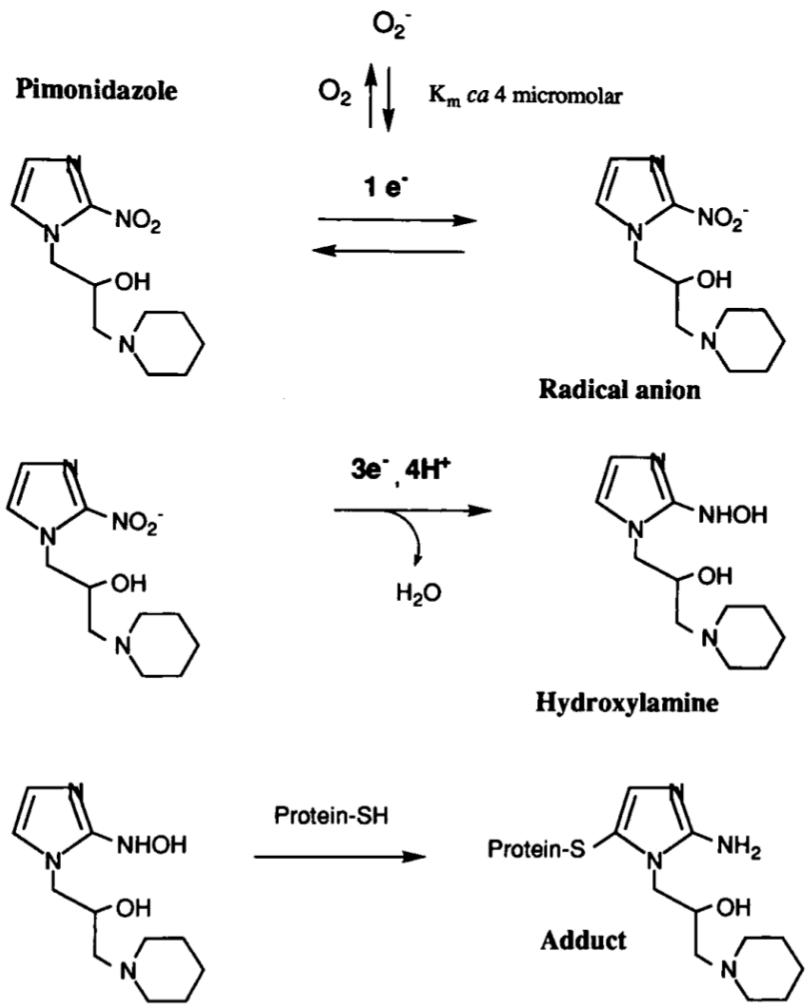

Scheme 1 The proposed reaction mechanism and binding of pimonidazole to thiol groups[1]

It is important to mention the actual reaction mechanism of nitroimidazoles and the binding sites in cellular components to pimonidazole are not identified and this is the major gap in our knowledge of nitroimidazoles retention, but the literature review suggests intracellular macromolecules like proteins or intercellular component like DNA[52]. But we know, the new bond can be detected by immunohistochemistry under a microscope[1]. The accuracy of the results from immunohistochemistry assay in detecting and localizing

hypoxia is universally accepted; however, the retention of nitroimidazole is heavily dependent on the tissue and the pathology under study. In addition, one cannot condone that the method is invasive and it can be hard or in some cases not feasible to perform. Considering the currently accepted mechanism of nitroimidazole under hypoxic conditions, researchers have developed noninvasive methods to image hypoxia, which are inspired with nitroimidazoles like ^{18}F-FMISO[51] for PET, GdDO3NI [2] and FOBNI for MRI.

4. Magnetic resonance imaging

MRI is a non-invasive imaging modality. It utilizes the same physical principles of nuclear magnetic resonance (NMR). Using the nuclear spin properties, we can generate a signal from a sample in the presence of an external magnetic field. The signal is the result of the precession of the net magnetic moment and the induced current in the receiver coil. In MRI, the generated signal is spatially encoded using gradients; in order to construct the image the signal is transformed with 2D Fourier Transform. The advances in the past few decades in generating strong external magnetic fields and improvements in electronics and computer systems resulted in higher resolution and signal to noise ratio in MR images.

In detail, the MR signal follows Faraday's law of induction and is an induced electrical current generated by the net magnetization during resonance. Hydrogen is one of the atoms that possess two different proton spin states ½ and -½ without any external magnetic field the nuclear magnetic moment of the protons are randomly placed in space and result in zero net magnetic moments, the vector sum of the individual magnetic moments. However, under external magnetic field the protons' magnetic moment align parallel and against with the external magnetic field. In this process a slightly more number of protons (about three

in one million protons) align with the external field and result in the net magnetic moment for the bulk this magnetic moment can be detected later as the MR signal. Since human body weight is composed of about 70% water and other organic materials, which contain hydrogen atoms, it can serve as a perfect hydrogen pool to generate proton MRI signal. Image contrast, which is the ability to demark different tissues in an MR image, has different origins. MR images can create contrast between different tissues based on imaging parameters (TR, TE, α) and contrast agents. The contrast is generated in the former, based on the intrinsic properties of the tissue like spin-lattice relaxation time (T_1), spin-spin relaxation time (T_2), observed spin de-phasing time (T_2*), proton density (ρ) and diffusion, while in the latter, changes in relaxation rate of protons in tissues perfused with the contrast agent are responsible for the contrast enhancement. The intrinsic properties of the tissue in generating contrast can be exploited by applying different choices of settings on the scanner and obtaining weighted images. For instance, the following table shows the T_1 and T_2 values of different materials.

Table 1. The T_1 and T_2 values for some of the well-known tissues in MRI

Material	T_1	T_2
Water (at 1.5 T) [24]	~4000 ms	~2000 ms
Fat	280-340 ms	60-100 ms
White matter	~ 800 ms	~80 ms
Gray matter	~1100 ms	~90 ms

The restriction of protons and their interaction with their surroundings can influence the T_1 and T_2 values. For example, the T_1 and T_2 values of Cerebrospinal fluid (CSF) are similar to those of water because the protons are freely moving like they do in water; however, the protons in fat because of the restriction in movement and their environment have shorter T_1 and T_2. It is worth mentioning, in pathologies like a tumor, injury and inflammation the water content of the tissue increases, and these tissues can easily be detected in T_2 weighted images and this explains why the T_2 weighted images are routinely used in clinical examinations to detect abnormalities.

There are situations that the contrast generated by intrinsic properties is subtle and is not providing useful information of the internal structure. Contrast agents are materials that can influence the intrinsic properties of their surroundings and result in improved contrast in the MR images[53–55]. Contrast agents have attracted a lot of attention because they can be modified with targeting groups to shed light on some physiological and biological questions such as the presence of hypoxia in a tissue. MRI as a noninvasive imaging modality can provide extremely important and crucial information about pathologies and anatomy and also generate functional images with high resolution, which can help to develop therapeutic approaches and to monitor the treatment.

4.1. T_1, T_2, T_2^* relaxation mechanisms

Right after the excitation takes place, the system tries to turn back to its lower energy state by losing energy. The process by which the net magnetization returns to its maximum value (M_o) is referred to as T_1 relaxation. The other synonyms for this process are spin-lattice relaxation and thermal relaxation. During this process the net magnetization

exponentially grows to M_o following $M_t = M_o(1 - e^{-t/T_1})$ equation. T_1 is a measure of the rate at which the recovery of magnetization happens. According to the T_1 relaxation equation when the $t=T_1$ the recovered net magnetization is about 63% of the net magnetization at equilibrium and when $t=5T_1$ the net magnetization is fully recovered.

To generate the MR signal, the nuclei in the sample should be excited with radio frequency (RF). The excited state is the result of energy accumulation in the system and modification of the energy state of the spins, which is concomitant to the appearance of magnetization in the x-y plane in the frame of reference. The appeared magnetic moment in the x-y starts to decay because the spins lose coherence due to experiencing the magnetic field from adjacent nuclei. The rate indicating the decay of transverse magnetization is known as T_2 and the process is transverse relaxation known as spin-spin relaxation. It is governed by $M_{xy}(t) = M_o e^{-t/T_2}$. A complementary relaxation mechanism to spin-spin relaxation is T_2^* relaxation, which results from a combination of T_2 relaxation and inhomogeneity of the magnetic field. This relaxation process can be observed in gradient echo-based sequences because they do not use 180 pulses to cohere the isochromats and the inhomogenous magnetic field, which results in incoherent isochromats is also responsible for additional decay of the transverse magnetization.

4.2. Paramagnetic relaxation

MRI contrast agents, consisted of paramagnetic atoms like Fe and Gd that produce contrast indirectly in the images, i.e., the contrast agent changes the relaxation rate of protons in the surrounding water molecules. In other words what we see as bright/dark regions in conventional contrast agent aided MRI is not coming directly from the contrast agents, but

the contrast is generated because of the effect of contrast agent on surrounding protons with changing the relaxation rate of them resulting in image contrast on T_1 and/or T_2 - weighted images. Generally speaking, most of the gadolinium-based contrast agents produce T_1 weighted contrast and the iron-based ones produce T_2 weighted contrast in the MR images. Relaxivity is a term defined to quantify the ability of a contrast agent in altering the relaxation rate of a tissue (R_1 and R_2). Relaxivity is a very complex concept and is influenced by many factors such as temperature, the external magnetic field and molecular structure. Even though diving into the detailed mechanisms of paramagnetic relaxation is out of the scope of our studies and the interested readers are referred to useful references[54,56,57], we briefly mention the general mechanisms and equations here.

The equation describing the relationship between relaxation rate, R, and relaxivity of the contrast agent, r, at a fixed temperature and external magnetic field is as follows:

$$R_i = [C]r_i + R_i^0$$

Where R_i (i=1 or 2) is the relaxation rate of the tissue, C is the concentration of the contrast agent, r_i is the relaxivity of the contrast agent and the R_i^0 is the intrinsic relaxation rate of the tissue[58(p1)].

In the production of new contrast agents, it is recommended the product of the relaxivity by the concentration be more than 10% of the intrinsic relaxation rate of the tissue to generate a successful contrast in the image[58(p1)]. Improving the relaxivity of a given contrast agent translates in the same contrast with lower concentrations that eliminates some of the side effects of the contrast agents, such as toxicity and accumulation and improves the resolution of the targeted contrast agents. Magnetic field strength alters

the relaxation rate of the contrast agent which typically decreases with increasing field strength[55]. The paramagnetic properties of an atom rest on the number of its unpaired electrons, i.e., the higher the number of unpaired electrons, the more enhanced paramagnetic properties. For example, Gd^{3+} with 7 unpaired electrons possesses a high magnetic moment. The unpaired electrons of the paramagnetic atom create a fluctuating local magnetic field and the dipole-dipole interaction of the protons of the water molecule with the paramagnetic atom results in the paramagnetic relaxation of the water protons. The paramagnetic relaxation takes place mainly through two different mechanisms of the inner sphere described by Solomon-Bloembergen-Morgan theory and outer sphere relaxation described by Freed[59].The inner sphere relaxation is the result of the direct interaction of the exchanged water molecules with paramagnetic ion, which is governed by the external magnetic field, water exchange rate and the distance between the paramagnetic ion and the relaxing protons. On the other hand, the outer sphere relaxation is due to fluctuating magnetic field experienced by the diffusing water molecules around the paramagnetic molecule. The other mechanism, which is hard to evaluate and as a result is included in the inner sphere relaxation mechanism is called the second sphere relaxation mechanism. This mechanism rises from the hydrogen bond between the surrounding water molecules with either the chelator molecule or the water molecule in the inner sphere coordination. All these three mechanisms can influence the overall relaxivity of a contrast agent and shed light on the designing approach of the molecules. For instance, large chelating molecules due to their size reduce the water exchange rate in addition to the lower number of coordinated water molecules result in lower relaxivity of the contrast agents[60].

Since the outer sphere relation cannot be modified the study of the inner sphere relaxation mechanism is of paramount importance in designing contrast agents with higher relaxivity.

The following equations are describing the theoretical relations for the inner and outer relaxations[53] with the observed relaxation

$$r = r^{is} + r^{os}$$

$$(\frac{1}{T_1})_{inner\ sphere} = \frac{P_M q}{T_{1M} + \tau_m}$$

Where r^{is} is the relaxation in the inner sphere and the r^{os} is the relaxation in the outer sphere, P_M is the concentration of the paramagnetic atom, q is the hydration value (the number of water molecules in direct contact with the paramagnetic atom), T_{1M} is the relaxation time of the coordinate water and τ_m is the residence lifetime of the coordinate water.

4.3. Targeting MR contrast agents

Gd-based contrast agents are still the key players in generating MR contrast. Most of the developed contrast agents are non-specific and known as conventional contrast agents. The term non-specific describes the contrast agent as a molecule distributed in the body with no preference to a specific tissue or a receptor. The conventional contrast agents are used in imaging pathologies, vascular permeability and MR angiography. Even though the conventional contrast agents are extremely beneficial in generating meaningful anatomical MR images, they cannot specifically target a region or provide information of tissue microenvironment or enable molecular imaging. Targeting contrast agents are developed to provide information from a specific tissue or site in the body. For example, GdDO3NI [61] is a hypoxia targeting contrast agent and it can detect hypoxic region in the tissue. There

are different approaches in developing targeting contrast agents. The most common approach, is using conjugation chemistry. In this method, the conventional contrast agents are chemically modified and conjugated to an antibody[62,63] or a targeting molecule[61]. The common three segments of the targeting contrast agents are the chelator of the metal, the linker and the targeting moiety. In 2012 Rojas- Quijano et al. synthesized and characterized GdDO3NI as Gd-based hypoxia targeting contrast agent[61]. The contrast agent is composed of a DOTA group, a linker and a nitroimidazole moiety as the hypoxia targeting group. To days, the retention and binding mechanisms of GdDO3NI are not investigated. GdDO3NI has the same imidazole chemical group as pimonidazole; therefore we assume it follows the same proposed chemical mechanism and pathway to bind to hypoxic region. The relaxivity properties of GdDO3NI are reported as r_1= 4.75 ± 0.04 $mM^{-1}s^{-1}$ and r_2= 7.52 ± 0.07 $mM^{-1}s^{-1}$ at 7 T[3].

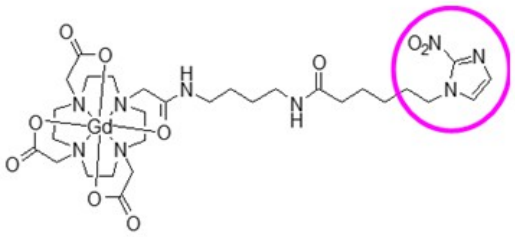

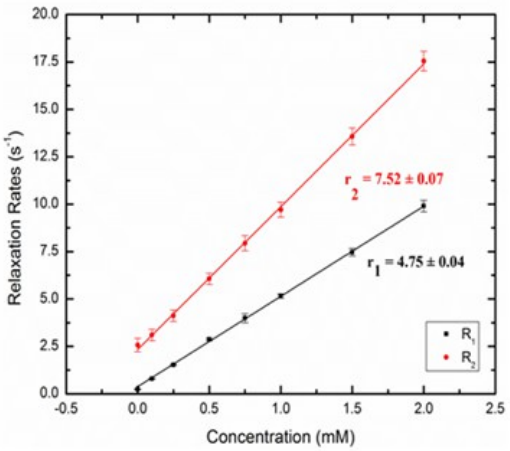

Figure 1. Chemical structure of GdDO3NI , and its relaxivity at 7T. GdDO3NI (MW = 839 g/mol), revealed the relaxivity values as $\boldsymbol{r_1 = 4.75 \pm 0.04\ s^{-1}mM^{-1}}$ and $\boldsymbol{r_2 = 7.52 \pm 0.07\ s^{-1}mM^{-1}}$ at 37 °C and 7 T[3].

CHAPTER 2

ASSESSMENT OF HYPOXIA IN TRAUMATIC BRAIN INJURY USING HYPOXIA TARGETING CONTRAST AGENT

Submitted to the Journal of Magnetic Resonance Imaging, and bioRxiv preprint : https://doi.org/10.1101/2021.03.16.435723

Purpose: In this study, we use the hypoxia targeting agent (GdDO3NI , a nitroimidazole-based T_1 MRI contrast agent) for imaging hypoxia in the injured brain after experimental traumatic brain injury (TBI) using magnetic resonance imaging (MRI), and validate the results with immunohistochemistry (IHC) using pimonidazole.

Methods: TBI induced mice (controlled cortical impact model) were imaged at 7T using a T_2 weighted fast spin-echo sequence to estimate the extent of the injury. The mice were then were intravenously injected with either conventional T_1 agent (gadoteridol) or GdDO3NI at 0.3 mmol/kg dose (n=5 for each cohort) along with pimonidazole (60 mg/kg). Mice were imaged pre- and post-contrast using a T_1-weighted spin-echo sequence for three hours. Regions of interests were drawn on the brain injury region, the contralateral brain as well as on the cheek muscle region for comparison of contrast kinetics. Brains were harvested immediately post imaging for immunohistochemical analysis.

Results: GdDO3NI is retained in the injury region for up to 3 hours post-injection ($p< 0.05$ compared to gadoteridol) while it rapidly clears out of the muscle region. On the other hand, conventional MRI contrast agent gadoteridol clears out of both the injury region and muscle rapidly, although with a relatively more delayed wash out in the injury region. Minimal contrast enhancement was seen for both agents in the contralateral hemisphere.

Pimonidazole staining confirms the presence of hypoxia in both gadoteridol and GdDO3NI cohorts, and the later cohort shows good agreement with MRI contrast enhancement. Conclusion: GdDO3NI was successfully shown to visualize hypoxia in the brain post-TBI using T_1-wt MRI.

1. Introduction

Traumatic brain injury (TBI) occurs due to damage to the brain resulting from an external mechanical force, including rapid acceleration or deceleration, blast waves, crushing force, an impact, or penetration by a projectile[64]. An estimated 1.7 million TBI occur annually in the U.S., which results in the hospitalization of 373,000, and 99,000 totally disabled individuals, and over 50,000 deaths[65,66]. Disabilities as well as cognitive, behavioral, and productivity problems are the most common complications for survivors; in acute cases, the affected individuals face mortality[67,68]. Upon sustaining a TBI, the mechanical forces from impact inflict heterogeneous tissue damage, referred to as the primary injury phase[64]. This insult initiates a myriad of pathophysiological and biochemical secondary injury signaling cascades, including hypo- or hyper-perfusion, edema, blood-brain barrier (BBB) dysfunction, and inflammation that evolves from minutes to days post-trauma[69–71].

Brain tissue hypoxia, defined as brain tissue oxygen tension (pO_2) < 15 mm Hg, is a common consequence of TBI due to the rupture of blood vessels during impact[72]. Studies have reported about 30-50% of TBI patients to have hypoxia as early as arriving in an emergency room[21,73]. It is shown that brain hypoxia, as one of the post-traumatic insults, is associated with mortality and poor and unfavorable neurological outcomes[17–19,74–76]. Tissue

hypoxia has a significant cross-talk with inflammatory processes, whereby hypoxia can trigger the upregulation of proinflammatory cytokines, and the resulting inflammation can further exacerbate hypoxia due to an increase in the metabolic demands of cells and a reduction in metabolic substrates caused by thrombosis, trauma, compression (interstitial hypertension)[77]. Cellular signaling continues acutely and post-acutely to restore homeostasis in injured tissue, which, if not controlled, can exacerbate the injury[71,78]. Furthermore, studies suggest brain tissue oxygen-based therapy can reduce mortality rate and ameliorate neurological outcome for the patients[72,79].

Noninvasive characterization of the injury microenvironment is often difficult to achieve through conventional neuroimaging methods (e.g. Computed tomography (CT), T_1w and T_2w Magnetic Resonance Imaging (MRI)) as they are not sensitive enough to identify regions undergoing microstructural changes[80–82]. The CT scan is highly effective in detecting TBI induced skull fractures, bleeding within and surrounding the brain (hematomas) as well as brain swelling (edema) and the resolution of these over time. CT is much more limited in its ability to detect the widespread microscopic injury to axons which leads to many of the long-term problems experienced by TBI patients. MRI is a powerful diagnostic tool that can detect signs of injury such as minute bleeding (microhemorrhage), small areas of bruising (contusion) or scarring (gliosis), which are invisible to the CT scan. Several MR-based neuroimaging modalities have been used to qualitatively examine acute and chronic changes post TBI longitudinally[83,84]: (a) fluid-attenuated inversion recovery (FLAIR) MRI, a sequence that suppresses the high signal from CSF, is sensitive in detecting traumatic lesions and hematomas, (b)T_1-weighted

structural MRI is sensitive to morphological changes in gray matter volume and cortical thickness, (c) diffusion-weighted MRI (DWI) is sensitive to changes in the microstructural integrity of white matter, (d) MR spectroscopy provides a sensitive assessment of metabolic and neurochemical alterations in the brain, and (e) T_2*-weighted blood oxygen level dependent (BOLD) functional MRI (fMRI) provides insight into the functional changes that occur as a result of structural damage and typical developmental processes. BOLD fMRI only reflects vascular oxygenation and it cannot provide data in regions where BBB is disrupted. An unmet need in TBI diagnosis is the ability to assess tissue oxygenation or hypoxia.

Among various invasive techniques to detect hypoxia, the 2-nitroimidazole pimonidazole, has been previously demonstrated to be reliable in detecting hypoxic regions in tissue[85]. After intravenous administration and extravasation, pimonidazole gets activated under hypoxia and binds to thiol-containing proteins in hypoxic regions, and these adducts can be detected *ex vivo* utilizing immunohistochemistry (IHC) in conjunction with fluorescent microscopy[1]. In addition, several noninvasive imaging approaches to assess hypoxia (qualitatively or quantitatively) have been developed and are in various stages of validation from preclinical to clinical use[86]. Currently, [^{18}F]Fluoromisonidazole (^{18}F-MISO) [^{18}F]fluoroazomycin arabinoside (FAZA)[87], [^{18}F]-EF5[88(p1)], [^{18}F] fluoroerythronitroimidazole (FETNIM)[89] and Cu-labelled diacetyl-bis(*N*(4)-methylthiosemicarbazone (Cu-ATSM) are being used as hypoxia targeting PET imaging agents[90]. While PET based probes have significantly advanced the field of hypoxia imaging, there is a strong rationale for the development of MRI based hypoxia-imaging

techniques as well due to the ability of MRI to acquire higher resolution anatomical and complementary functional information in the same scanning session. BOLD and tissue oxygen level-dependent (TOLD) signal[47,91–93] and [^{19}F] Tri-fluoromisonidazole (TF-MISO)[94,95] are MRI techniques to qualitatively image hypoxia while ^{19}F [48,86] and ^{1}H [49,96,97] based MR oximetry techniques quantitatively measure pO_2 in tumors and muscle tissue. Recently, our group used a novel nitroimidazole-based T1 contrast agent, gadolinium tetraazacyclododecanetetraacetic acid monoamide conjugate of 2-nitroimidazole (GdDO3NI , MW = 839 g/mol), to measure hypoxia non-invasively *in vitro* using 9L glioma cells [61] and *in vivo* in a rat prostate cancer model [2] and demonstrated correlation with pimonidazole staining. The relaxivity values of GdDO3NI were reported as r_1=4.75±0.04 $s^{-1}mM^{-1}$ and r_2 =7.52±0.07 $s^{-1}mM^{-1}$ at 37 °C and 7 T[3].

The objective of the present study is to utilize GdDO3NI enhanced MRI, for high resolution visualization of hypoxia in the rodent brain post TBI and to validate MRI data with pimonidazole based IHC. Here, we used the controlled cortical impact (CCI) injury model [98] to recapitulate elements of a focal TBI including focal lesion, axonal injury, BBB disruption, and necrosis[99,100].

2. Materials and Methods

2.1. Materials

ProHance (Gadoteridol; Bracco Diagnostics Inc., Monroe Township, NJ, USA), was used as control contrast agent. GdDO3NI , was synthesized as described previously[61]. Briefly, DOTA (1,4,7,10-tetraazacyclododecane-1,4,7,10-tetraacetic acid) was selected as Gd chelator along with conjugation to 2-nitroimidazole for hypoxia targeting. Pimonidazole

and FITC linked mouse anti-pimonidazole monoclonal antibody (FITC-Mab, Hypoxyprobe Inc, Belmont, MA, USA) was used as the gold standard hypoxia indicator in tissue through IHC staining. The FITC-MAb 4.3.11.3 (Lot# 01.28.15) was purchased from Hypoxyprobe, Inc, Burlington, MA, USA.

2.2. Animal preparation

All animal studies were approved by Arizona State University's Institute of Animal Care and Use Committee (IACUC) and were performed in accordance with the relevant guidelines. Two cohorts of 5 animals each were used in this study. All the procedures on animals were performed under isoflurane (Baxter International Inc, Deerfield, IL). TBI was simulated using the CCI model of TBI[98]. Briefly, adult male C57Bl/6 mice (9-11 weeks old) placed in stereotaxic frame under isoflurane anesthesia (3% induction, 1.5% maintenance). The frontoparietal cortex was exposed via 3 mm craniotomy and the impact tip was centered at −1.5 mm bregma and 1.5 mm lateral from midline. The impactor tip diameter was 2 mm, the impact velocity was 6.0 m/s and the depth of cortical deformation was 2 mm with 100 ms impact duration (Impact ONE; Leica Microsystems). After the impact, the skin was sutured, and the animal was catheterized for tail vein injection. Once the catheter was connected, the animal was placed onto temperature controllable MR bed and kept at 37 °C and under anesthesia (isoflurane at 1.5%).

2.3. Magnetic Resonance Imaging

MRI studies were carried out on a 7 T Bruker system with a surface coil. Mice were placed into the magnet right after the injury and pre-injection T_2 and T_1 weighted scans were acquired in a one hour window after injury and before injection of contrast agents. A

cocktail of 60 mg/kg pimonidazole (hypoxia marker) and 0.3 mmol/kg of either MRI agents (gadoteridol or GdDO3NI) in a 100 μL volume was injected via intravenous injection. Injection of the contrast agents was performed at 1 hour post-injury and follow-up imaging began right after the injection. Multi gradient echo (MGE) sequence with TR= 80 ms, TE= 3 ms, flip angle= 35^{o}, image acquisition time=5min 27s, and FOV (2 cm X 2 cm X 2 cm) were used to monitor the contrast agent uptake in the site of injury over a period of three hours with 10 min intervals after injury. Image data (k-space) were acquired with grid size of 128*64*64 and zero-filled to 128*128*128 for further analysis.

2.4. Data processing

Acquired data was processed using custom-written scripts in MATLAB. Regions of interests (ROI) for the muscle, injury, and the contralateral brain were manually delineating on the T_2 maps, for each animal. These were registered and applied to the time course T_1-wt images as masks to extract data for further analysis. From these data, the injury volume, normalized differential enhancement (NDE) and the contrast agent retention fraction, were calculated for each animal NDE is defined as the difference in percentage enhancement between the injury region and the contralateral brain and divided by the maximum value of the muscle enhancement for each data set. NDE is used to reduce the influence of normal muscle and brain contrast retention, ensuring the calculated enhancement is due to injury-induced hypoxia. The contrast agent retention fraction is calculated as the fraction of pixels in the injury region with NDE values greater than the mean NDE + standard deviation of the conventional contrast agent cohort. The contrast agent retention fraction is used to discern the additional contrast retention of GdDO3NI

when compared to gadoteridol. The pre-injection and 3-hour post-injection scans were used to create 3D percentage contrast enhancement maps for each animal using the 3D Slicer software (http://www.slicer.org). A percentage enhancement range between 10% and 100% were used to display the 3D videos of hypoxic regions to show the spatial extent and degree of contrast retention. The videos are available through the following links https://www.youtube.com/watch?v=HdsRiracz58 represents the retention of Gadoteridol at the end of 3h and https://www.youtube.com/watch?v=VrLVv4Am2PM represents retention of GdDO3NI .

2.5. Statistics

All results are reported as means ± standard deviations (SD). Statistical comparisons were made between time-course gadoteridol and GdDO3NI data using analysis of variance (ANOVA). In pairwise statistical evaluations, the Tukey (α= 0.05, 95% confidence intervals) test was used between specific means.

2.6. Tissue Collection

The excision and fixing of the brain tissue was performed as reported previously[101]. Immediately after imaging, animals were deeply anesthetized with lethal dose of sodium pentobarbital solution. Once a tail pinch produced no reflex movement, animals were transcardially perfused with cold phosphate-buffered saline (PBS), followed by 4 % (w/v) buffered paraformaldehyde solution. Whole brain tissue was harvested and fixed overnight in 4 % (w/v) buffered paraformaldehyde solution. The following day, brains were immersed in 30 % (w/v) sucrose solution in 1X PBS for cryoprotection until the tissue was fully infiltrated. Samples were embedded in optimal cutting temperature medium and

frozen on dry ice. Samples were stored at −80°C until sectioned coronally at a 20 µm thickness with a cryostat (CryoStar™ NX70; Thermo Fisher Scientific) and collected onto positively charged microscope slides. Slides were retained in -80ºC refrigerator for further staining and analyses.

2.7. Histology and immunohistochemistry

Pimonidazole staining was performed using FITC-conjugated anti-pimonidazole antibody. The slides, which were kept in -80 °C were moved to the -20 °C freezer for 20-30 minutes. Then, they were moved to a 4 °C refrigerator for 15-20 minutes before being moved to room temperature PBS in a glass slide staining rack to avoid the temperature shock. The slides were moved to a tray and covered with the blocking buffer for 1 h. The slides were then washed using the waterfall technique with 1X PBS three times and were placed in the glass station filed with 1x PBS for 5 minutes and washed again. Following that, slides were placed in a tray and moved to 4 °C refrigerator and covered with 100 µL of the FITC conjugated anti pimonidazole antibody and incubation buffer mixture for overnight incubation.

Sections were then washed with 1 mL of 1X PBS for three times in a dimmed light room and incubated with the nuclear stain DAPI (4',6-diamidino-2-phenylindole)to help in identification of tissue in final visualization. Microscope images were acquired using a Leica microscope with 355-425 nm excitation / LP 470 nm emission filter for DAPI and 450-490 nm excitation / 500-550 nm emission filter for FITC.

3. Results

To verify the consistency of the TBI modeling, we calculated the injury volume for each cohort using MR images. T_2 wt MRI allowed for delineation of injury regions and quantification of injury volumes in the gadoteridol and GdDO3NI injected cohorts at 1 hr post-injury. The mean injury volumes for the gadoteridol and GdDO3NI cohorts were 4.82±0.50 mm^3 and 5.23±1.13 mm^3, respectively ($p>0.05$). Figure 2 shows the dynamic percentage enhancement maps of a representative animal from the gadoteridol (top row) and GdDO3NI injected animal over the course of three hours post-injection.

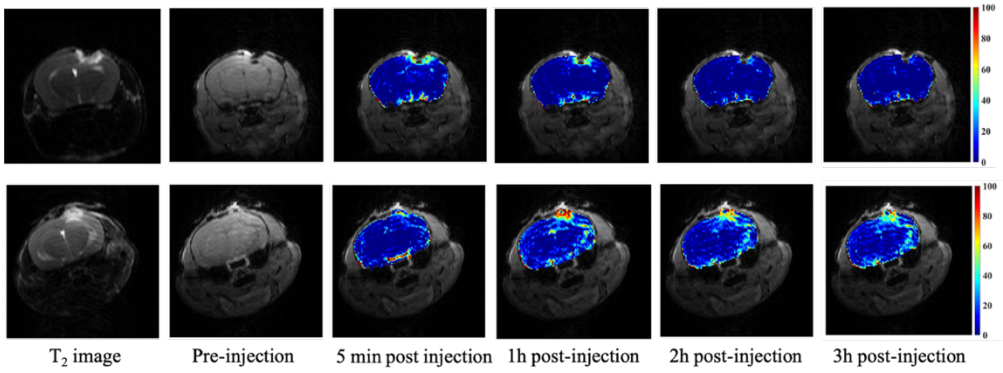

Figure 2. MRI T_2 weighted scout images and signal enhancement (%) overlay on T_1 weighted images of mice brains pre- and post-injection of conventional Gd agent gadoteridol (top row), and GdDO3NI (bottom row) over 3 hrs after injection. White arrow shows location of injury.

The region of interest (ROI) defining the injury region is indicated using a white arrow on T_2 weighted and T_1 weighted images. The color map overlay represents the percentage changes in pixel intensities with respect to the pre-injection value. Gadoteridol (Figure 2, top row) shows almost complete clearance from the injury region while

GdDO3NI (bottom row) shows significant accumulation at 3 hr post injection. Figure 5. a) demonstrates the mean time-course NDE of the two cohorts over three hours post-injection. Statistical analysis showed significant differences ($p < 0.05$) in NDE of the injury region after 150 min between gadoteridol and GdDO3NI cohorts. The distribution of pooled NDE values over all animals (Figure 5. 2b) further underline the differences between the two agents.

Animal #1

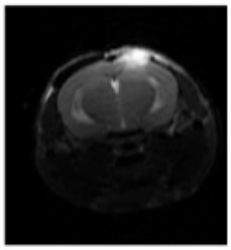

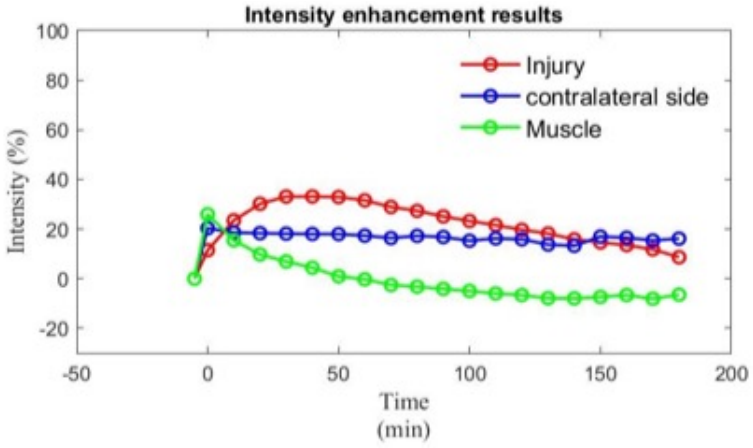

Animal #2

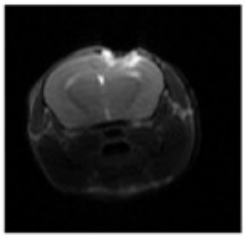

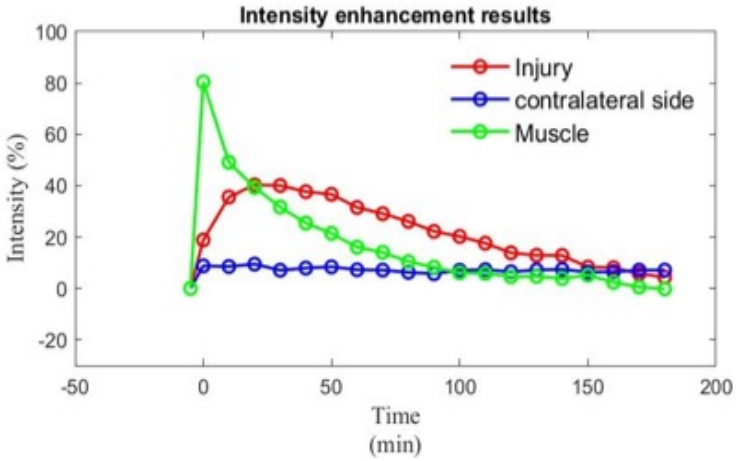

Animal #3

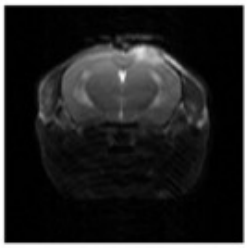

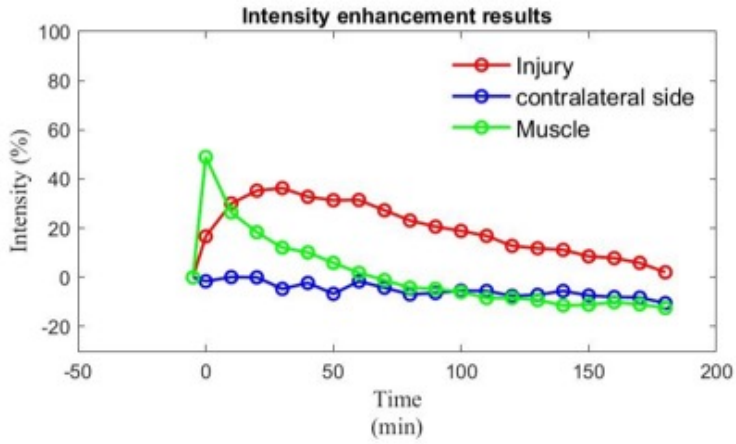

Animal #4

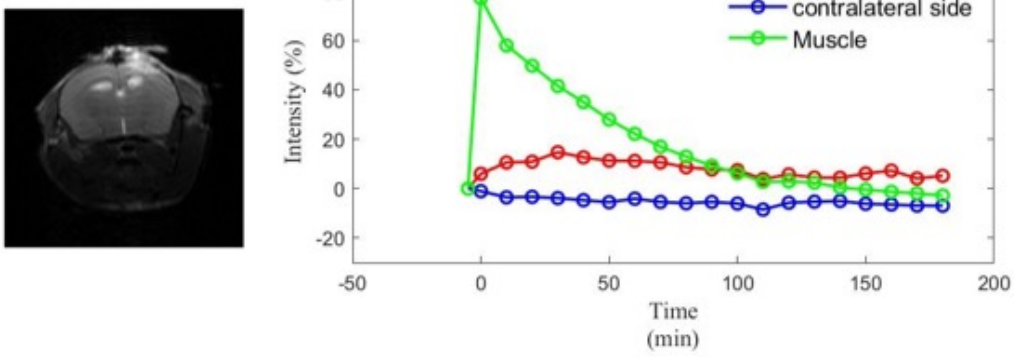

Animal #5

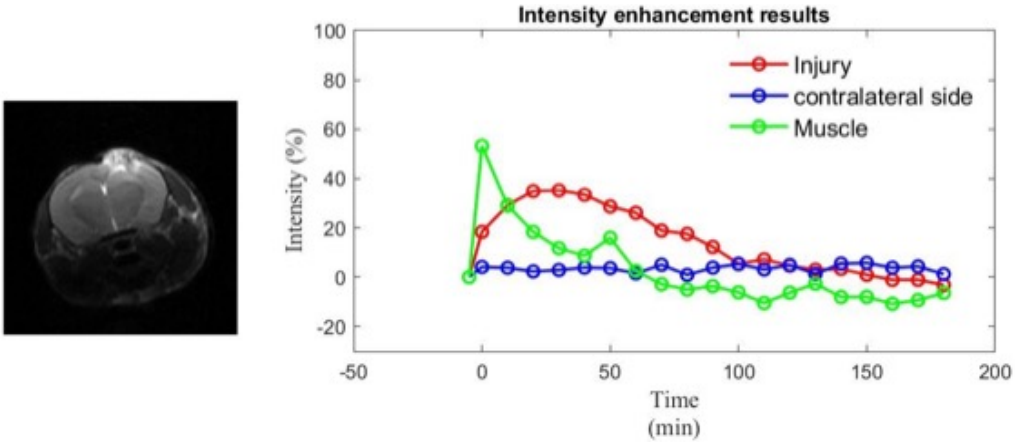

Figure 3. Signal intensity enhancement data in the injured brain, contralateral brain, and muscle regions (%) for the individual animals in the Gadoteridol cohort. Gadoteridol, the conventional, nontargeting contrast agent served as control in this study. The ROI analysis was a voxel-wise comparison and was performed in MATLAB by measuring the percentage enhancement of signal intensity in T_1 weighted images over three hours of the experiment compared to the pre-injection image.

Animal #1

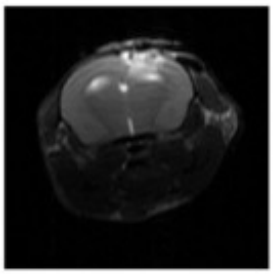

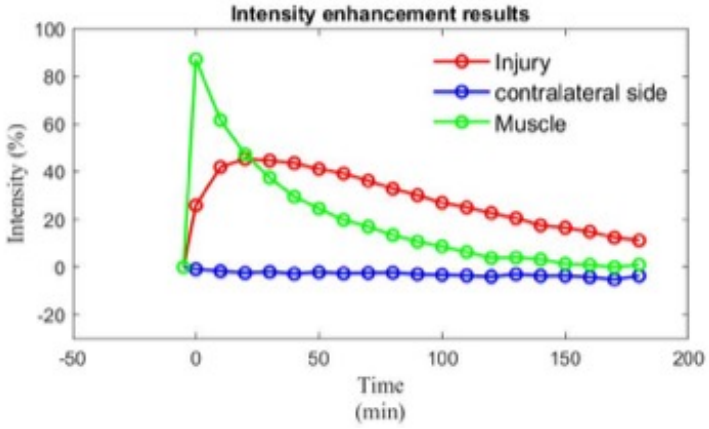

Animal #2

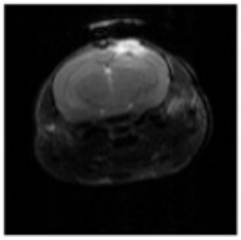

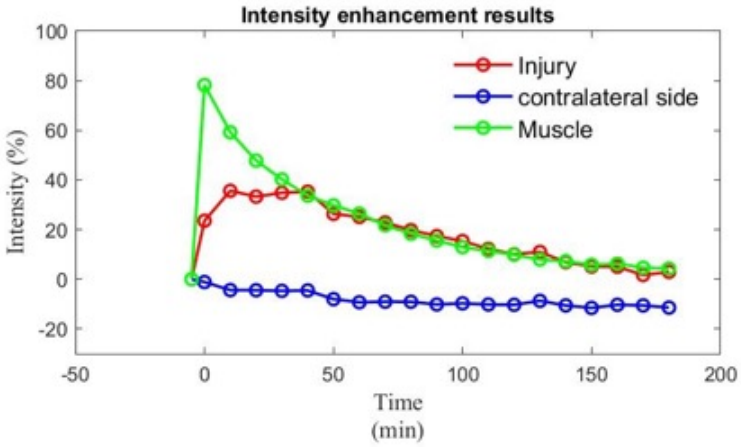

Animal #3

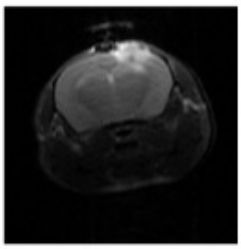

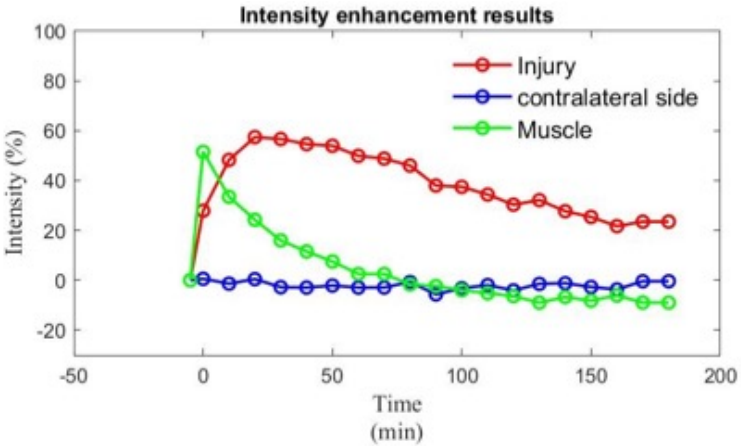

Animal #4

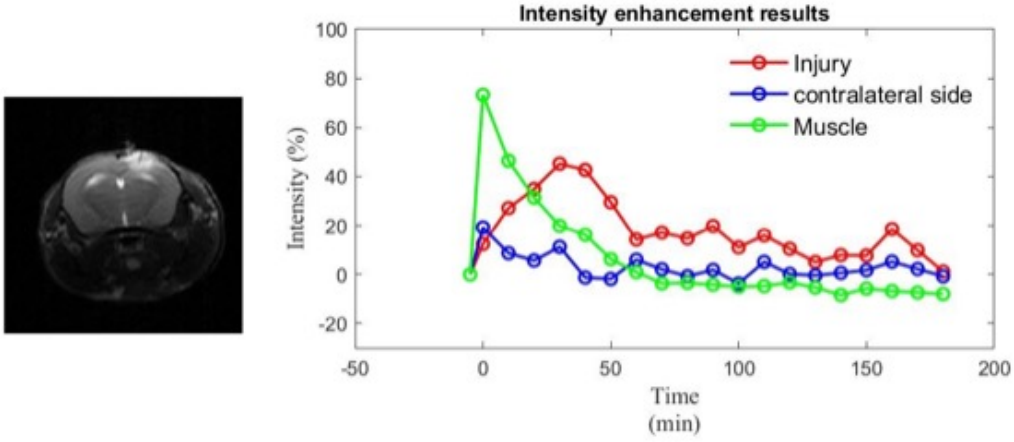

Animal #5

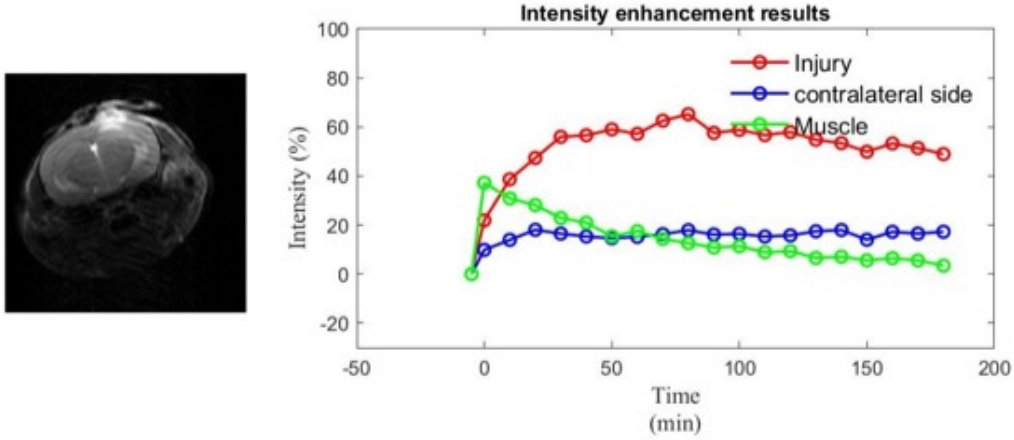

Figure 4. Signal intensity enhancement data in the injured brain, contralateral brain, and muscle regions (%) for the individual animals in the GdDO3NI cohort. The ROI analysis was a voxel-wise comparison and was performed in MATLAB by measuring the percentage enhancement of signal intensity in T_1 weighted images over three hours of the experiment compared to the pre-injection image.

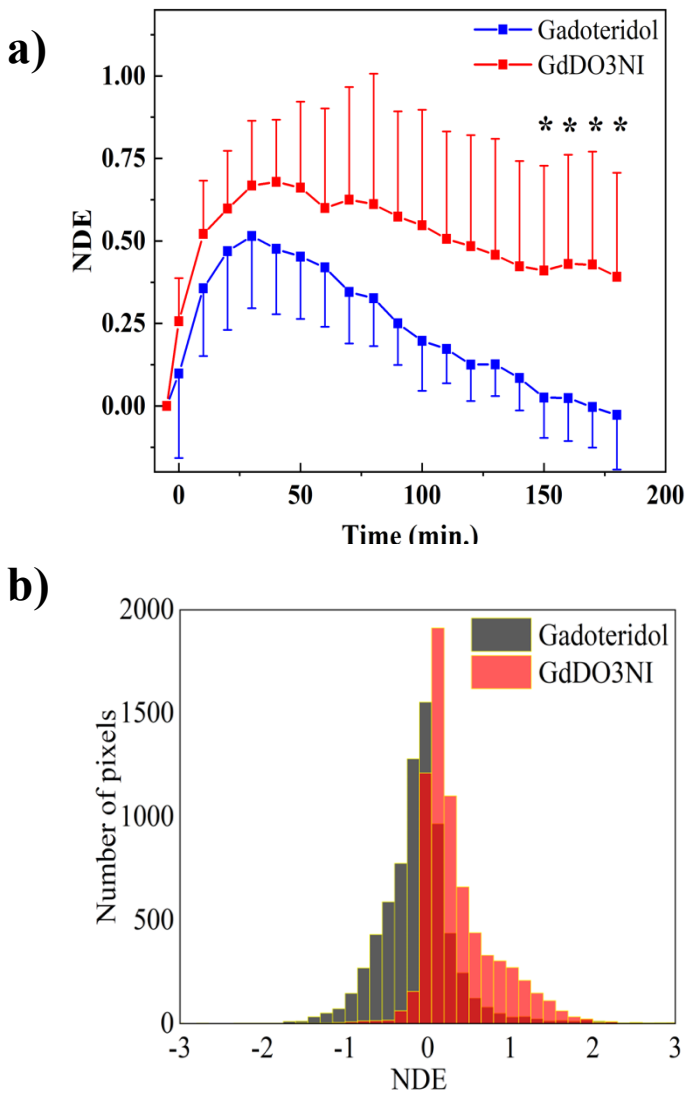

Figure 5. Time course mean normalized differential enhancement (NDE) results for gadoteridol and GdDO3NI injected cohort during 3 hrs after injection. NDE is calculated as the difference between the % enhancements of the injury region and a contralateral brain region of interest (ROI) normalized to the peak % enhancement for a muscle ROI . The ROI analysis for both contrast agents revealed changes in the signal intensity in injury site and muscle, but almost no changes in the healthy contralateral region over the three hours.

The intensity enhancement values in muscle showed rapid changes compared to the injury region that was slow and prolonged. Comparing the two cohorts (n=5) shows statistically significant retention ($p < 0.05$) of GdDO3NI in the injured region with significantly lower retention of gadoteridol at 150 minutes post-injection or later with the contrast agent retention factor values of 63.95±27.43 % and 20.68±7.43 %, respectively, at 3 hr post injection (4 hr post injury). In order to visualize the hypoxic regions in 3D, the maps of hypoxia and videos were generated. Figure 6 (a, b) illustrate the 3D visualization of percentage enhancement at 3 hr post-injection for a representative animal from each cohort which shows the difference between the enhancement of each contrast agent can be seen, and the volumetric extent of the contrast agent retention.

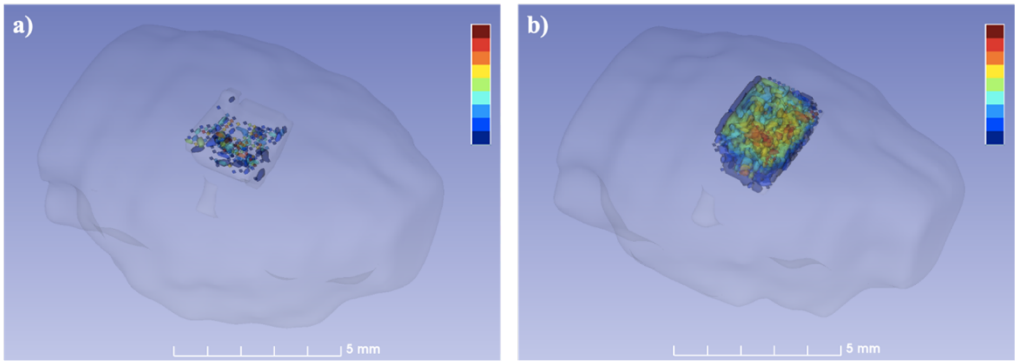

Figure 6. 3D rendering of hypoxic regions in brains of representative (a) gadoteridol and (b) GdDO3NI injected animal. Color scale represents percentage enhancement at 3 hrs post injection of respective contrast agent. 3D rendering shows both the spatial extent as well as the severity of hypoxia in the GdDO3NI cohort and the degree of residual agent retention in the gadoteridol cohort. Color scale= 10% -100%, scale bar = 5 mm.

Corresponding videos allow for complete visualization of the injury region within the brain. Table 1 summarizes the injury volumes, NDE and the contrast agent retention factor for each animal as well as the means and standard deviations.

Table 2. Injury volume, normalized differential enhancement and contrast agent retention fraction for each animal in the gadoteridol (control) and GdDO3NI cohorts.

Animal number	Injury volume (mm^3)	Normalized Differential Enhancement (NDE)	Contrast agent retention fraction (%)
		Gadoteridol	
# 1	4.68	-0.26	15.17
# 2	5.27	-0.04	13.41
# 3	4.58	0.16	32.37
# 4	4.20	0.10	21.71
# 5	5.40	-0.09	20.74
Mean	4.82±0.50	-0.03±0.17	20.68±7.43
		GdDO3NI	
# 1	6.81	0.89	51.25
# 2	5.66	0.41	45.32
# 3	3.77	0.18	93.67
# 4	4.69	0.18	36.32
# 5	5.22	0.13	93.20
Mean	5.23±1.13	0.36±0.32*	63.95±27.43*

We performed pimonidazole-based immunohistochemical staining of the brain sections for each cohort to study the presence of hypoxia and sections from corresponding representative animals in Figure 2 and Figure 6 are shown in Figure 7. The DAPI staining is presented in blue and pimonidazole staining in green. The results from both cohorts confirmed the presence of pimonidazole in the injury region.

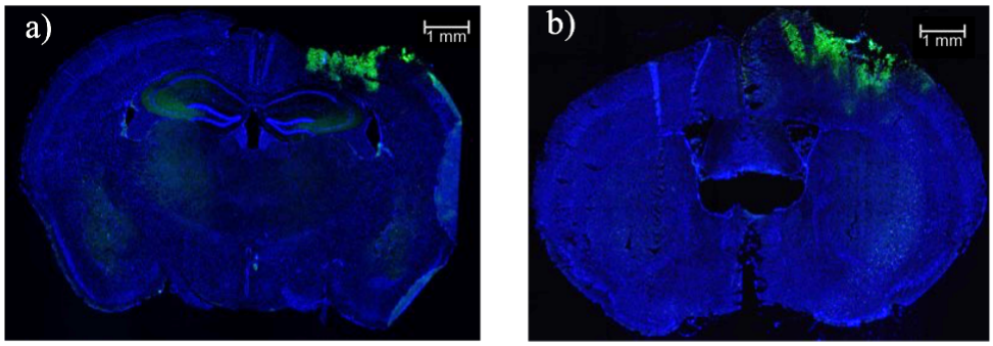

Figure 7 Immunohistochemical staining for hypoxia in injured animals (corresponding to fig 1), DAPI is visualized in blue and pimonidazole staining is visualized in green in representative animals injected with (a) gadoteridol or (b) GdDO3NI . Both cohorts display presence of hypoxia post injury. Scale bar = 1 mm.

4. Discussion and Conclusions

The mean volume of injury for gadoteridol injected cohort and the GdDO3NI injected cohort showed no statistically significant difference between the cohorts, indicating the consistency of the lesion volume and TBI modeling across the animals. Under normal physiological conditions, small molecular non-targeting Gd contrast agents such as gadoteridol, once introduced to the bloodstream, do not extravasate into brain tissue due to the tightly regulated BBB (unlike the muscle tissue). In pathologies that disrupt the BBB

(e.g TBI or brain tumors), dynamic contrast enhanced MRI shows accumulation and clearance of the contrast agent from the affected region enabling the estimation of BBB leakiness[102,103]. GdDO3NI and gadoteridol had similar, slower uptake pharmacokinetics in the brain injury region compared to muscle in each case. This observation can be attributed to the complex dynamic of the injured brain and blood flow disruption due to BBB dysfunction in the injury region compared to the intact muscle[104]. In contrast, the clearance pharmacokinetics of the two agents (GdDO3NI and gadoteridol) were markedly distinct in the injured brain while they were similar in the muscle region. In absence of hypoxia in the muscle, GdDO3NI behaves like any other small molecular MRI contrast agent, including gadoteridol with uptake/clearance kinetics that are predominantly flow-limited[105]. However, in the hypoxic injured region, the two agents behave differently, with GdDO3NI binding to proteins, via the 2-nitroimidazole moiety of the agent, showing significantly longer retention times compared to gadoteridol. This mechanism has been previously shown in prostate tumors as well where GdDO3NI was retained in hypoxic regions compared to a non-targeting Gd agent and enhancement patterns match pimonidazole IHC[2]. In the case of the current study, a qualitative comparison between the MRI and IHC images shows a good agreement between the location of T1 hyper-intensity regions within in the injury site in the GdDO3NI cohort and pimonidazole binding. The IHC results from both cohorts confirmed the presence of hypoxia post TBI; however, only animals in the GdDO3NI cohort were able to represent that in MRI contrast enhancement studies. These observations confirm our hypothesis that GdDO3NI localizes in hypoxic regions in TBI.

Our results showed the contrast agent retention factor was significantly different in the two cohorts. The contrast agent retention factor represents the fraction of voxels with an NDE of about 15% or more (mean NDE for gadoteridol + standard deviation) which reflects the amount of contrast agent in the injury region at the 3 hr post injection. In case of the gadoteridol-injected cohort, animals showed contrast retention in ~ 15-30 % of voxels in the injury region while that in the GdDO3NI was 36-94% of voxels in the injury region but with much higher mean NDE values. This indicates that GdDO3NI is retained in a larger number of voxels at 3hr post injection and at higher concentrations which can only be attributed to binding in the hypoxic regions. It is to be noted that while we see significant differences in the retention of gadoteridol compared to GdDO3NI , the former does not appear to be completely eliminated possibly due to the irreversible retention[102]. The dynamic nature of the BBB dysfunction can influence the amount of exogenous agents that are able to wash in or wash out, even over a matter of hours post injury, due to dynamic reduction in BBB leakiness[106]. In case of the GdDO3NI the retention fraction is related to the hypoxic fraction but, unlike tumors, it may overestimate the hypoxic fraction due to some degree of irreversible retention arising from acute reduction in BBB leakiness over 3 hrs since the contrast agent was injected (as seen for the control agent, gadoteridol).

In summary, the results demonstrate that contrast enhanced MRI using GdDO3NI allows visualization of hypoxic regions in the brain following TBI. The MR results were validated by the gold standard method of IHC staining for pimonidazole. Non-invasive imaging of hypoxia in TBI could allow for injury prognosis as well as personalized treatment targeted towards alleviation of hypoxia.

CHAPTER 3

ASSESSMENT OF HYPOXIA IN TWO DIFFERENT TYPES OF BRAIN TUMORS

Purpose: Here, we assessed the tumor hypoxia in 9L and C6 tumor models in rat brain using GdDO3NI with dynamic contrast enhancement (DCE)-MRI method. The MR results were validated with two available gold standard imaging modalities, 18-fluoromisonidozole (^{18}F-FMISO) in positron emission tomography (PET) and immunohistochemical assay of pimonidazole in confocal microscopy.

Methods: The tumors were implanted intracranially. The animals were imaged at 7 T to monitor the tumor growth. Approximately 21 days post implantation the animals were imaged with PET and on the following day were intravenously injected with GdDO3NI at 0.1 mmol/kg dose (n=8 for each cohort) and imaged for 2h. The regions of interest were drawn on the brain tumor region, the contralateral brain as well as on the cheek muscle for the comparison of contrast kinetics. After the MR experiment animals were injected with pimonidazole the brains were harvested 1h post injection of pimonidazole for immunohistochemical assay.

Results

In this study the results of immunohistochemistry and PET are in good agreement with the result of hypoxia targeting contrast agent. We saw hypoxia in the big 9L tumor in all three techniques. 2h post injection in big tumor showed higher enhancement, which can be ascribed to the retention of the targeting contrast agent in the tumor. The big tumor ROI showed about 15% enhancement at two hour time points, distinctly different from muscle

enhancement with about 7%. However, at the same time point for the small tumor, there was almost no difference between the muscle and tumor enhancement.

Conclusion

We showed GdDO3NI enhancement patterns matched pimonidazole staining. We verified the performance of GdDO3NI with PET and immunohistochemistry. Our result showed the relation between the tumor size and severity of hypoxia.

1. Introduction

Glioblastoma multiforme (GBM) is the most common and deadliest type of primary malignant brain tumor. Its prognosis remains grim, and most patients with GBMs die of their disease in less than a year even if they receive advanced treatments like surgery, adjuvant radiotherapy, and chemotherapy[107(p1)]. The hypoxic microenvironment is one of the important features of brain tumors, which is shown to correlate with tumor aggressiveness[108]. It occurs due to the leaky and chaotic vasculature network in the tissue. Tumor microenvironment because of high proliferative cells and lack of genetically built-in checkpoints that control the functionality of the cells is conducive to underdeveloped and malfunctioning structures and heterogeneous environment compared to normal tissues. Studying the tumor microenvironment can shed light on drug development, and choosing effective treatment for patients. A chronic hypoxic microenvironment in solid tumors, i.e. an imbalance in supply and consumption of oxygen resulting in oxygen deficit, leads to changes in tumor cell metabolism and upregulating pro-survival proteins which in turn increase angiogenesis, proliferation, invasion, and metastases[109]. In the aftermath of hypoxia, tumors' response to commonly effective and practiced therapies like chemo- and

radio therapy is not satisfactory or favorable. Since hypoxia results in resistance to chemotherapy, a better understanding of the tumor microenvironment and detection of hypoxia could improve the current anticancer treatment strategies[110]. For example, there are special drugs termed hypoxia activated prodrugs, developed that selectively target hypoxic regions. These drugs can improve the response of the tumors to radio- and chemo-therapy. Knowledge about hypoxia can improve the prognostic accuracy and be used in the development of personalized therapies. There are numerous methods and techniques to study hypoxia and oxygenation each with its pros and cons. The gold standard to study oxygenation is the polarographic fibers. The importance of hypoxia has attracted interest from many research groups to develop novel techniques to study tissue hypoxia. Among various procedures to detect hypoxia like, oxygen microelectrode, oxygen-dependent DNA strand break, and hypoxia marker techniques[85], the immunohistochemical hypoxia marker technique[50] has shown the most promising results in detecting hypoxia, which is universally defined as oxygenation less than 10 mmHg. The above-mentioned techniques are either invasive or nondynamic. The clinically approved noninvasive approach to detect hypoxia is positron emission tomography (PET) using hypoxia targeting tracers like FMISO and FAZA. The imaging based noninvasive approaches in studying hypoxia are advantageous mainly because they do not cause any medical complications compared to invasive techniques and the studies are not time consuming. In order to avoid the invasive nature of the most reliable techniques researchers are in quest of noninvasive methods. For instance, [18F] FMISO and [18F] FAZA are nitroimidazole derivate tracers in PET, which have been used for detecting tissue hypoxia noninvasively[111–114]. Even though PET scans

reveal metabolic changes at the cellular level it does not reveal detail information about the anatomy of the pathology. Moreover, PET scans are expensive and the scanners are usually dedicated to oncology departments and their availability to study hypoxia in other pathologies might be limited[52]. Magnetic resonance imaging (MRI) is a noninvasive imaging modality that can also be utilized to assess hypoxia[2,61]. MRI provides high resolution images compared to PET and dynamic information about the tumor microenvironment. Dynamic contrast-enhanced (DCE) MR is a quantitative MR based technique to study the T_1 changes of a tissue. To this end, multiple images are acquired before, during and after injection of a contrast agent[115]. The well investigated parameter in DCE-MR is K^{trans} that representative of contrast agent diffusivity across endothelium[116]. The diffusion of the contrast agent to the extracellular space and its clearance can be calculated through the changes in the MR signal in the region of interest. The blood brain barrier (BBB); however, is not permeable to most of the contrast agents. The signal changes in healthy brain tissue after a contrast agent injection is not attributed to contrast agent extravasation to the tissue but it is because of contrast agent present in the blood pool. On the other hand, in the regions of the brain that the BBB is compromised because of tumor, brain injury and infection the contrast agent enhances the signal in BBB compromised regions. The signal enhancement is influenced by the amount of blood flow to the tissue, the surface area per unit mass of tissue (*S*), and the permeability (P) of the tissue and their combined effect is K^{trans}. The calculated parameters from DCE-MRI are extremely helpful and informative to characterize tumor microenvironment, stage of the tumor, and monitoring tumor response to a treatment[117]. For example, it is recommended to study

K^{trans} while monitoring the efficacy of anti-angiogenic therapies[118]. The DCE-MR analysis requires accurate measurements of the contrast agent concentration in blood plasma also known as arterial input function (AIF), which is the primary challenge in DCE-MR calculating AIF is described as notoriously difficult[115]. The main challenges to calculate AIF accurately can be summarized as the need for high temporal resolution in data acquisition, the need for a vessel in the vicinity of the tumor, and any motion of the vessel can also affect the AIF measurements. To avoid the hurdle of AIF measurements there are some models called reference region (RR) models developed to eliminate the need for direct AIF measurements[115,119]. Here, we aim to determine the hypoxic tissue in two different brain tumor models, using GdDO3NI and verify the accuracy of the detection with PET and IHC assay of pimonidazole. The PET studies are conducted with ^{18}F-FMISO, a hypoxia targeting tracer[120],which uses the similar hypoxia-targeting moiety as GdDO3NI . In addition, to study perfusion of the tumor and its microenvironment we model and extract the pharmacokinetic parameters of the tumors using DCE-MRI and hypoxia targeting contrast agent. Based on the parameters the perfusion and hypoxia levels in tumors are assessed with the MRI approach and noninvasively. The results of this study can be used for improved personalized therapy, especially for treatment with hypoxia-activated prodrugs, and radiotherapy.

2. Materials and methods

2.1. Materials

Wistar and Fisher rats were 5–9 week-old when purchased from Charles River Laboratories (Wilmington, MA). The FMISO trace was obtained from the St. Joseph Hospital and

Medical Center (Phoenix, AZ). GdDO3NI was synthesized and used in this study as described previously[61].

2.2. Relaxivity measurements

The relaxivity of synthesized GdDO3NI was measured at 7T using a preclinical Bruker MRI scanner. Briefly, a home-made 3D printed MR compatible phantom, which could provide control over the sample temperature containing nine different concentrations of the contrast agents in water was used to measure the contrast agent's relaxivity. The acquired images had the following parameters a matrix size of 64 × 64, the field of view 2.56 cm × 2.56 cm and TR=205-5000 ms, TE=10 ms for the T_1 map and TR=5000 ms, TE=8-200 ms for the T_2 map. The images were analyzed and processed in MATLAB to calculate the T_1 and T_2 values for each pixel. Using the T_1 and T_2 maps vales and the known concentrations the relaxivity values were calculated by a linear fit on R_i and [C][58].

2.3. Animal models

All animal studies were performed in accordance with Institutional Animal Care and Use Committee approved animal protocol. Female Fischer rats (n=8) were inoculated with 9L and Wister rats (n=8) with C6 tumors, as described previously[109]. Briefly, C6 and 9L cells were collected and resuspended in phosphate buffered saline (PBS). Each animal was injected with 60,000 cells in a volume of 4ul in the brain. To monitor the efficacy of the implantation and the tumor growth the animals were imaged with In Vivo Imaging Systems (IVIS) a week after implantation.

2.4. PET and MRI

Imaging was performed on 18 or more days of post implantation. PET images were acquired on a Bruker Albira Si 3 ring preclinical PET scanner with the same procedure described in Scarpelli et al. paper[121]. In brief, PET images of the brains were acquired dynamically from 0 to 110 minutes simultaneously with bolus injection of ^{18}F-FMISO. Afterwards, the images were reconstructed with an ordered subset expectation maximization algorithm which was modified to account for scattering, dead time, and decay of the tracer. MRI was performed at 7 T on a preclinical Bruker MR scanner on the following day of PET imaging. Anatomical imaging was performed using a T_2-weighted spin echo sequence with the following parameters: TR= 6.4s, TE= 50ms, averages= 4, matrix = 128x128, FOV=3.2cm×3.2cm, thickness = 1mm. The DCE study was performed using a Fast low angle shot (FLASH) sequence with TR=100ms, TE=2.5ms, matrix = 64×64, FOV=3.2cm×3.2cm and a flip angle of 40 degrees.

2.5. Immunohistochemistry assay

At the end of the DCE-MRI experiment the animals were injected with 60mg/kg pimonidazole HCL and transcardially perfused one hour later with a mixture of phosphate buffer and heparin (100 U/mL) immediately after blood clearance from the system a solution of 4% paraformaldehyde (PFA) was used to start the fixing process in situ. The harvested brains were then immersed in PFA solution overnight. The fixed tissue was washed and stored in phosphate buffer. Later, the brains were sliced into 1mm coronal sections. The tissue was cleared using a CUBIC (clear, unobstructed brain imaging cocktail) based protocol[122] for 10 days, washed in 0.1M PB and incubated in a 1:50 dilution

of FITC-MAb1 (Hypoxyprobe) in 0.1% PBTX for 2.5 days. Following antibody incubation tissue was placed in EasyIndex (LifeCanvas Technologies) and imaged using IVIS spectrum imaging system with excitation and emission spectrum wavelengths of 570/620nm for detecting Tdtomato, which was expressed in the stably transfected tumor cells, and 500/540nm for detecting FITC in hypoxic regions.

2.6. Image and data processing

Image analysis was performed using built in-house algorithms with MATLAB. The regions of interest (ROI s) for the tumor, contralateral brain, and muscle were drawn on the anatomical MR images on all the slices covering the tumor and used to extract data from pre-injection T_1 maps and the DCE images. Data analysis was performed on the ROI s to calculate the tumor volume, normalized differential enhancement (NDE)[28]. NDE is used to reduce the effect of potential variability of the delivered contrast agent on each animal. A conditional smoothening algorithm in MATLAB was applied to the DCE-MR data to reduce the noise and retain the vital information like the initial jump in contrast enhancement following the bolus injection. To eliminate the apparent drift in the time course data, the first 50 points and the final 50 points of the contrast-enhanced data of the contralateral brain were used to fit a linear equation. The resultant line was subtracted from the contrast enhancement data of all three ROI s. After noise reduction and drift correction, the data was used for pharmacokinetic modeling to compute K^{trans} values.

2.7. Pharmacokinetic modeling

To study the distribution of conventional i.e., nonspecific contrast agents the concentration of plasma and tissue of interest is used to compute pharmacokinetic constants using Equation 1:

$$\frac{dC_T}{dt} = K_T^{Trans} C_p - \frac{K_T^{Trans}}{\nu_e} C_T \qquad \text{Equation 1}$$

Where C_T is concentration of contrast agent in tissue of interest and C_p is the concentration in plasma. In the proposed formula the main issue, considering the accuracy of the model, rises from calculating $C_p(t)$. In order to calculate C_p there should be a large vessel or artery in the slice of MR image and using the blood signal C_p can be calculated. However, even if there is a blood pool in the MR slice the results still would differ because of differences in the location of ROI , the number of pixels included in the calculations, and in flow effects. To avoid this questionable situation, Yankeelov et.al[115] used a reference region approach to eliminate the need for direct measurement of C_p from a large vessel in FOV.

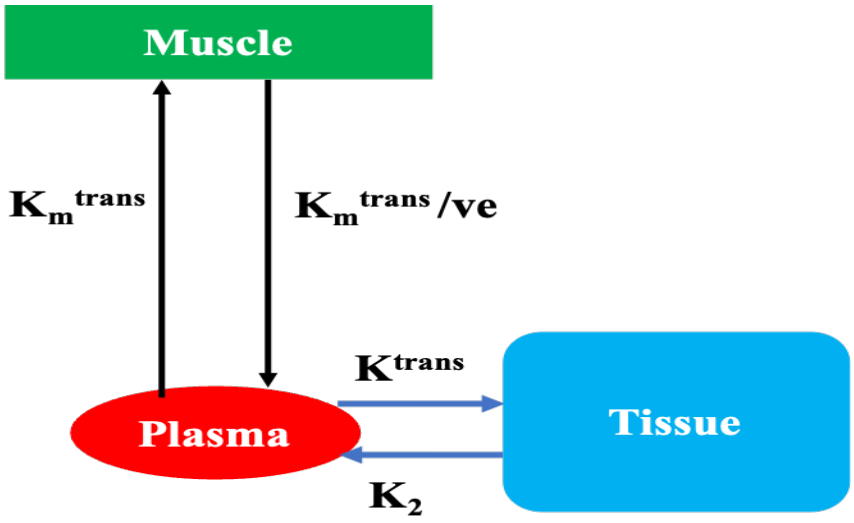

Scheme 2. The proposed model for extravasation of targeting contrast agent

In this method a reference tissue such as muscle whose pharmacokinetic properties is well characterized in the literature can be used to simulate C_p. The model is shown in Scheme 2. For conventional contrast agents the reference region model is written as the following equation system.

$$\begin{cases} \frac{dC_m}{dt} = K_m^{trans} C_p - \frac{K_m^{trans}}{v_e^m} C_m \\ \frac{dC_T}{dt} = K_T^{trans} C_p - \frac{K_T^{trans}}{v_e^T} C_T \end{cases} \qquad \text{Equation 2}$$

Where C_m is the concentration of contrast agent in muscle; C_p concentration in plasma; K_m^{trans} and K_T^{trans} are transfer constants for muscle and general tissue; v_e^m and v_e^T are the extracellular and extravascular space volume fraction.

However, the equations are very simplified and do not capture the plasma volume fraction (v_p) term in the simulation. The v_p is about 1-2% in normal and healthy muscle tissue while

it changes significantly in other tissues specifically in tumors. Here we are using a modified version of the reference region tissue approach to calculate C_p and pharmacokinetic parameters for the targeting contrast agent.

The important concern of this situation is that the signal measured is interpreted as a sum of all the contributing compartments. Measurement of concentrations in the individual compartments hypoxic fraction and normoxic fraction are impossible[123]. To overcome the issue we assume the efflux K_2 value captures the combination of transfer consonants for the hypoxic and normoxic portion of the tissue. As mentioned above the v_p of muscle is 1-2% and in most pharmacokinetic modeling studies the blood volume fraction is neglected for muscle tissue. The modified form of the equations for using reference region can be written as:

$$\begin{cases} C_p(t) = \dfrac{1}{K_m^{trans}} \dfrac{dC_m(t)}{dt} + \dfrac{1}{v_e^m} C_m(t) & \text{Equation 3} \\ C_T(t) = K^{trans} \displaystyle\int_0^t C_p(u) e^{-K_2(t-u)} du + v_p C_p(t) & \text{Equation 4} \end{cases}$$

Equation 4 can be written as follows[124] to make it a linear equation:

$$C_T(t) = [K^{trans} + K_2 v_p] \int_0^t C_p(u) du - K_2 \int_0^t C_T(u) du + v_p C_p(t) \qquad \text{Equation 5}$$

Substituting Equation 3 in Equation 5 eliminates the need for direct measurements of plasma concentration.

The final equation can be written as:

$$C_T(t) = [K^{trans} + K_2 v_p] \int_0^t [\frac{1}{K_m^{trans}} \frac{dC_m(u)}{du} + \frac{1}{v_e^m} C_m(u)]du - K_2 \int_0^t C_T(u)du + v_p C_p(t) \quad \text{Equation 6}$$

Using MATLAB programming we can solve the above equation with the least square method to fit the three parameters K^{trans}, $K_2 v_p$ and K_2.

In order to use MRI data to calculate the pharmacokinetic constantans we need to obtain concentration maps from DCE-MR images. With the computed pre-injection T_1 map of the brain, and equation between the relaxation rate and relaxivity $R_1 = r_1[C] + R_0$

Where R_1 is relaxation time equal to the inverse of T_1 and r_1 is relaxivity of the contrast agent and a known constant value the C(t) for each pixel can be calculated.

The signal detected in MRI has the following general form for the gradient echo sequence, a widely used sequence for dynamic contrast enhancement.

$$S(t) = \frac{S_0(1 - e^{\frac{-T_R}{T_1}})}{1 - e^{\frac{-T_R}{T_1}} cos\alpha} e^{\frac{-T_E}{T_2^*}} \sin\alpha \quad \text{Equation 7}$$

Where α is the flip angle, and S0 is a constant describing the scanner gain and proton density. To minimize the T_2^* effect we choose short TE to have the data insensitive to the T_2^* effect.

$$S(t) = \frac{S_0(1 - e^{\frac{-T_R}{T_1}})}{1 - e^{\frac{-T_R}{T_1}} cos\alpha} \sin\alpha$$ Equation 8

If we acquire a T_1map of the slice before injection, we can find S_0 and $T_1$for each voxel.

If we substitute 1/ T_1=R_1 in Equation 8, it will be:

$$S(t) = \frac{S_0(1 - e^{-T_R \times R_1})}{1 - e^{-T_R \times R_1} cos\alpha} \sin\alpha$$ Equation 9

TR and α are fixed values we get S(t) from the image and we can calculate R_1 of each voxel over the experiment period. Once R_1(t) is computed subsequently C(t) can be obtained. Using the concentration of muscle region and the concentration of tissue in each pixel the pharmacokinetic parameters can be calculated.

2.8. Statistical analysis

Results are presented as means ± standard deviation for the rats. Individual groups were statistically compared with t-test and the results with $p<0.05$ were considered significant.

3. Results

The synthesized contrast agent was characterized with NMR, Mass spectroscopy and Inductively Coupled Plasma (ICP) to ensure its originality. After chemical characterization techniques the relaxometry experiment was performed on each batch of the contrast agent Figure 8 shows the result of the relaxometry experiment. The experimental data and the linear fit showed a good correlation with an r^2 value of 0.9 for the both batches.

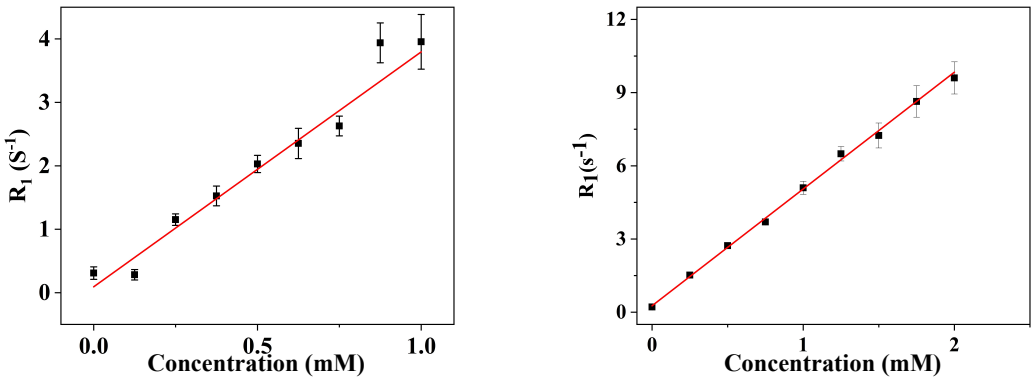

Figure 8. T_1 relaxometry of two batches of GdDO3NI at 7 T at 37 ℃, the equation for the line on the left graph is R_1=0.09+3.70[C] and for the right graph is R_1= 0.26+4.78[C].

Figure 9 shows the comparative view of intensity enhanced region in three different imaging modalities with respective agents in a big and a small tumor. The figure shows pimonidazole based IHC using microscopy, ^{18} F-FMISO using PET and GdDO3NI using MRI. The MR based image is the overlay of intensity enhancement image at 2h on T_2 anatomical MRI. The smaller tumor showed little to no hypoxia in IHC and PET images[109], while the large 9L tumor exhibits considerable hypoxic regions in the two gold standard approaches for hypoxia imaging. In each case the MR results correlate well with the IHC and PET.

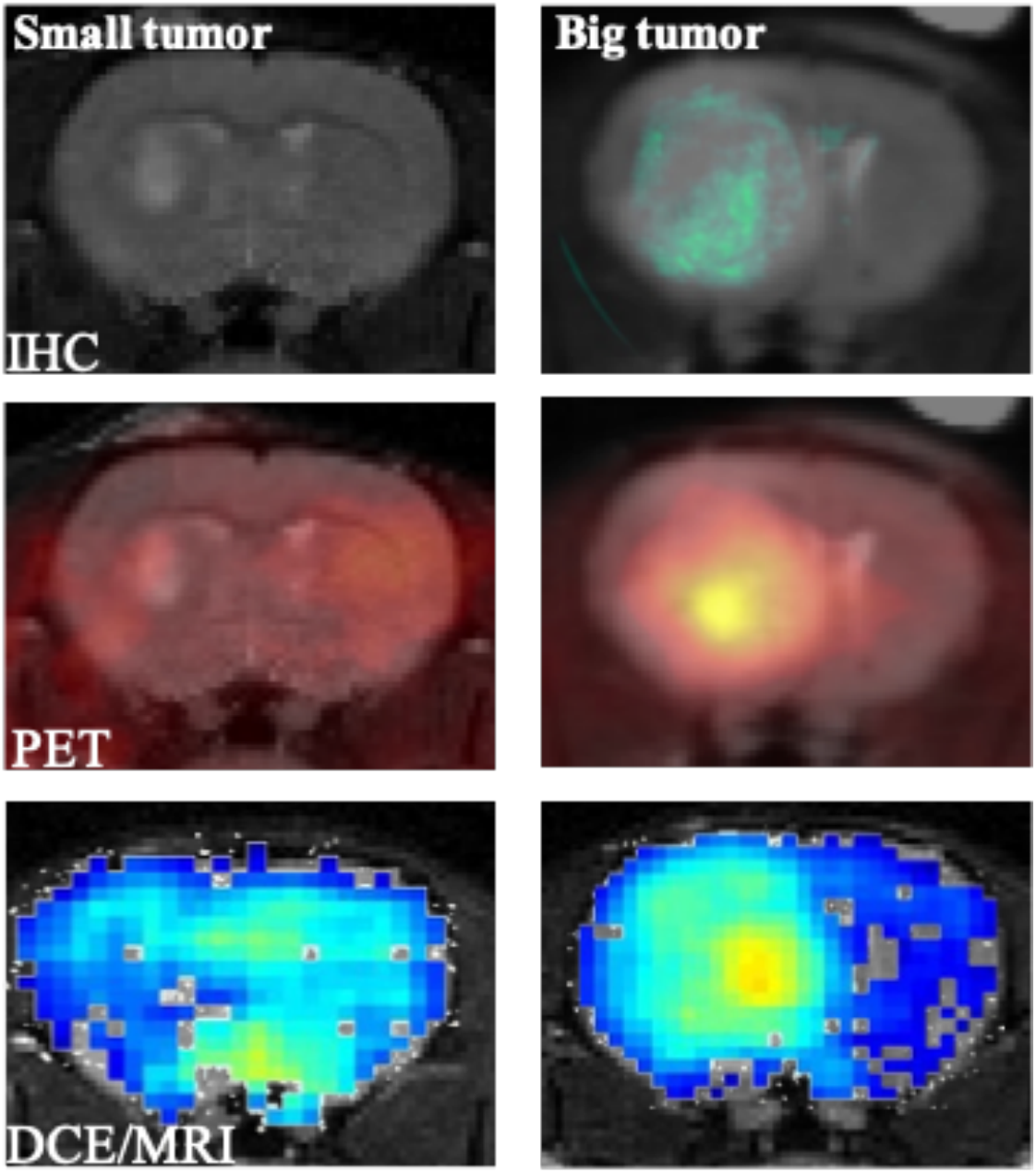

Figure 9. The left is representative of the small 9L tumor from top: pimonidazole staining overlaid on MRI T_2, PET scan overlaid on MRI, MRI and the difference image of before injection and the 2h post injection time point. The right is representative of the big 9L tumor from top: pimonidazole staining overlaid on MRI T_2, PET scan overlaid on MRI,

MRI and the difference image of before injection and the 2h post injection time point. The IHC and PET images are acquired by Dr. Matthew Scarpelli.

Figure 10 demonstrates the time course data for intensity enhancement on the three different ROI s: tumor, contralateral brain, and muscle on the representative animals. ROI s analyses in MATLAB were performed by measuring the percentage enhancement of intensity in T_1 weighted images compared to the pre-injection images.

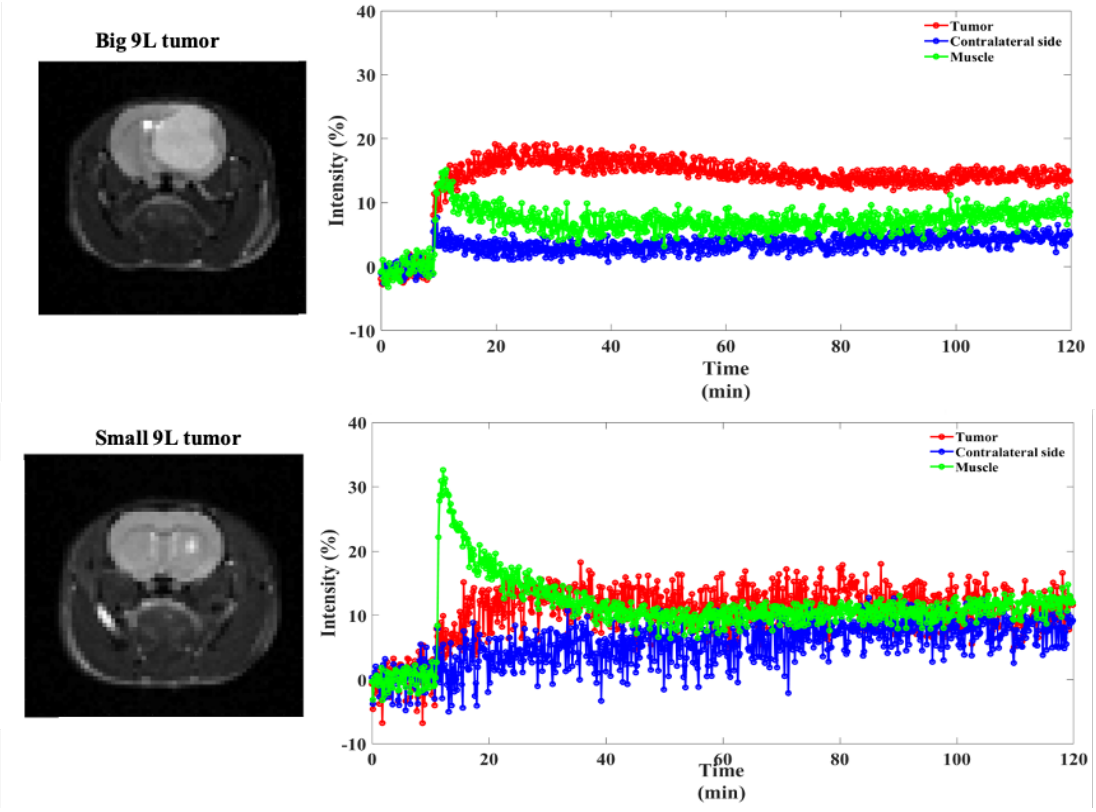

Figure 10. Percentage enchantment results from DCE experiment over 2h, representative of big(top) and small(bottom) tumors.

As shown in Figure 10 the curves are noisy and there is a slight drift in the data, which can influence the results of the pharmacokinetic modeling. To assess the drift we ran the same sequence with the same parameters to acquire images from a water phantom. Figure 11

visualizes water phantom on the left, the ROI marked in the red and blue region are for water and noise respectively, the intensity enhancement graphs for the water and noise region (top graph) shows no changes to the water signal during 2h of scan time. However, looking closely at the water data (bottom graph) reveals about 1.5% increase in intensity enhancement.

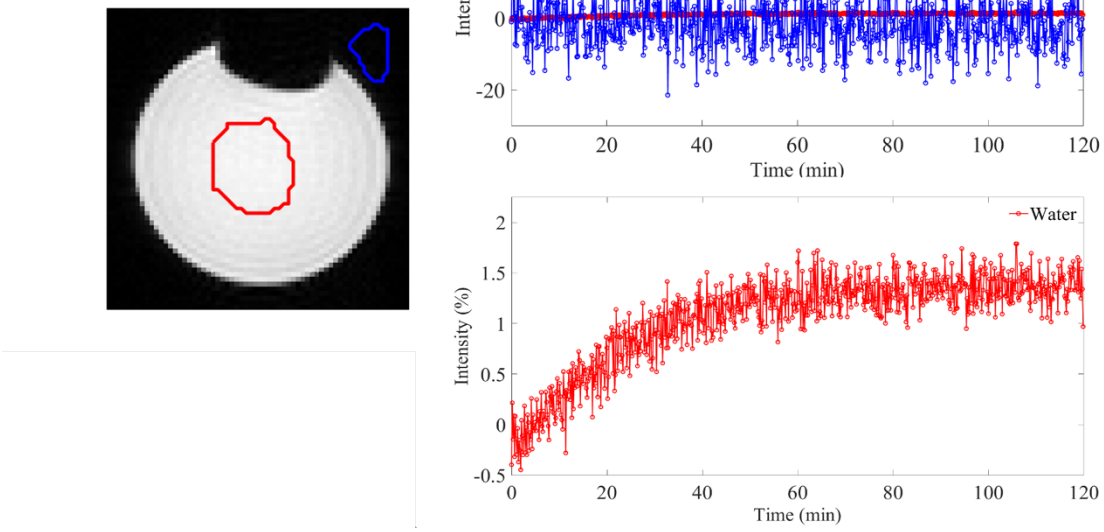

Figure 11 Water phantom and result of DCE sequence running for 2h.

To reduce the noise and compensate for the drift in the data, we employed a conditional moving average algorithm. The algorithm's conditionality helps capture the critical information in the data, such as the sharp rise time, specifically in the muscle. The algorithm calculates the standard deviation of the data in the first 10 min (before injection). It then applies a moving average with n=5 to the points that show changes less than twice the calculated standard deviation. To reduce the drift, the algorithm uses the first 50 points

and last 50 points of the contralateral data (blue curve) to fit a linear equation; then, all the data sets were subtracted from the obtained linear equation. This approach ensures the contralateral brain's endpoint lands very close to 0% enhancement, eliminating the data's drift. The corrected data sets for the noise and drift after applying the conditional smoothening algorithm are summarized in Figure 12 and Figure 13.

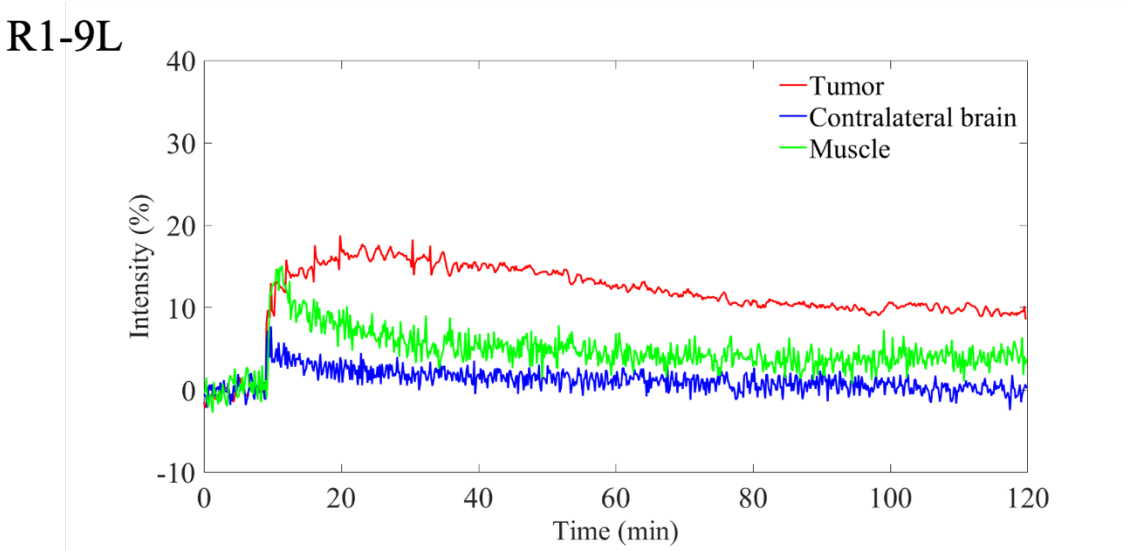

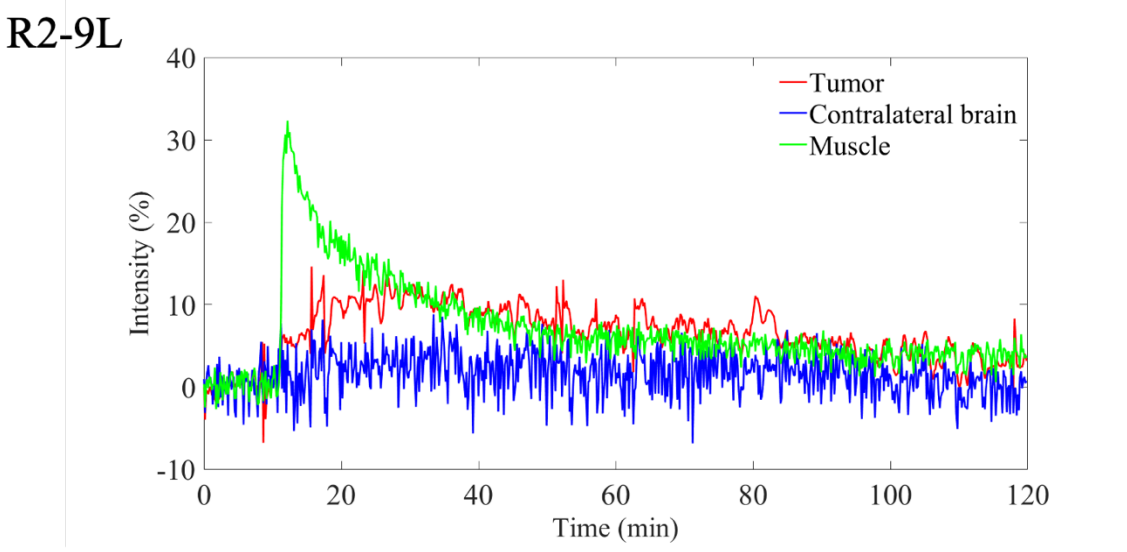

R5-9L

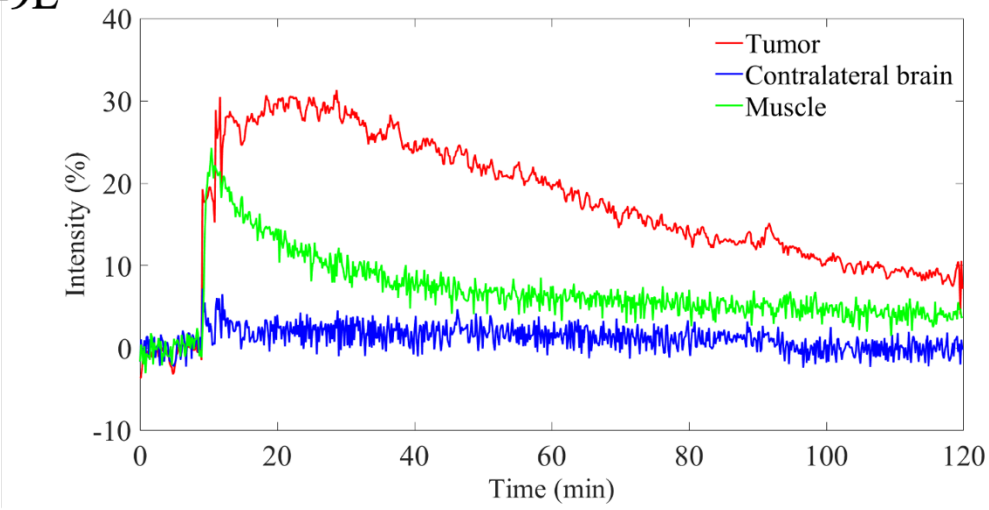
Tumor
Contralateral brain
Muscle
Intensity (%)
Time (min)
40
30
20
10
0
-10
0
20
40
60
80
100
120

R204-9L

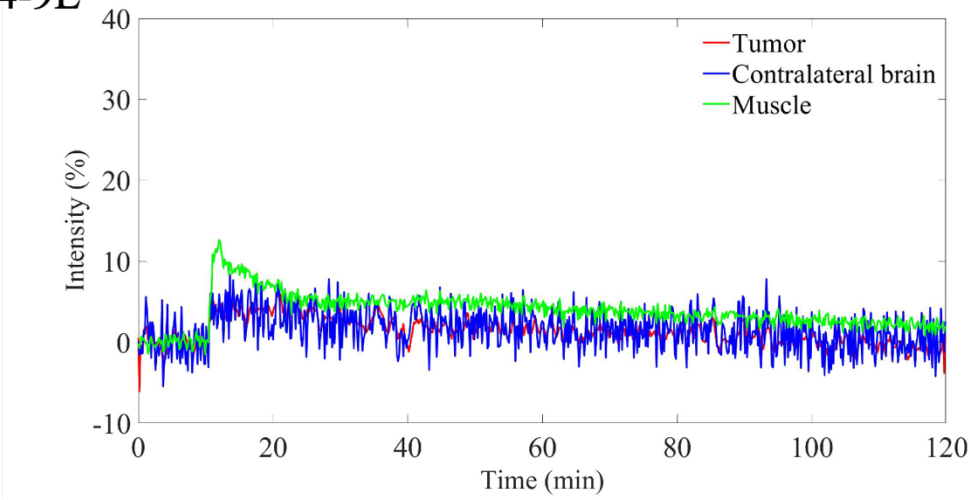
Tumor
Contralateral brain
Muscle
Intensity (%)
Time (min)
40
30
20
10
0
-10
0
20
40
60
80
100
120

R206-9L

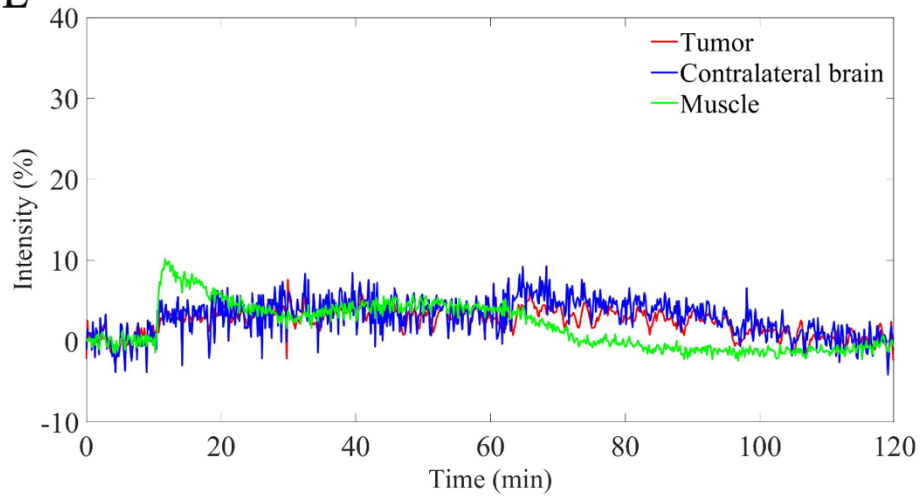

R208-9L

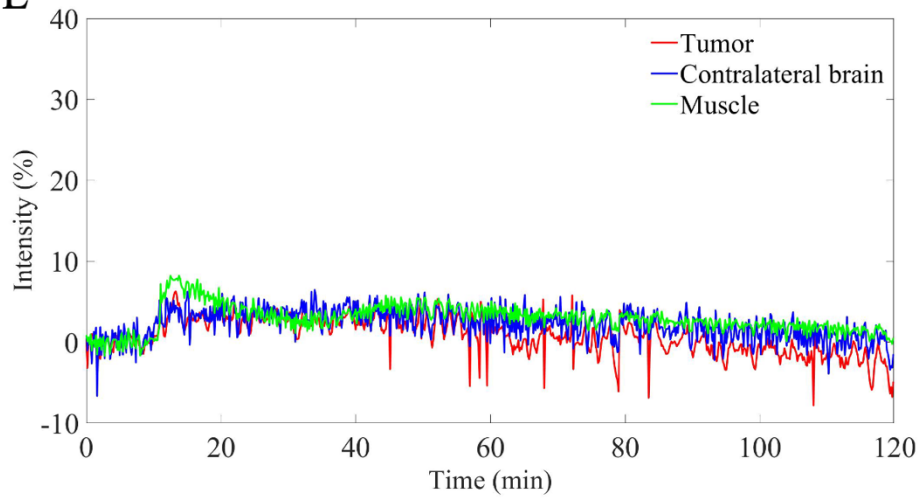

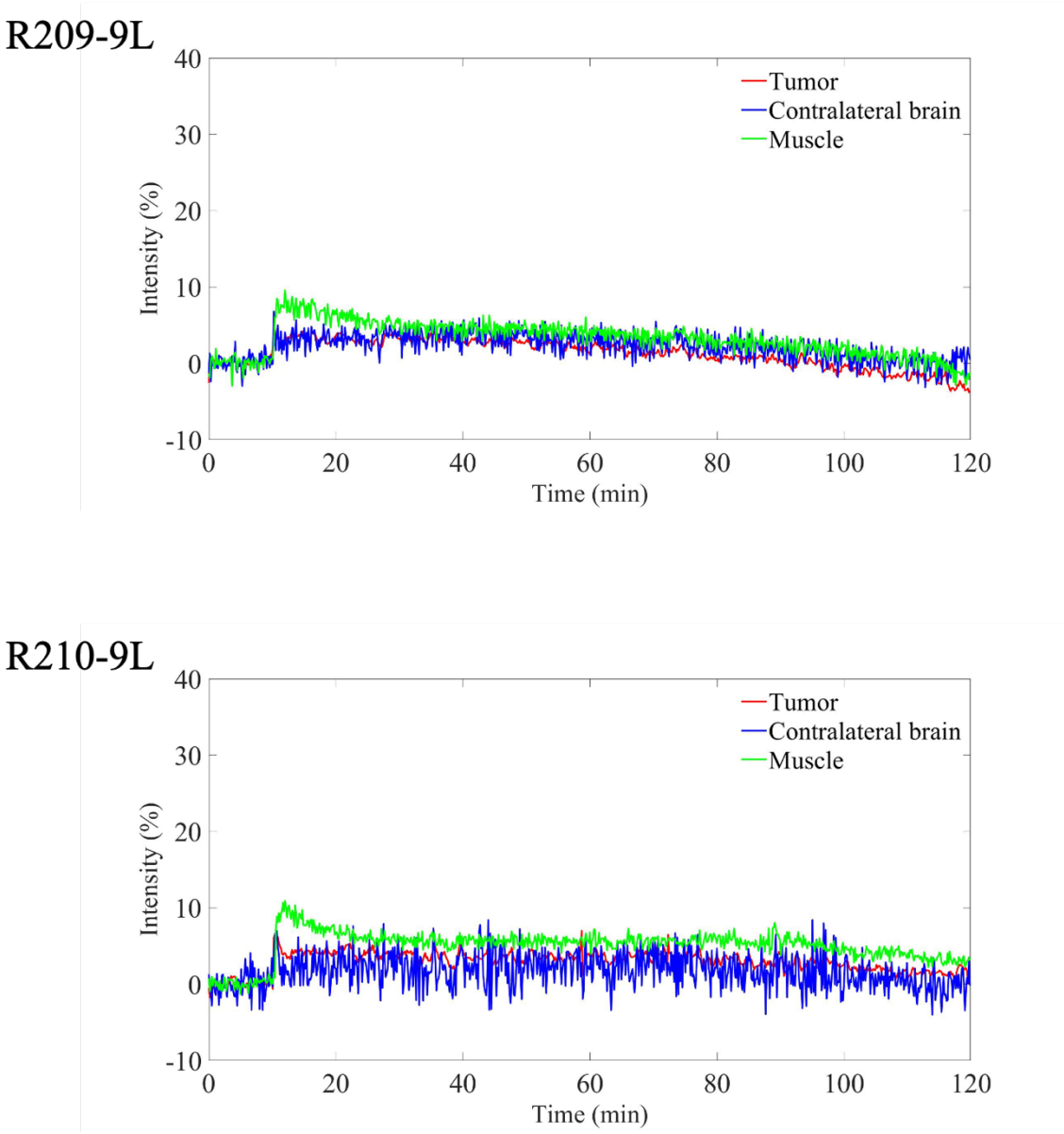

Figure 12. Time course data for the tumor, contralateral brain and muscle region after applying conditional smoothening and drift algorithm for 9L cohort.

R1

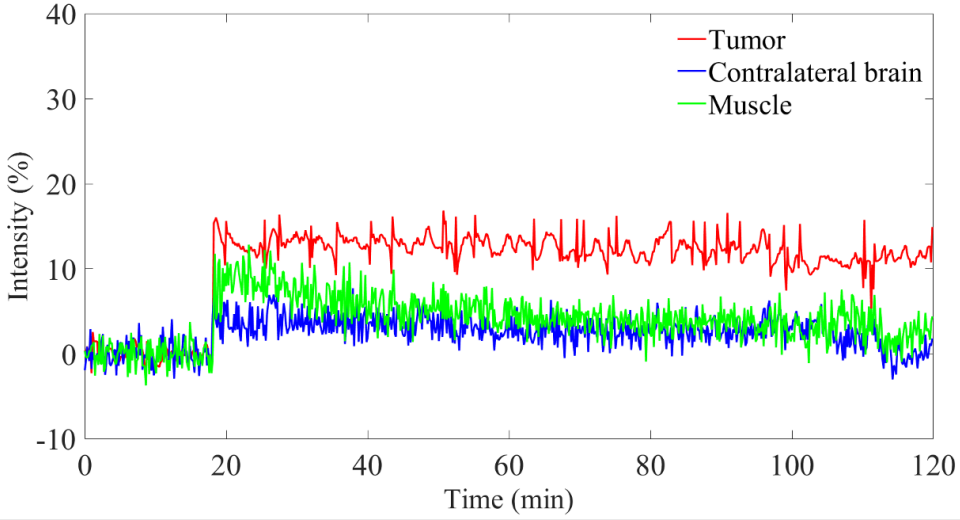
Tumor
Contralateral brain
Muscle
Intensity (%)
Time (min)
40
30
20
10
0
-10
0
20
40
60
80
100
120

R2

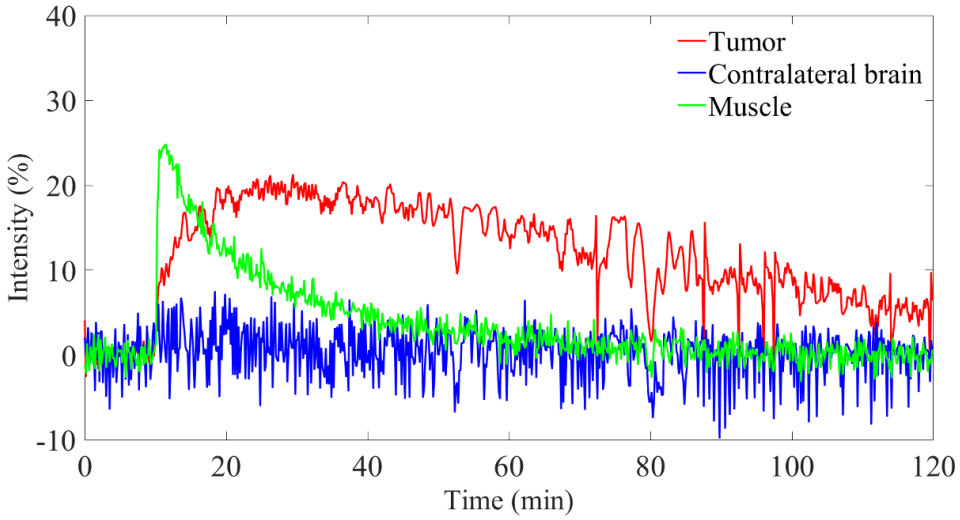
Tumor
Contralateral brain
Muscle
Intensity (%)
Time (min)
40
30
20
10
0
-10
0
20
40
60
80
100
120

R3

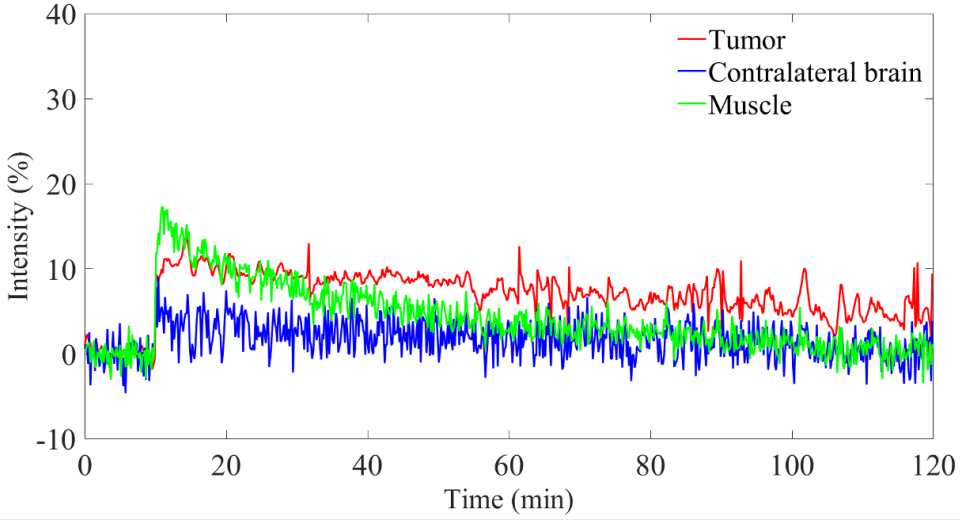
Tumor
Contralateral brain
Muscle
Intensity (%)
Time (min)
40
30
20
10
0
-10
0
20
40
60
80
100
120

R4

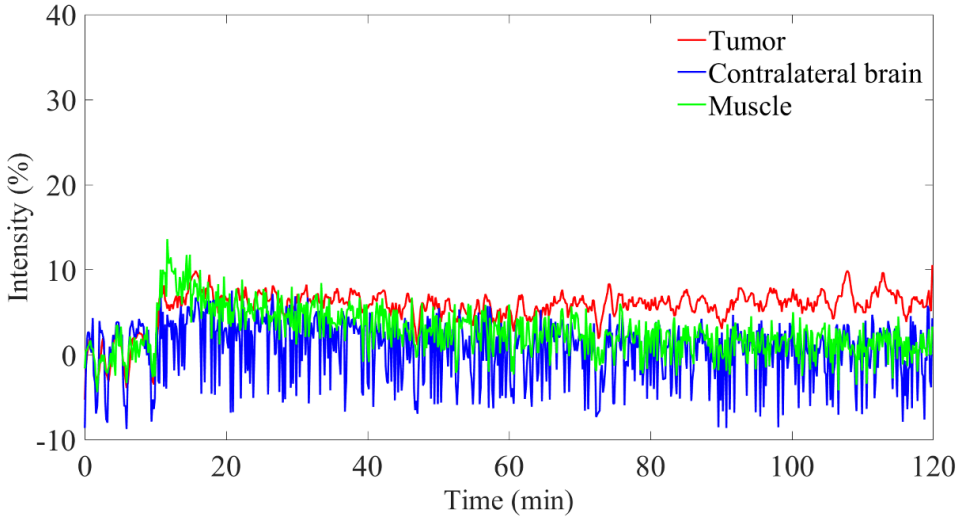
Tumor
Contralateral brain
Muscle
Intensity (%)
Time (min)
40
30
20
10
0
-10
0
20
40
60
80
100
120

R5

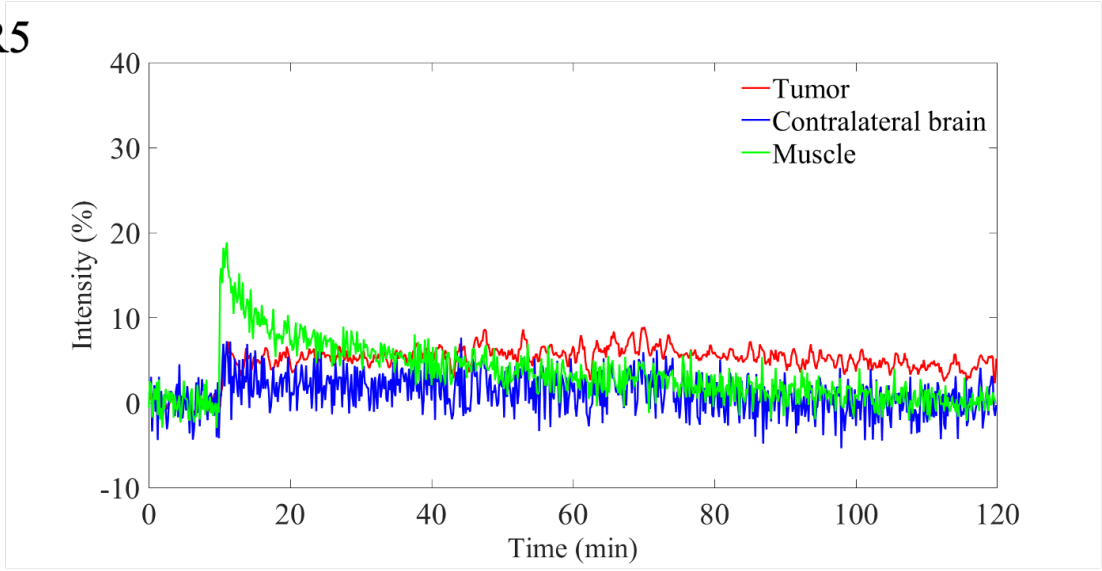
Tumor
Contralateral brain
Muscle
Intensity (%)
Time (min)
40
30
20
10
0
-10
0
20
40
60
80
100
120

R200

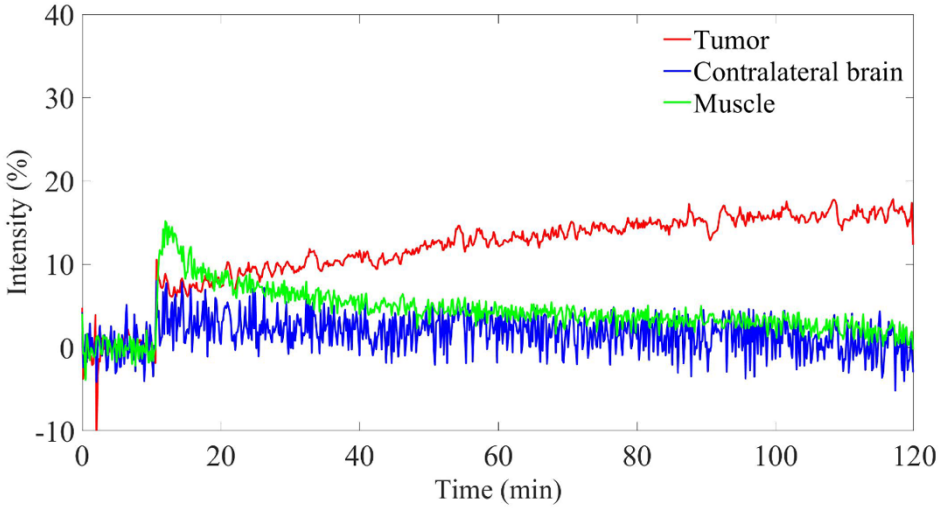
Tumor
Contralateral brain
Muscle
Intensity (%)
Time (min)
40
30
20
10
0
-10
0
20
40
60
80
100
120

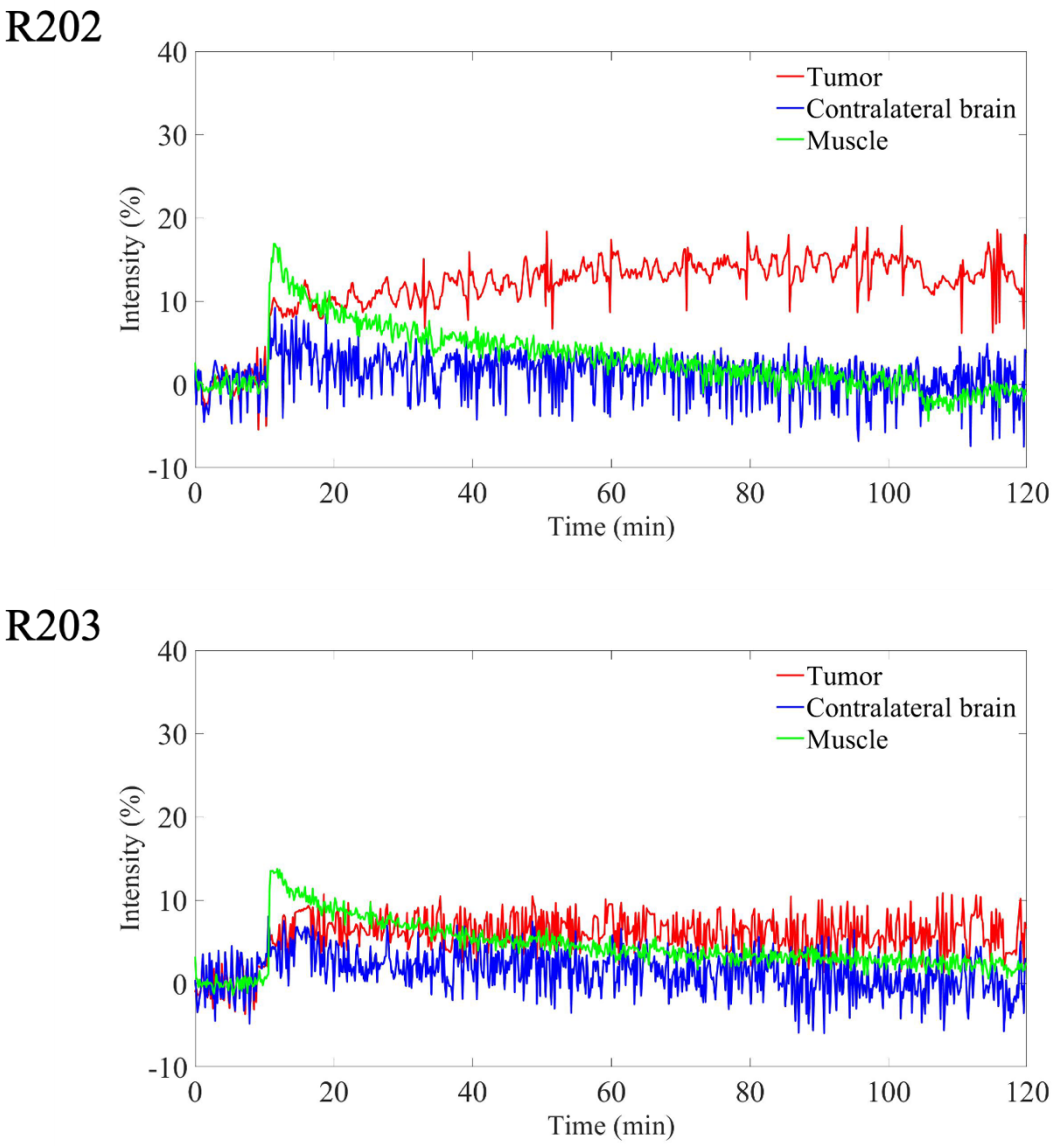

Figure 13. Time course data for the tumor, contralateral brain and muscle region after applying conditional smoothening and drift algorithm for C6 cohort.

Our results indicate the signal enhancements of 0-17% in the tumors using GdDO3NI with clearance from contralateral brain and muscle tissue. To normalize the data with the amount of delivered contrast agent for each animal normalized differential enhancement (NDE) was calculated. The NDE is defined as the difference in percentage enhancement between the tumor region and the contralateral brain and the result is divided by the maximum value of the muscle enhancement for each data set. Table 3 and

Table ***4*** summarize the tumor volume and the NDE value for the respective animal in each cohort.

Table 3. The tumor size and the NDE value of the animals in the 9L cohort.

9L cohort	Volume (mm^3)	NDE
R1	44.75	0.55
R2	3.5	0.07
R5	23.5	0.3
R204	5.5625	-0.16
R206	6.5	-0.22
R208	6.5625	-0.36
R209	14.625	-0.35
R210	4.75	0.1
Mean	13.71±14.21	-0.008±0.323

Table 4. The tumor size and the NDE value of the animals in the C6 cohort.

C6 cohort	Volume (mm^3)	NDE
R1	23.5	1.05
R2	27.25	0.23
R3	41	0.31
R4	35	0.46
R5	11.5	0.28
R200	17.125	0.99
R202	21.375	0.76
R203	27.5	0. 26
Mean	25.53±9.44	0.542±0.340

To study if there was any correlation between tumor size and the NDE value the correlation graphs were generated as Figure 14 and Figure 15. There was no correlation between the tumor size and NDE as the r^2 value for the linear equation was r^2=0.11; however, the 9L cohort showed a good correlation between the tumor size and the NDE value. Considering all the values of NDE the r^2 resulted in r^2=0.53 and with positive NDE values the r^2 was 0.99.

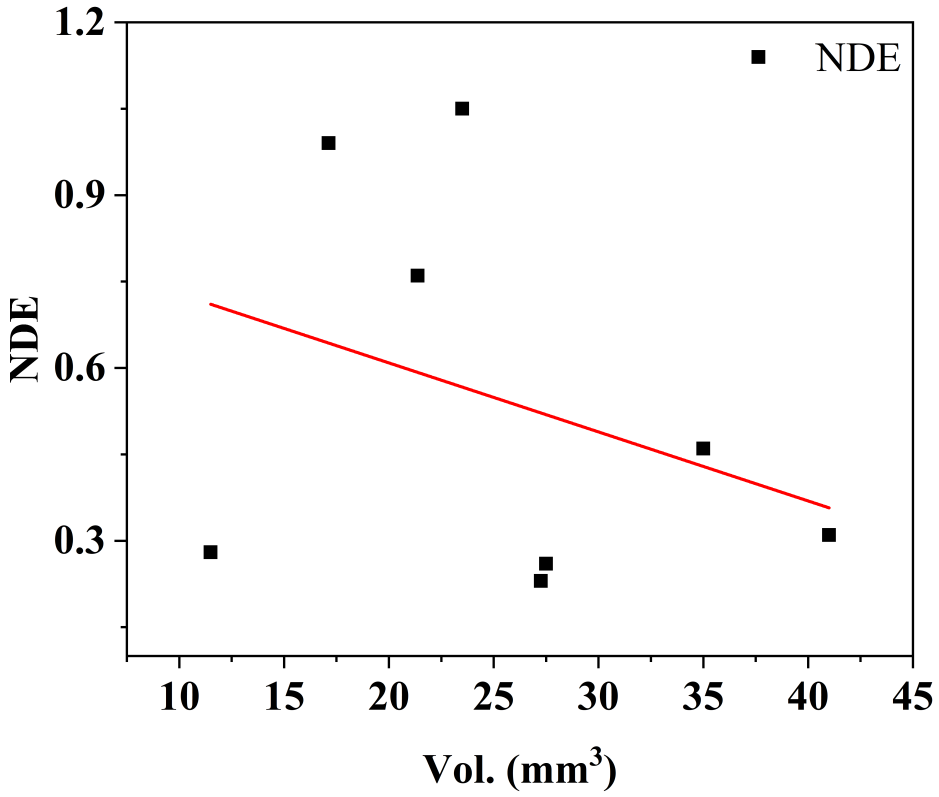

Figure 14. Correlation between NDE and tumor volume in the C6 cohort. The equation of fit curve and the r^2 representing the line is $\boldsymbol{NDE = -0.011 \times Vol. + 0.843}$ *and* r^2*=0.11.*

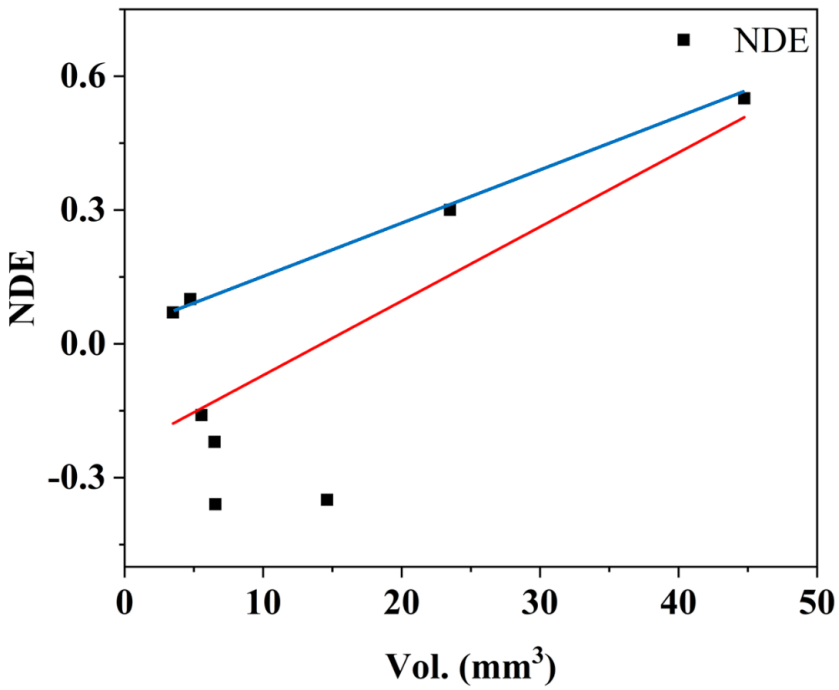

Figure 15 Correlation between NDE and tumor volume in the 9L cohort. The equation of the fitted curve and the r^2 of the red line, which shows the correlation between all the data points and tumor volume is $\boldsymbol{NDE = 0.016 \times Vol. - 0.237}$ *and* r^2*=0.53 and the blue line, which shows the correlation between all the positive NDE values and tumor volume is* $\boldsymbol{NDE = 0.011 \times Vol. + 0.036}$ *and* r^2*=0.99.*

Pharmacokinetic modeling of the data will allow us to characterize the tumor microenvironment quantitatively and enable simultaneous assessment of perfusion and hypoxia parameters in tumors. To study the pharmacokinetics of the tissue in DCE computing concentration maps is the crucial beginning step. To this end, the T_1 map of the brain is calculated to obtain the relaxation rates before the injection of the contrast agent. Later using the pre-injection R_1 values and the time dependent relaxation during injection and clearance the concentration maps were calculated. The T_1 maps of the animals are represented in *Figure **16*** for 9L cohort and *Figure **17*** for C6 cohort.

Animal# 1

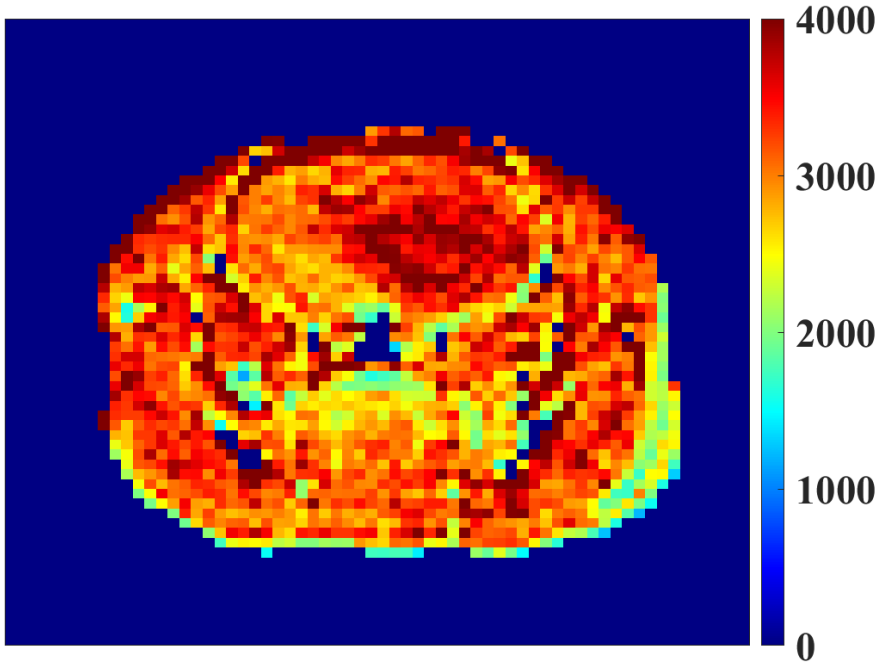

Animal# 2

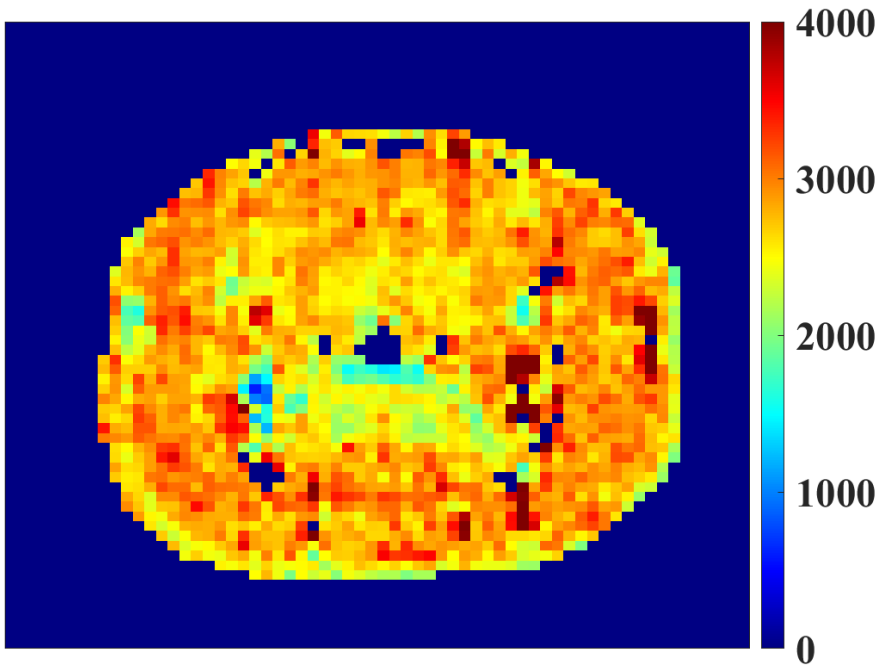

Animal# 3

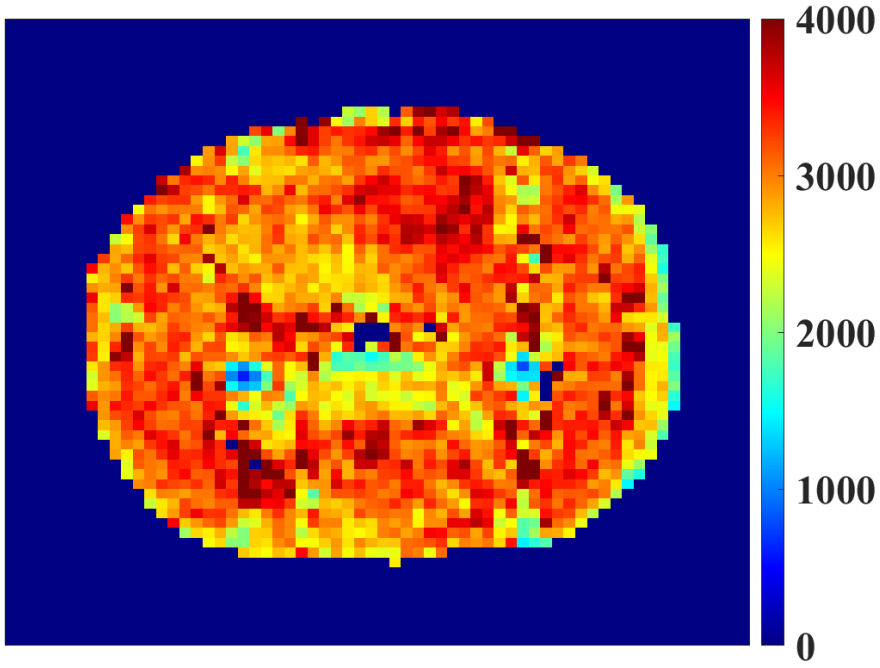

Animal# 4

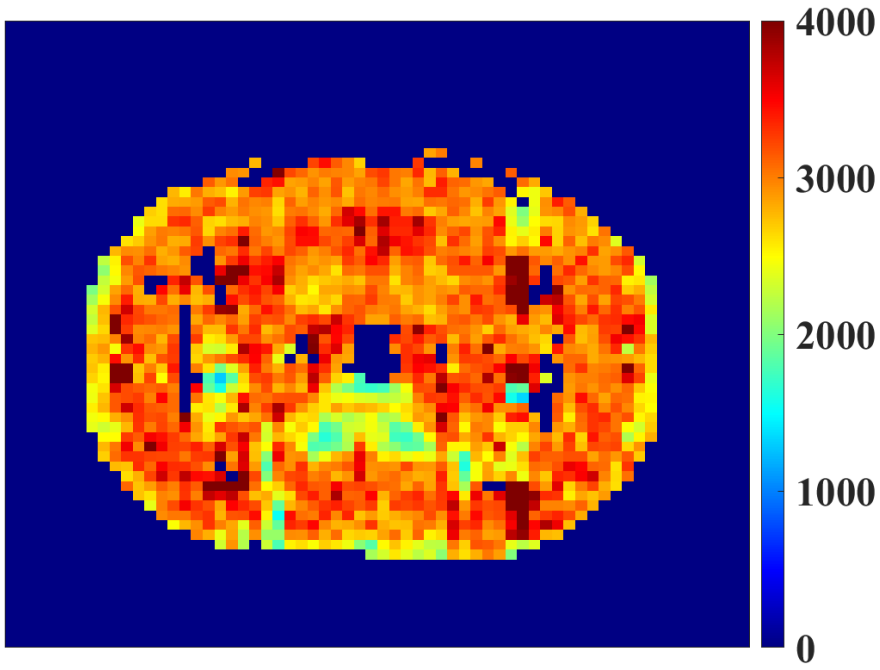

Animal# 5

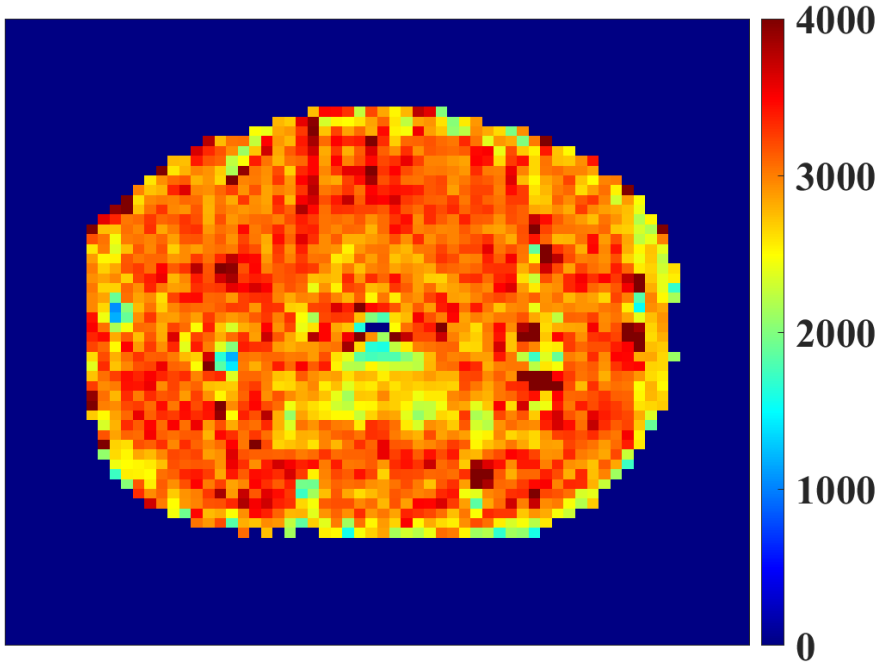

Animal# 6

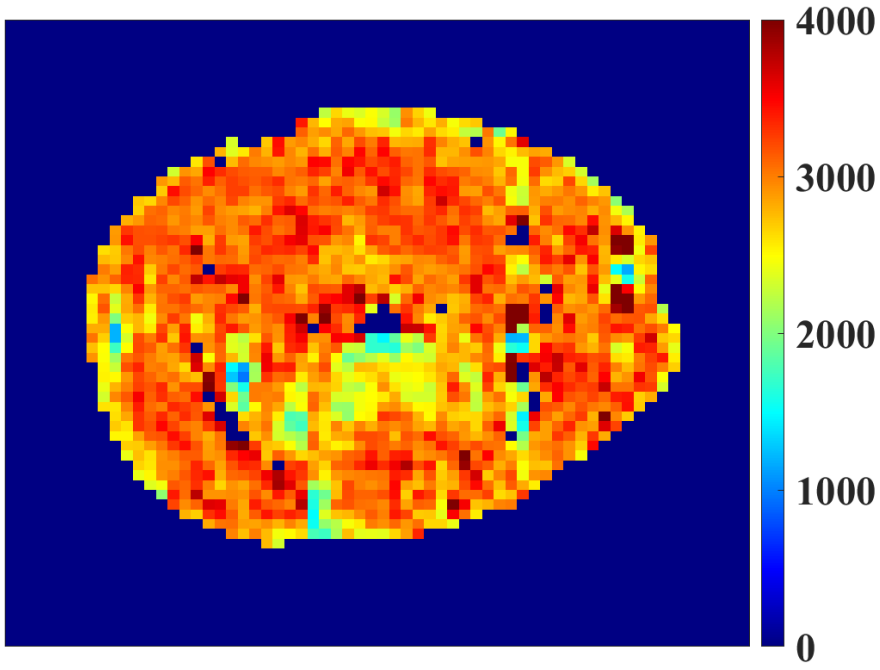

Animal# 7

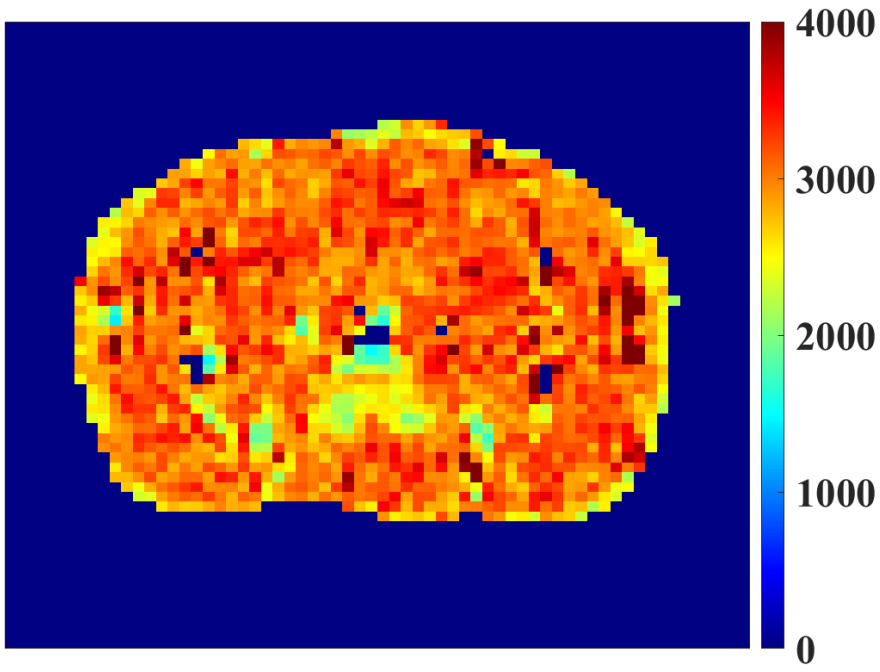

Animal# 8

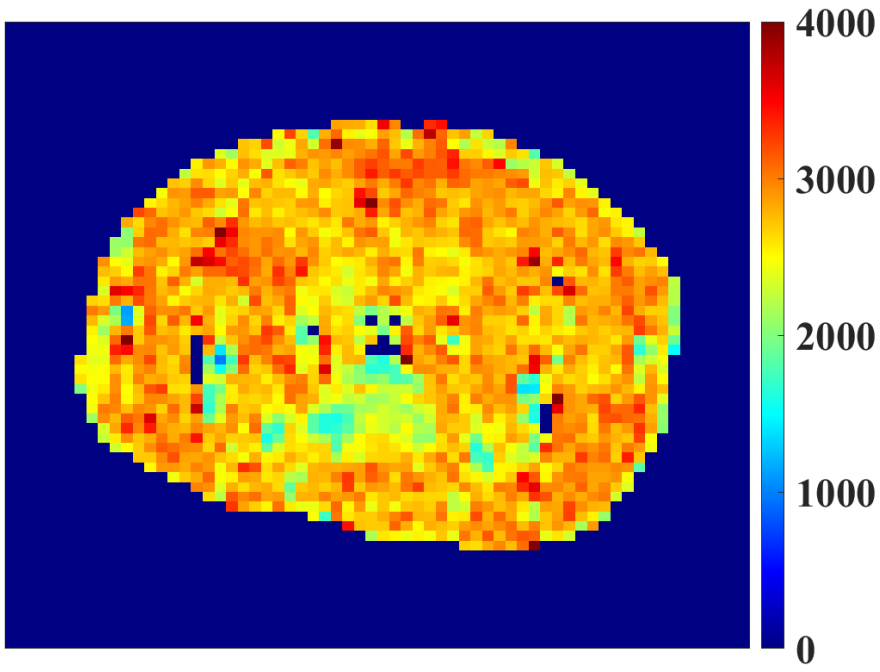

Figure 16. T_1 map of the animals before injection in 9L cohort the color bar is represented in ms units.

Animal# 1

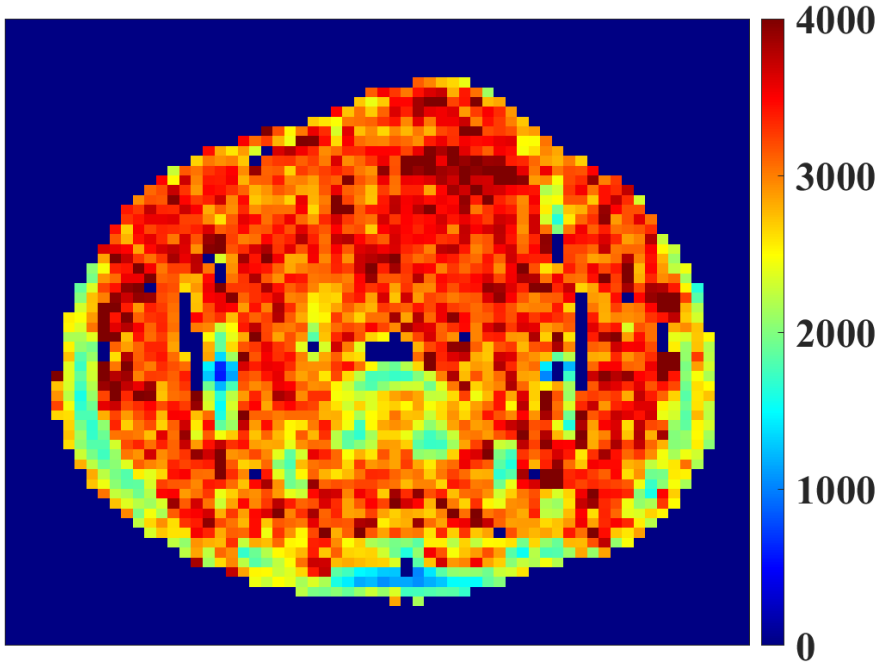

Animal# 2

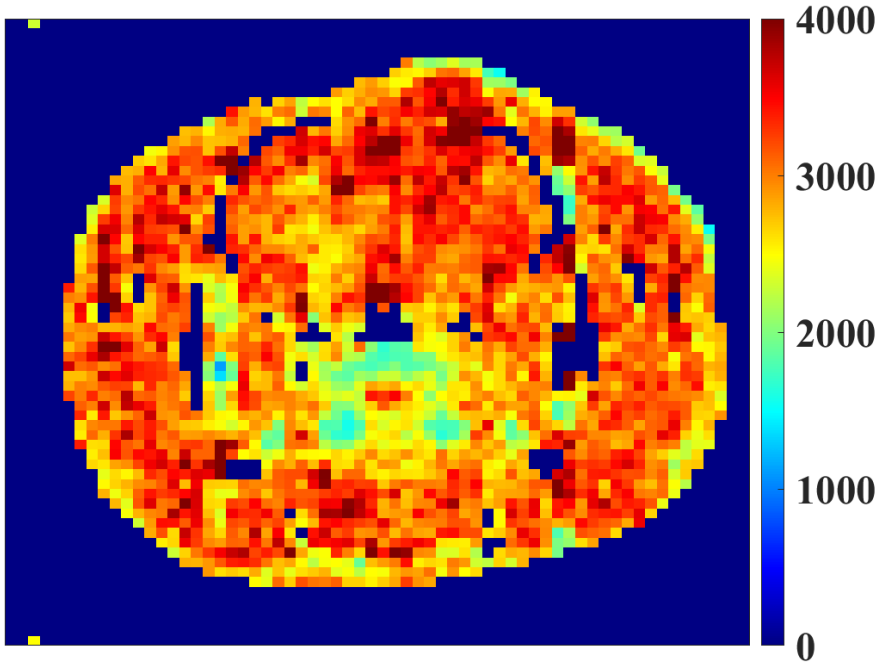

Animal# 3

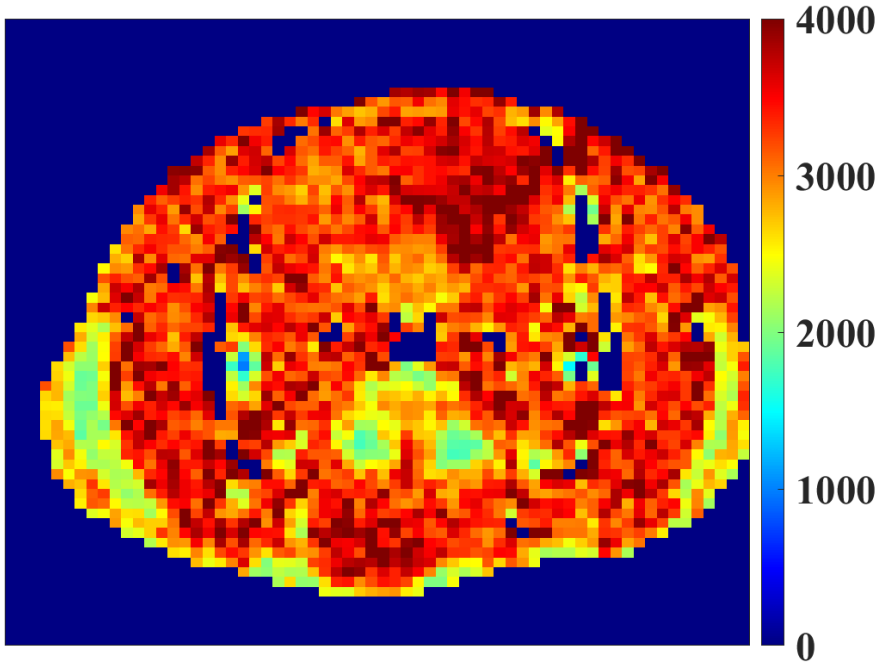

Animal# 4

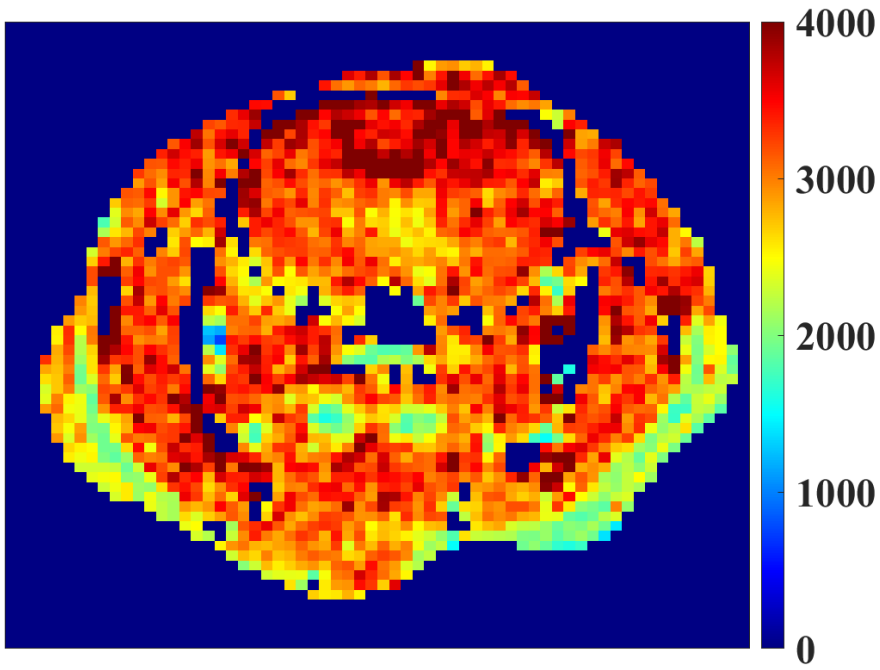

Animal# 5

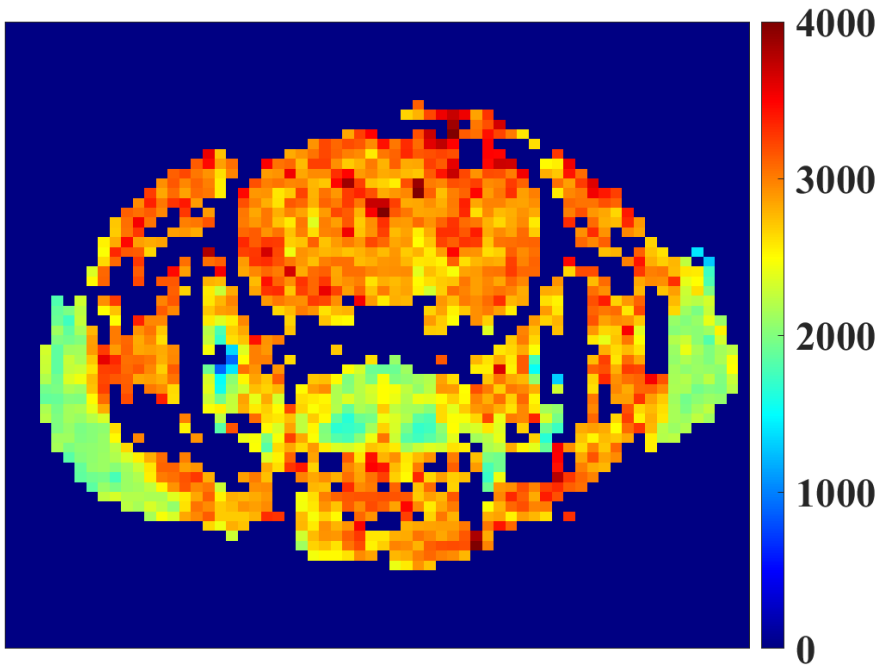

Animal# 6

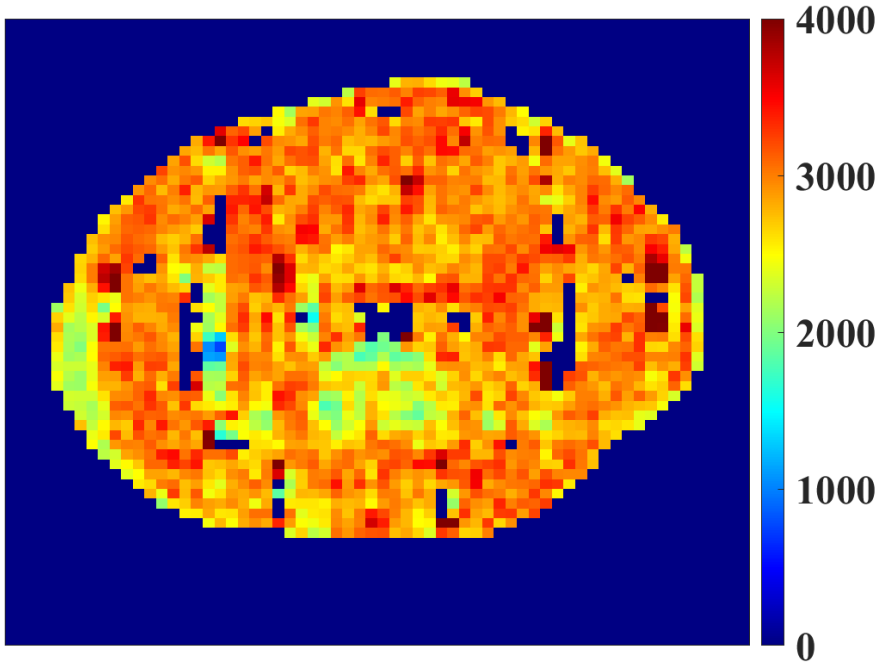

Animal# 7

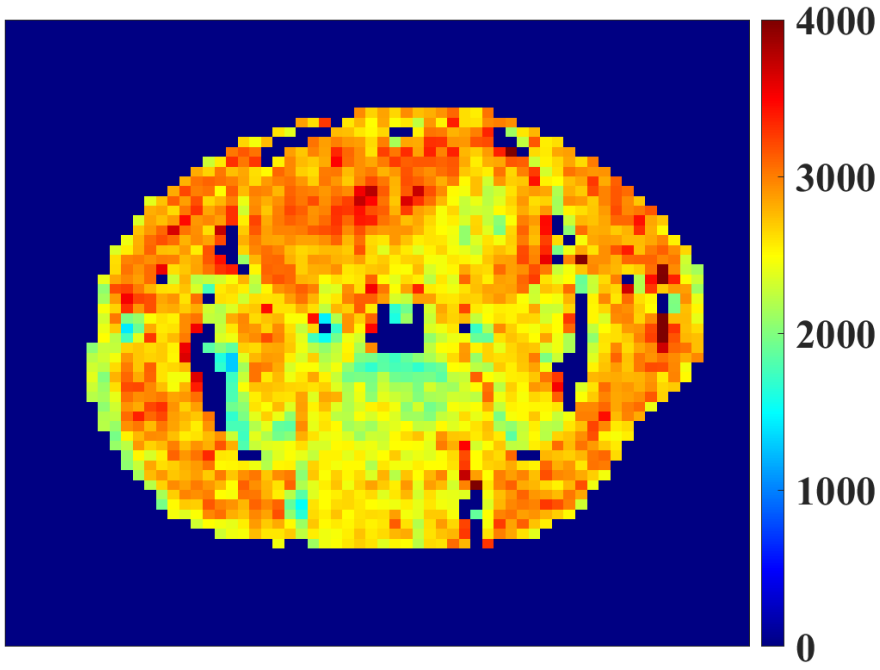

Animal# 8

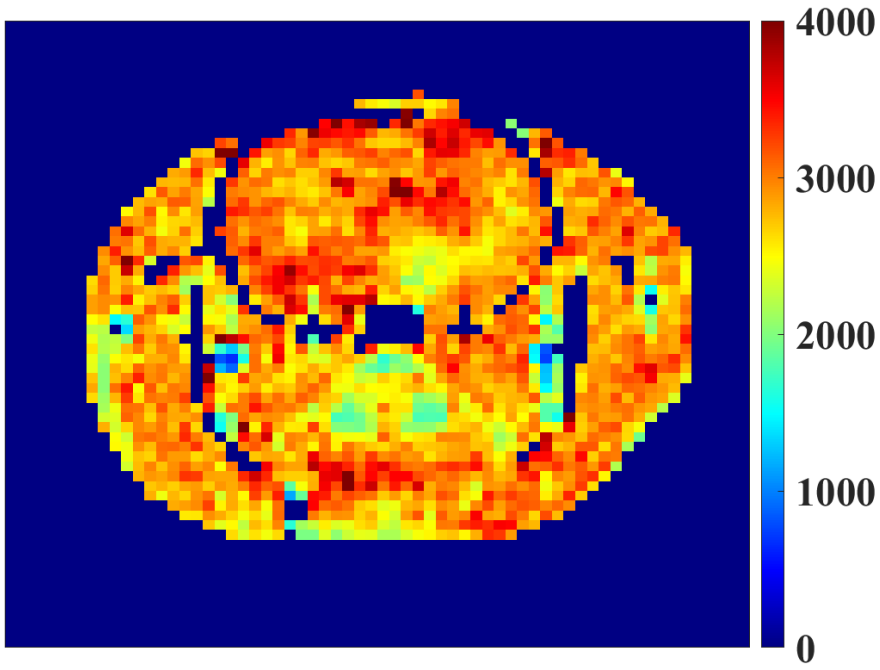

Figure 17. T_1 map of the animals before injection in C6 cohort the color bar is represented in ms units.

*Figure **18*** shows the pre-injection T_1 map and the time course changes in relaxation and concentration values in the tumor, contralateral and muscle region.

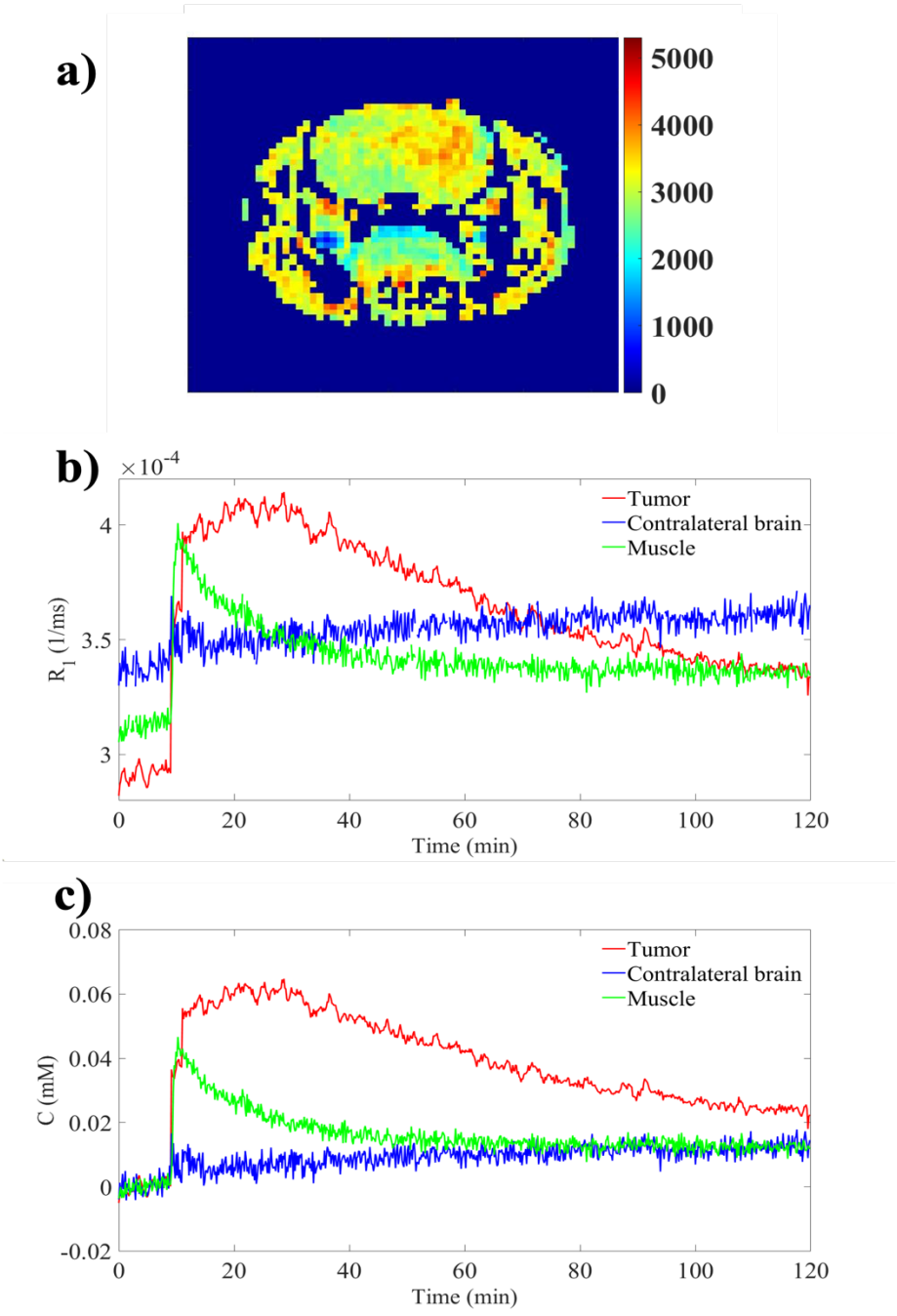

Figure 18. T_1 map of the brain (a) and ROI analysis for tumor, contralateral brain and muscle region on R_1 (b) and concentration map respectively (c).

Figure 19 shows the map of computed pharmacokinetic parameters including K^{trans}, K_2, and v_p values. Figure 20 summarizes the computed concentration map from the DCE-MR images and the reconstructed concentration map from the calculated pharmacokinetic parameters and the difference map. The difference image is the subtraction of the concentration map from the reconstructed concentration map using calculated pharmacokinetic parameters for one of the giant tumors. As Figure 19 shows the tumor region has higher K^{trans} values than the contralateral brain and lower than muscle. The K_2 values in the tumor region are very small. The K_2 values in pixels representing the highest intensity (i.e. higher retention of the contrast agent) are showing the smallest values. The blood volume fraction map shows small values, mostly zeros in the muscle region, which is in good agreement with other reports. The blood volume fraction value for muscle tissue is usually neglected because it is approximately 1-2%[125]. The reconstructed image for concentration using the pharmacokinetic parameters is very similar to the concentration map and shows how closely these two match. The difference map represents the goodness of the fit and the accuracy of the modeled parameters.

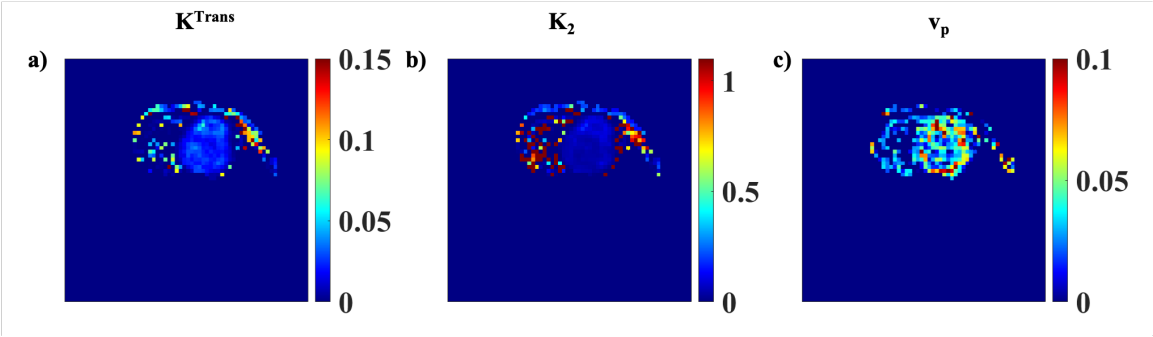

Figure 19. The pharmacokinetic parameters representing a) K^{trans}, b) K_2 and c) v_p.

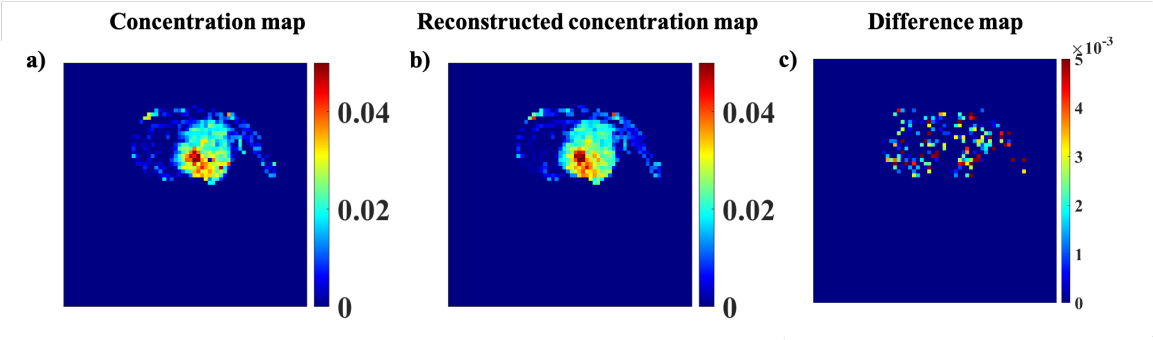

Figure 20. The computed concentration map from the MR data (a), the reconstructed concentration map using pharmacokinetic parameters (b) and the difference map (c).

The calculated parameter maps and reconstructed concentration maps for each animal are represented in Figure 21 and Figure 22 respectively for 9L and C6 cohorts. The mean value and standard deviation of the parameters (K_1, K_2 and v_p) for tumor, contralateral brain and muscle ROI are tabulated in *Table 5* through *Table 16* for 1h and 2h timepoint. The visualization of the concentration maps shows distinct hyperintense regions in the tumor regions especially in the big tumors; however, the mean values of pharmacokinetic parameters over the tumor ROI s do significantly differ between the two cohorts at either 1h or 2h timepoints. The images of reconstructed concentration maps and directly calculated concentration maps are in good agreement for the two cohorts.

Animal# 1

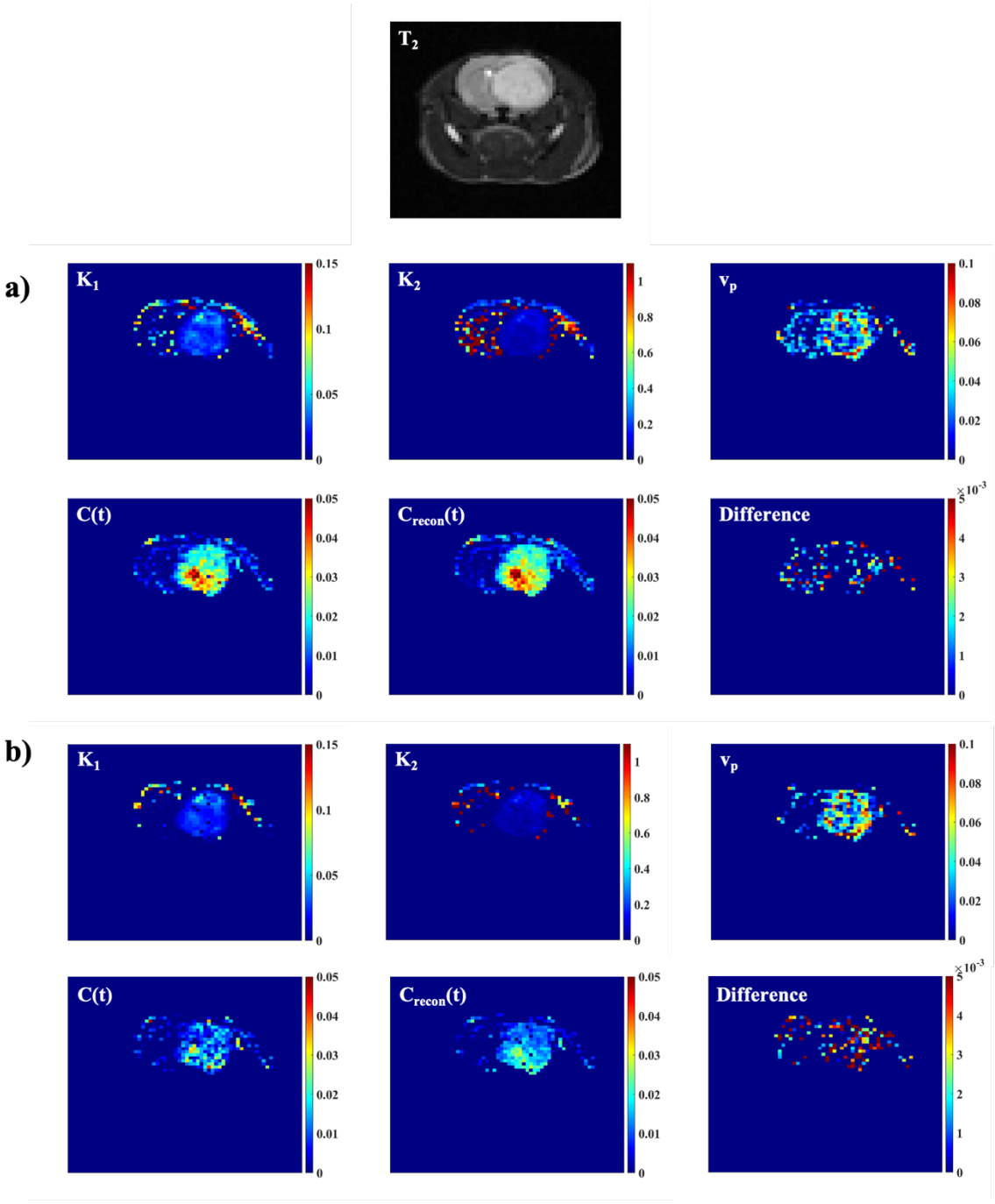
T2
a)
K1
K2
vp
C(t)
Crecon(t)
Difference
b)
K1
K2
vp
C(t)
Crecon(t)
Difference

Animal# 2

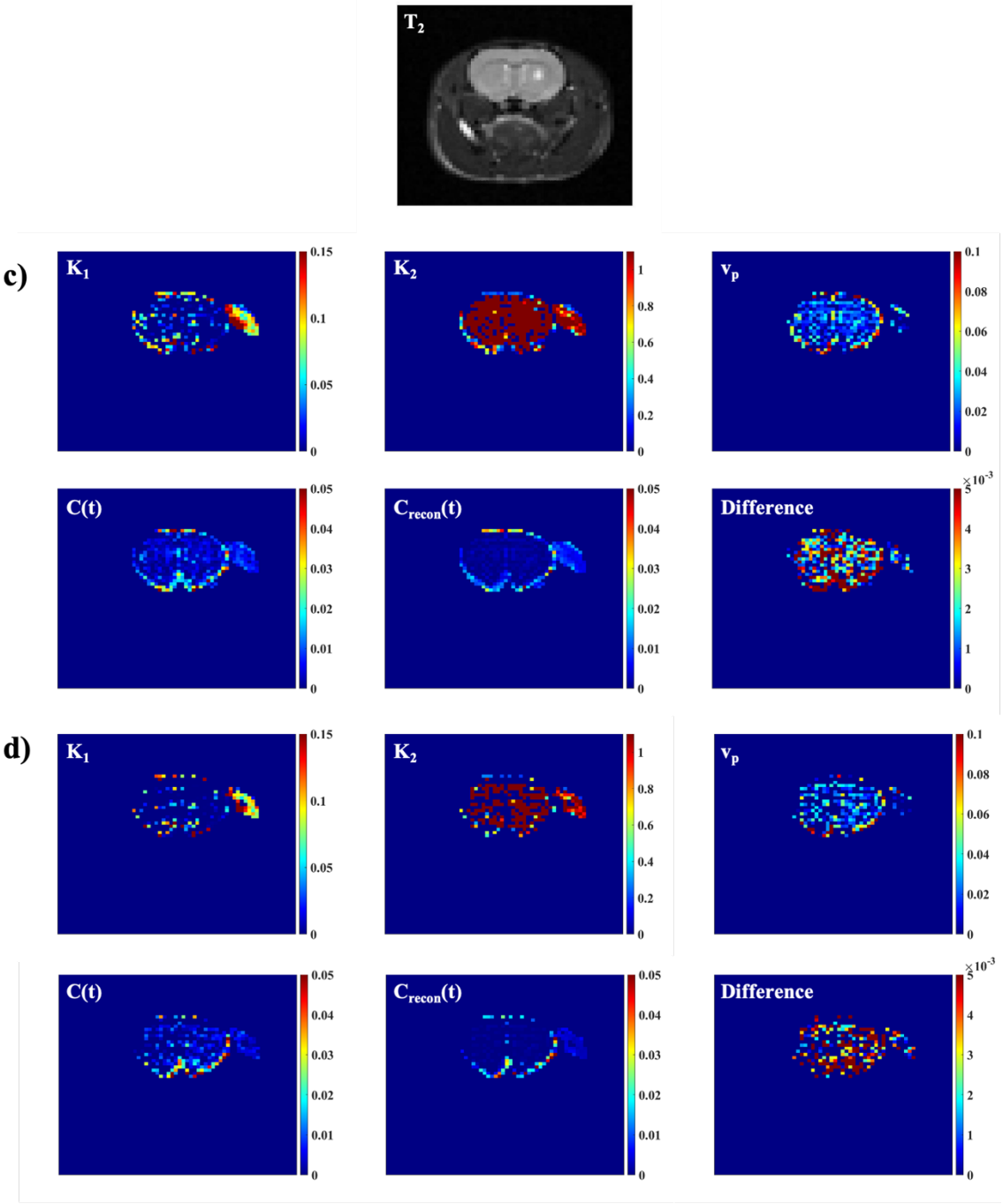
T2
c)
K1
0.15
0.1
0.05
0
K2
1
0.8
0.6
0.4
0.2
0
vp
0.1
0.08
0.06
0.04
0.02
0
C(t)
0.05
0.04
0.03
0.02
0.01
0
Crecon(t)
0.05
0.04
0.03
0.02
0.01
0
Difference
×10-3
5
4
3
2
1
0
d)
K1
0.15
0.1
0.05
0
K2
1
0.8
0.6
0.4
0.2
0
vp
0.1
0.08
0.06
0.04
0.02
0
C(t)
0.05
0.04
0.03
0.02
0.01
0
Crecon(t)
0.05
0.04
0.03
0.02
0.01
0
Difference
×10-3
5
4
3
2
1
0

Animal# 3

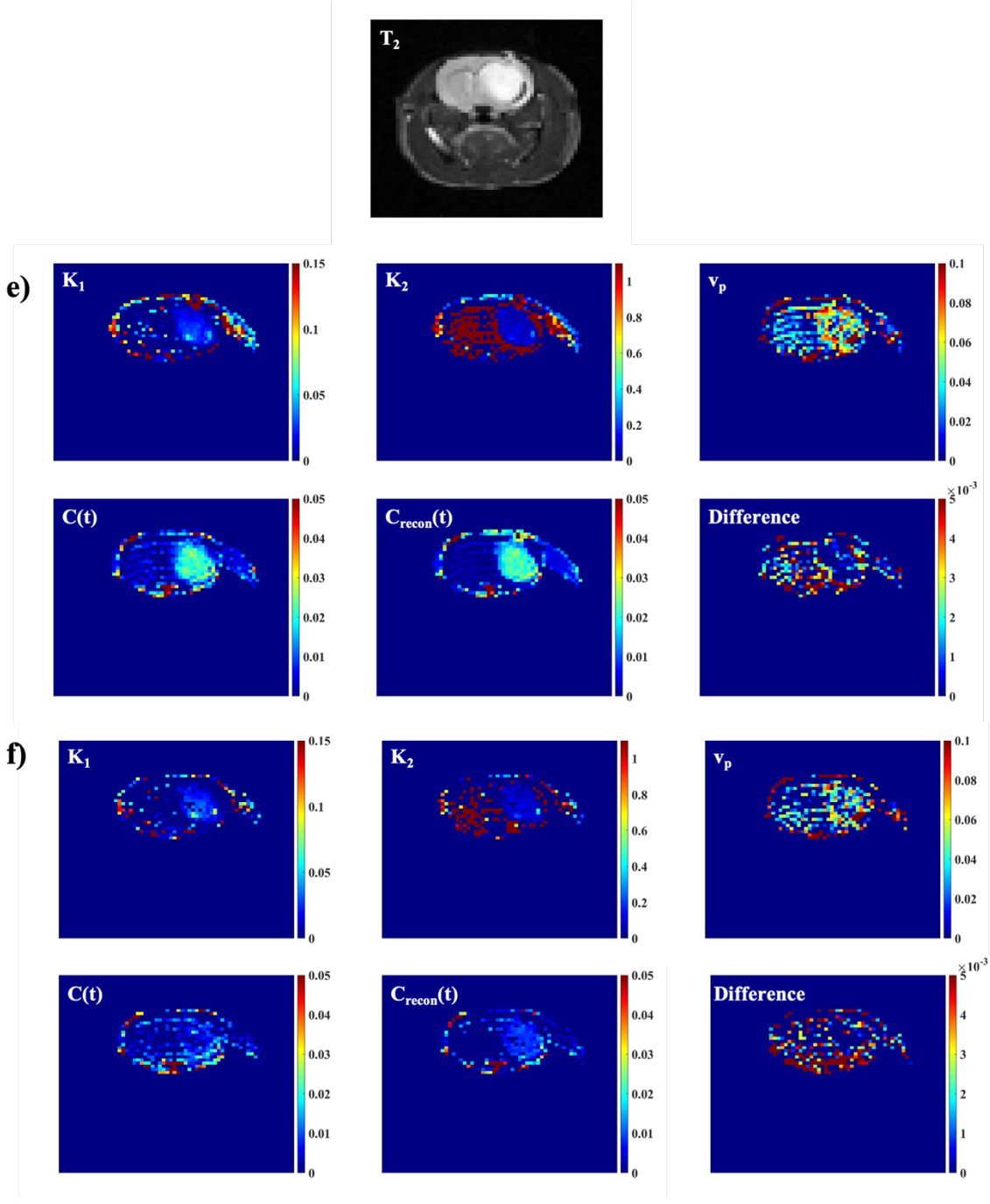
T2
e)
K1
K2
vp
C(t)
Crecon(t)
Difference
f)
K1
K2
vp
C(t)
Crecon(t)
Difference

Animal# 4

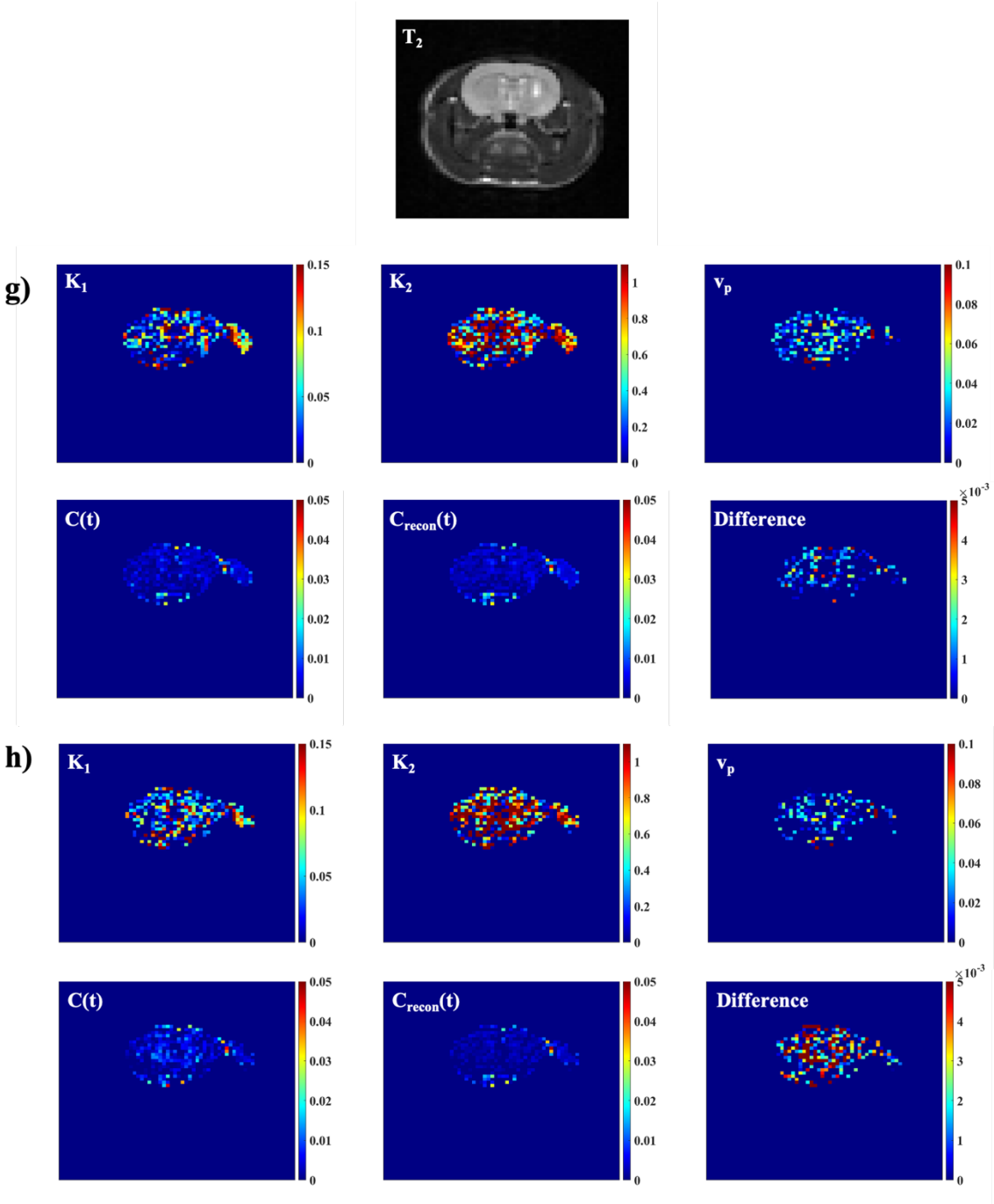
T2
g)
K1
K2
vp
C(t)
Crecon(t)
Difference
h)
K1
K2
vp
C(t)
Crecon(t)
Difference

Animal# 5

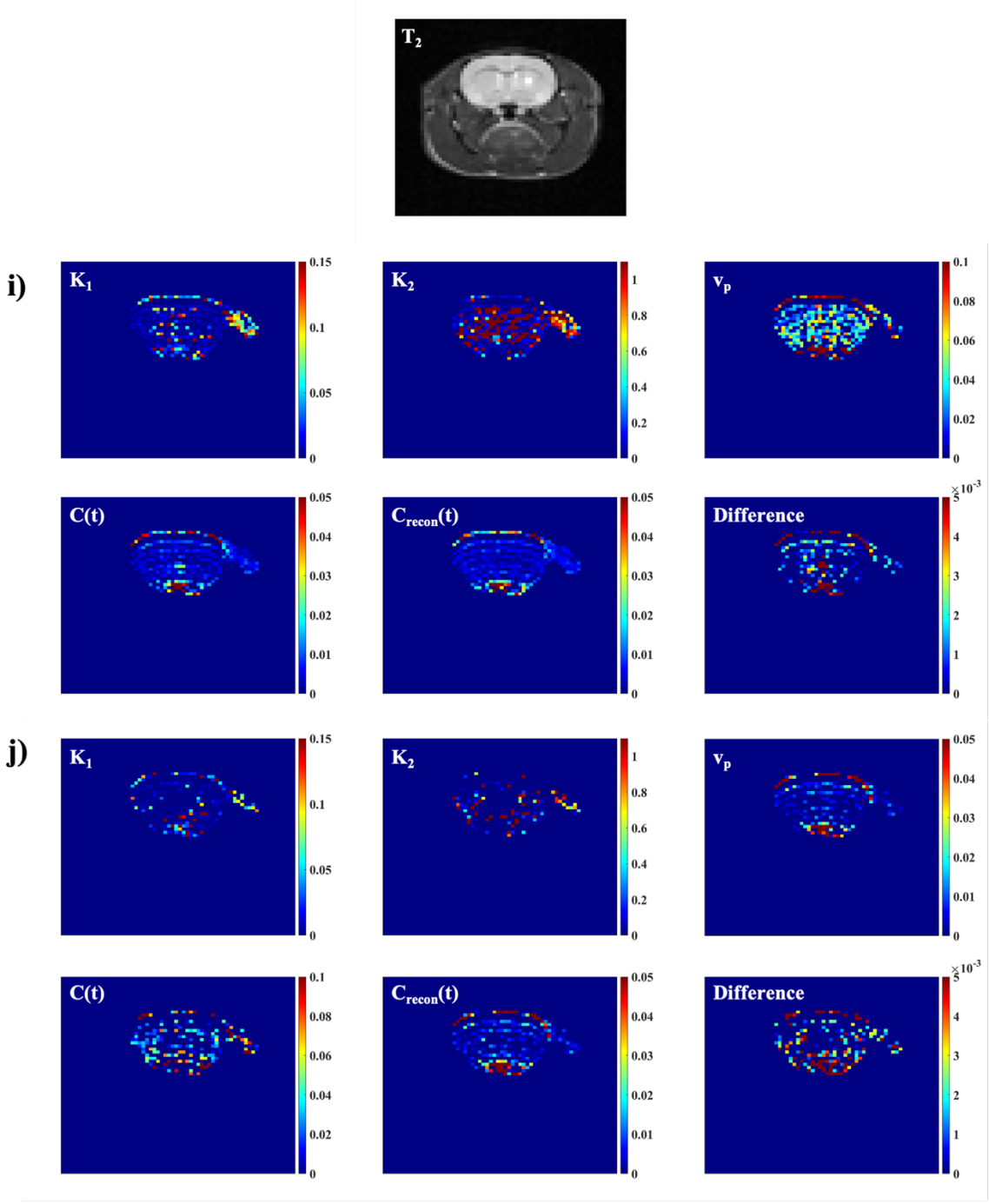
T2
i)
K1
K2
vp
C(t)
Crecon(t)
Difference
j)
K1
K2
vp
C(t)
Crecon(t)
Difference

Animal# 6

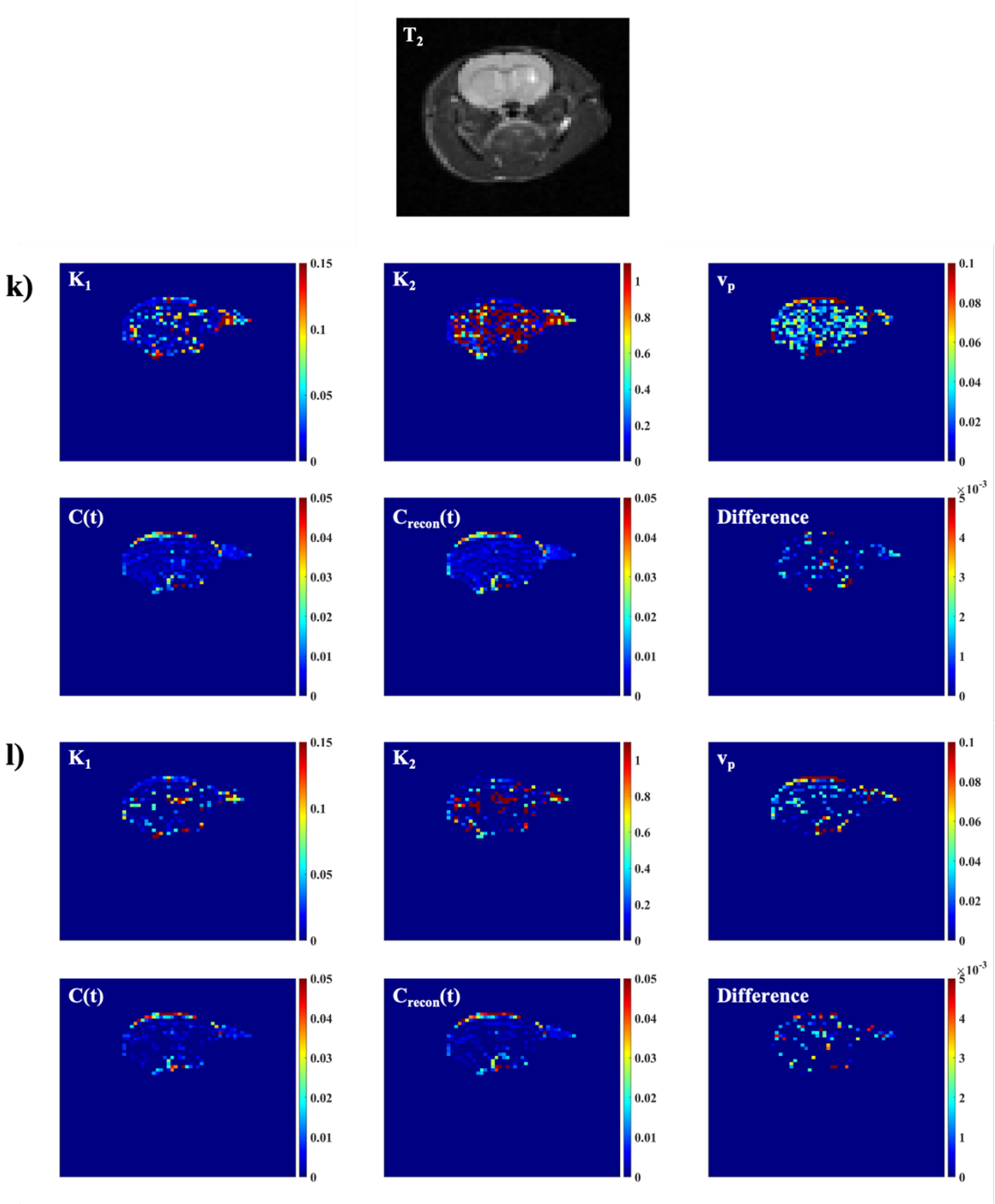
T2
k)
K1
K2
vp
C(t)
Crecon(t)
Difference
l)
K1
K2
vp
C(t)
Crecon(t)
Difference

Animal# 7

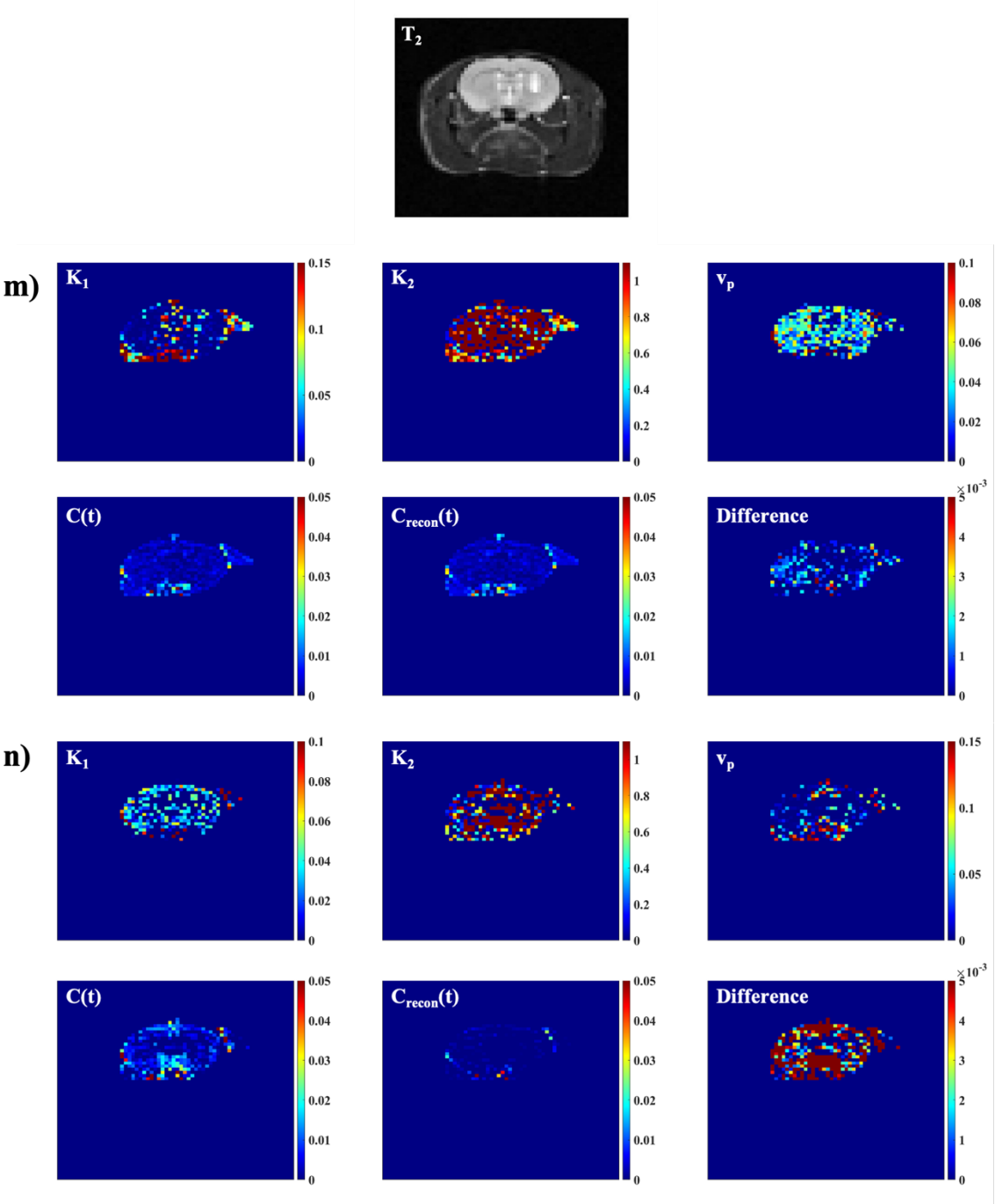
T2
m)
K1
K2
vp
C(t)
Crecon(t)
Difference
n)
K1
K2
vp
C(t)
Crecon(t)
Difference

Animal# 8

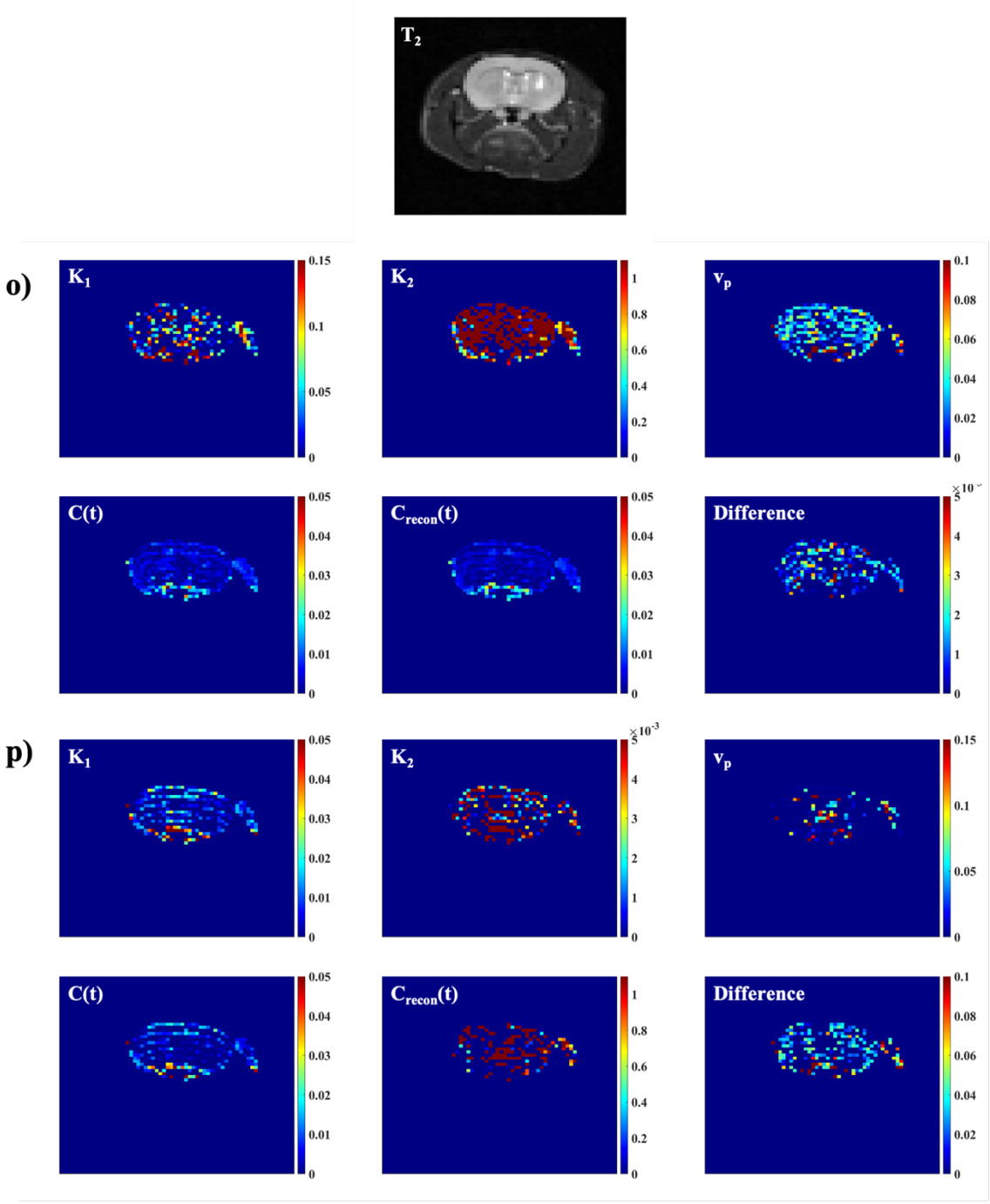

Figure 21 The T_2 weighted anatomical image and the pharmacokinetic maps and concentration maps of the individual animals in 9L cohort over 1h post-injection in a, c, e, g, i, k, m, o and 2h post-injection in b, d, f, h, j, l, n, p.

Animal# 1

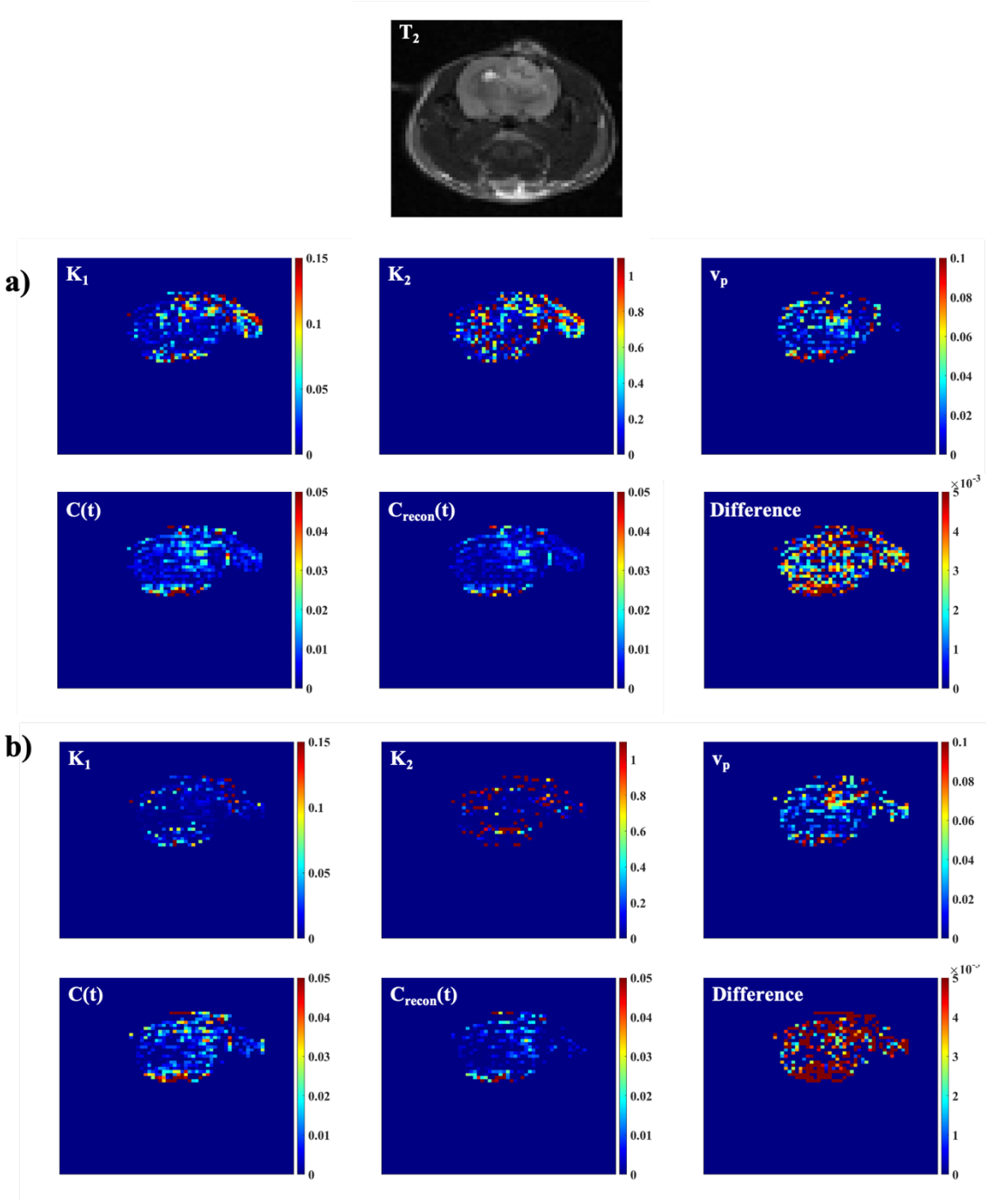
T2
a)
K1
K2
vp
C(t)
Crecon(t)
Difference
b)
K1
K2
vp
C(t)
Crecon(t)
Difference

Animal# 2

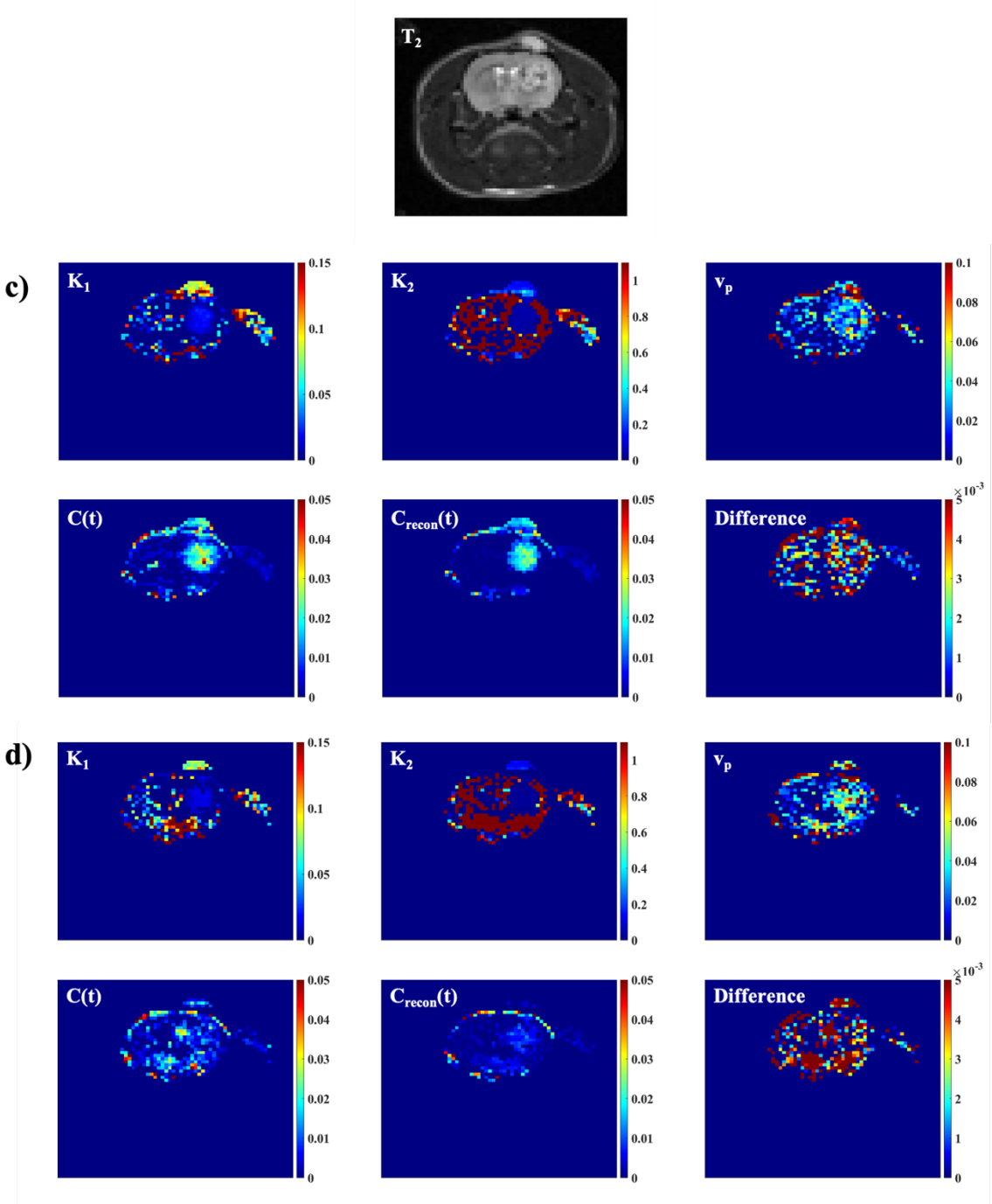
T2
c)
K1
K2
vp
C(t)
Crecon(t)
Difference
d)
K1
K2
vp
C(t)
Crecon(t)
Difference

Animal# 3

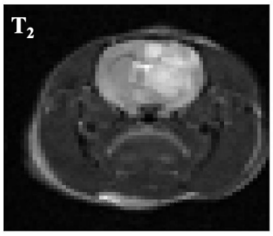
T2

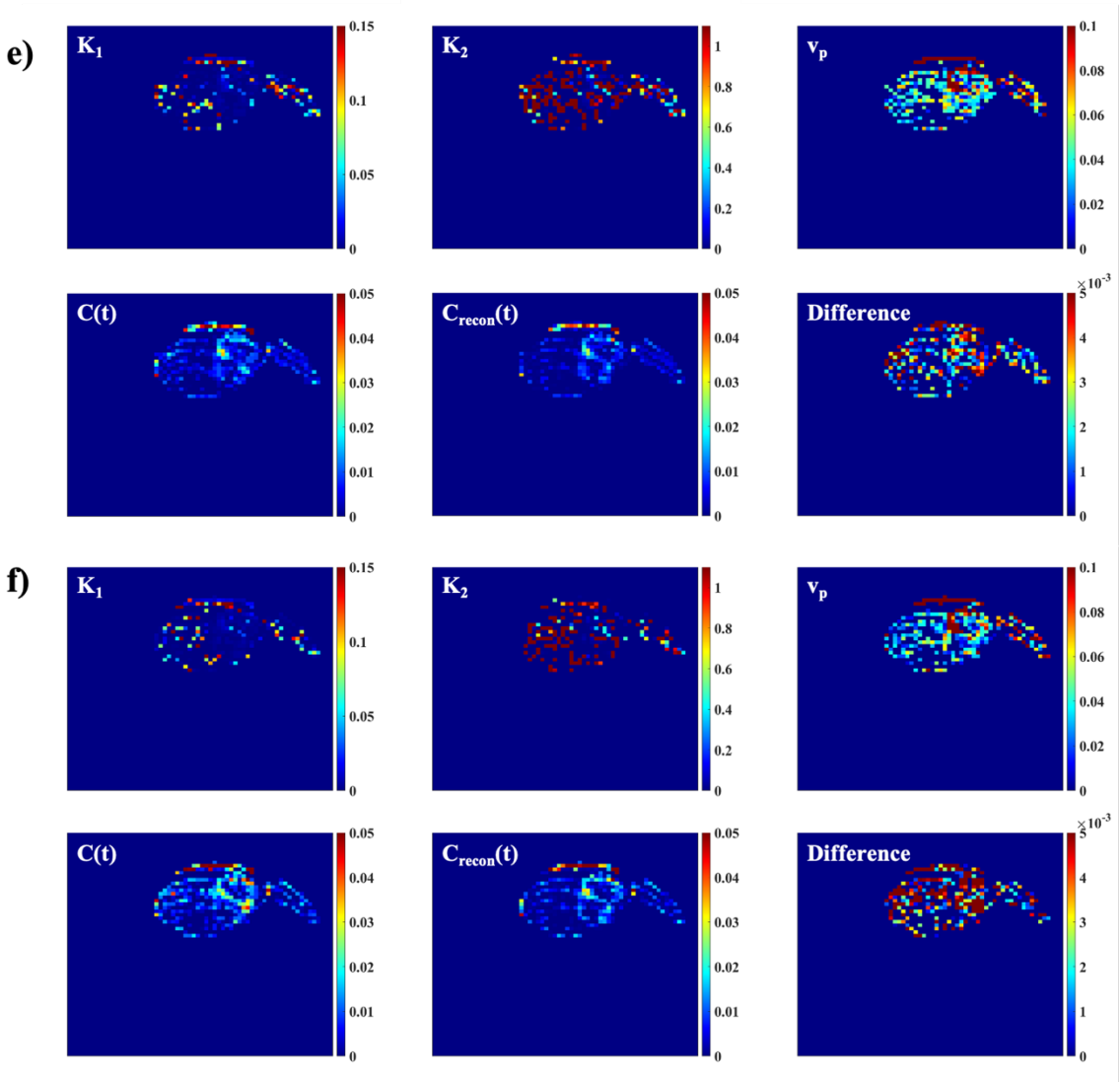
e)
K1
0.15
0.1
0.05
0
K2
1
0.8
0.6
0.4
0.2
0
vp
0.1
0.08
0.06
0.04
0.02
0
C(t)
0.05
0.04
0.03
0.02
0.01
0
Crecon(t)
0.05
0.04
0.03
0.02
0.01
0
Difference
×10-3
5
4
3
2
1
0
f)
K1
0.15
0.1
0.05
0
K2
1
0.8
0.6
0.4
0.2
0
vp
0.1
0.08
0.06
0.04
0.02
0
C(t)
0.05
0.04
0.03
0.02
0.01
0
Crecon(t)
0.05
0.04
0.03
0.02
0.01
0
Difference
×10-3
5
4
3
2
1
0

Animal# 4

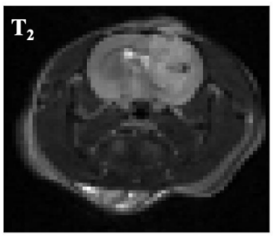
T2

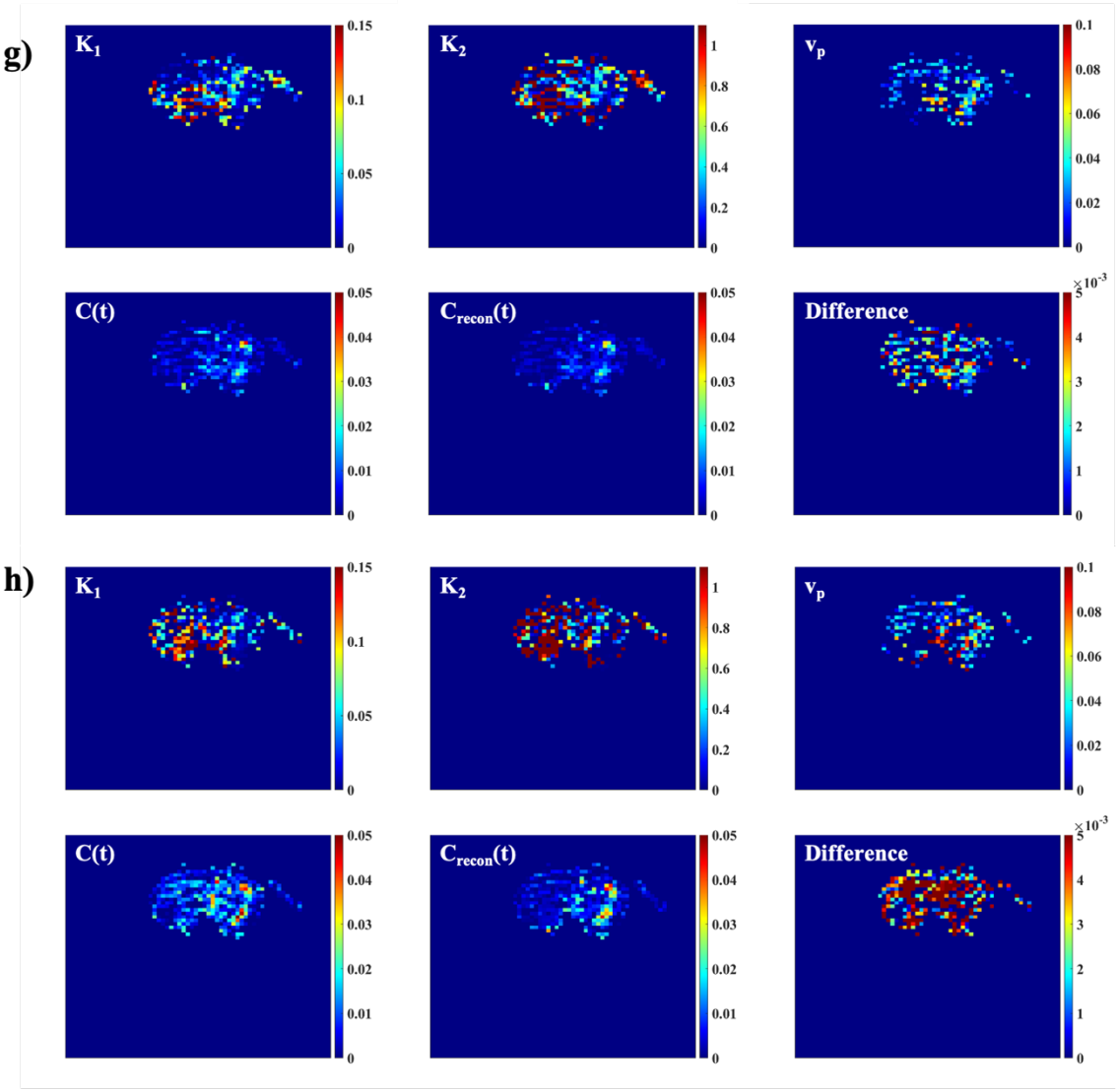
g)
K1
K2
vp
C(t)
Crecon(t)
Difference
h)
K1
K2
vp
C(t)
Crecon(t)
Difference

Animal# 5

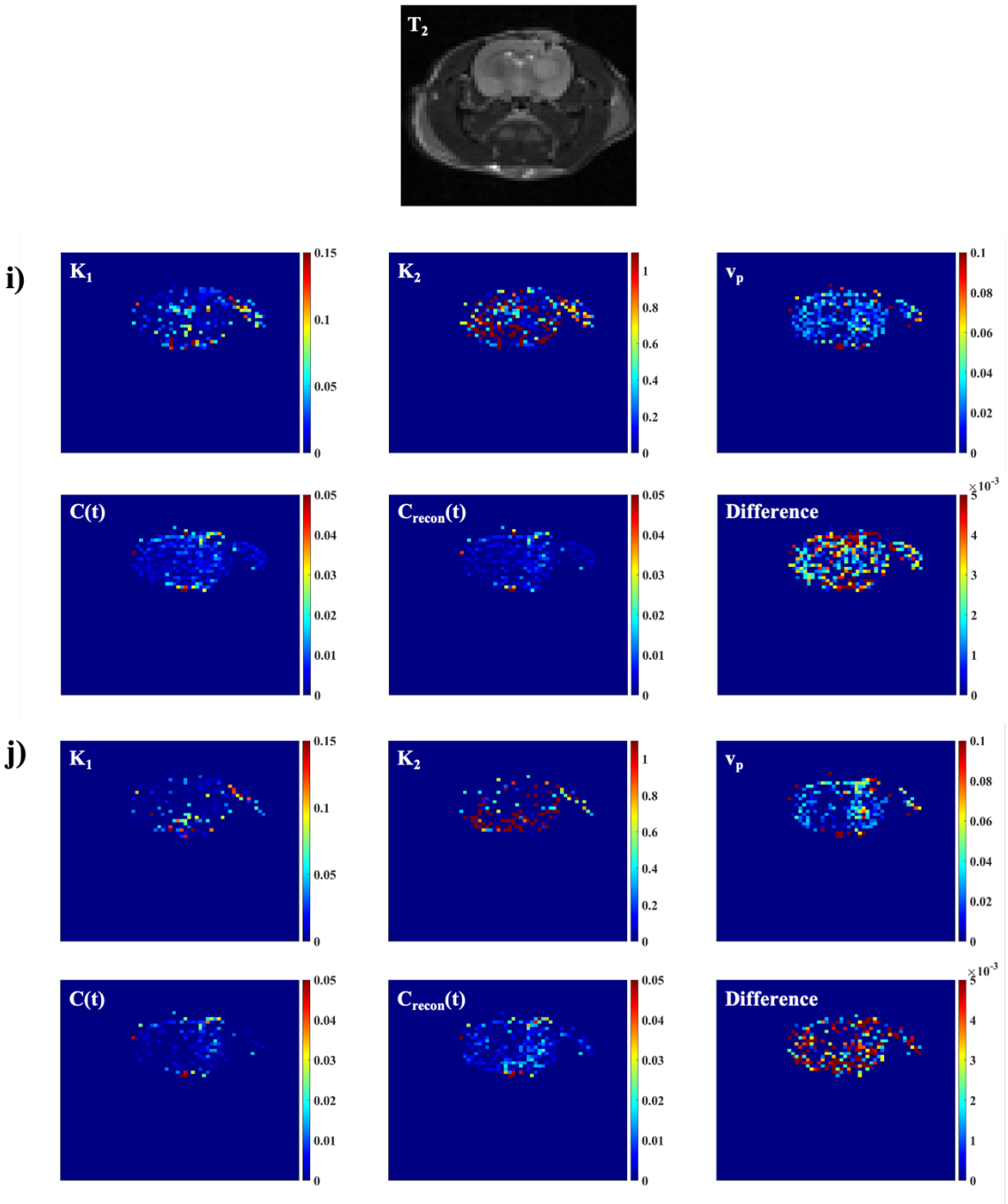
T2
i)
K1
K2
vp
C(t)
Crecon(t)
Difference
j)
K1
K2
vp
C(t)
Crecon(t)
Difference

Animal# 6

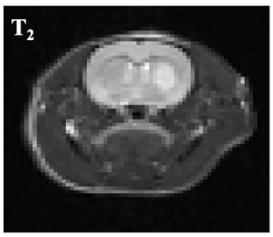
T2

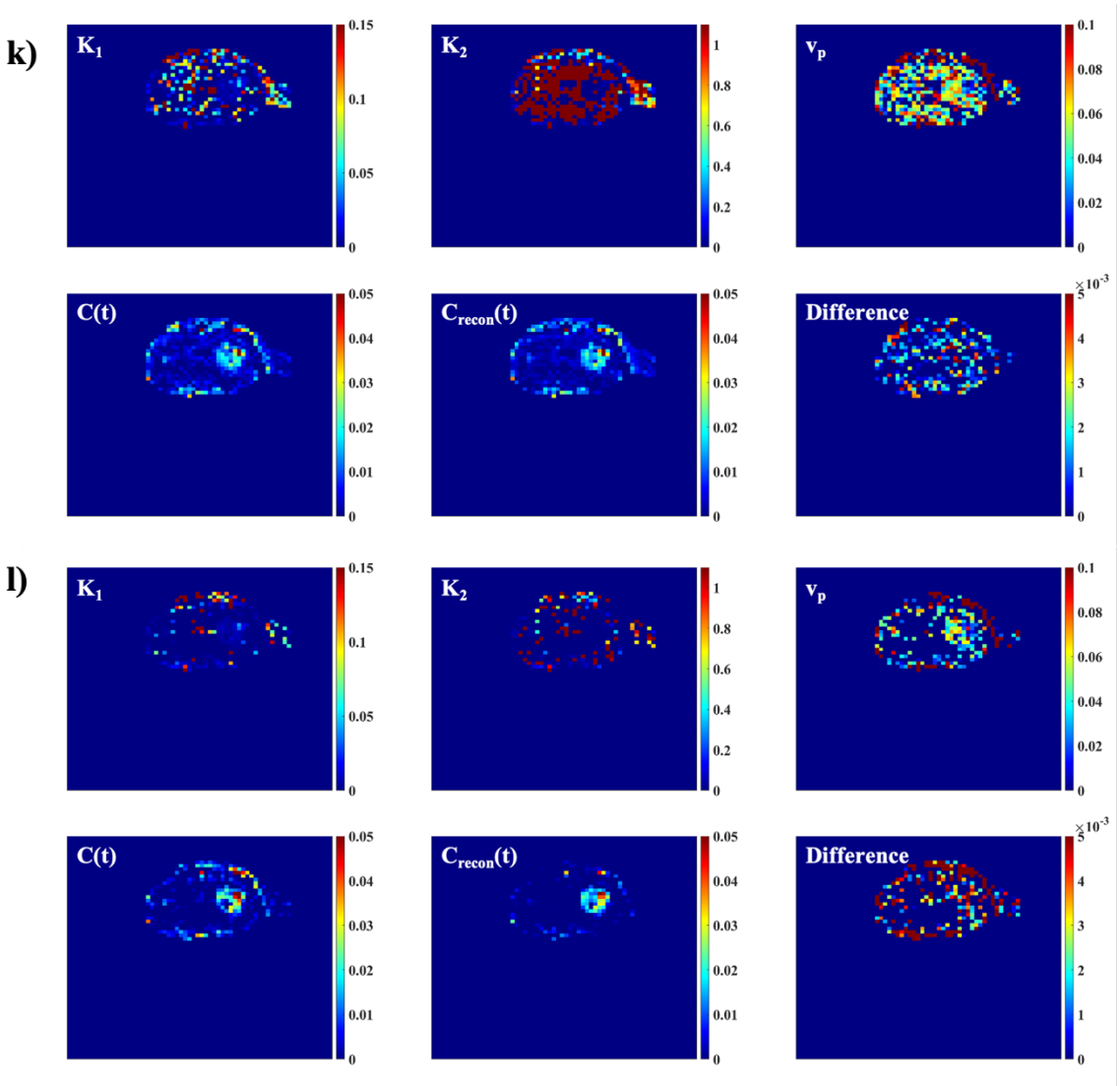
k)
K1
0.15
0.1
0.05
0
K2
1
0.8
0.6
0.4
0.2
0
vp
0.1
0.08
0.06
0.04
0.02
0
C(t)
0.05
0.04
0.03
0.02
0.01
0
Crecon(t)
0.05
0.04
0.03
0.02
0.01
0
Difference
×10-3
5
4
3
2
1
0
l)
K1
0.15
0.1
0.05
0
K2
1
0.8
0.6
0.4
0.2
0
vp
0.1
0.08
0.06
0.04
0.02
0
C(t)
0.05
0.04
0.03
0.02
0.01
0
Crecon(t)
0.05
0.04
0.03
0.02
0.01
0
Difference
×10-3
5
4
3
2
1
0

Animal# 7

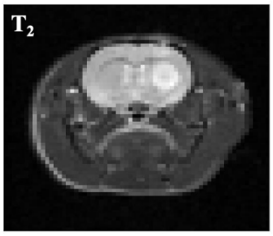
T2

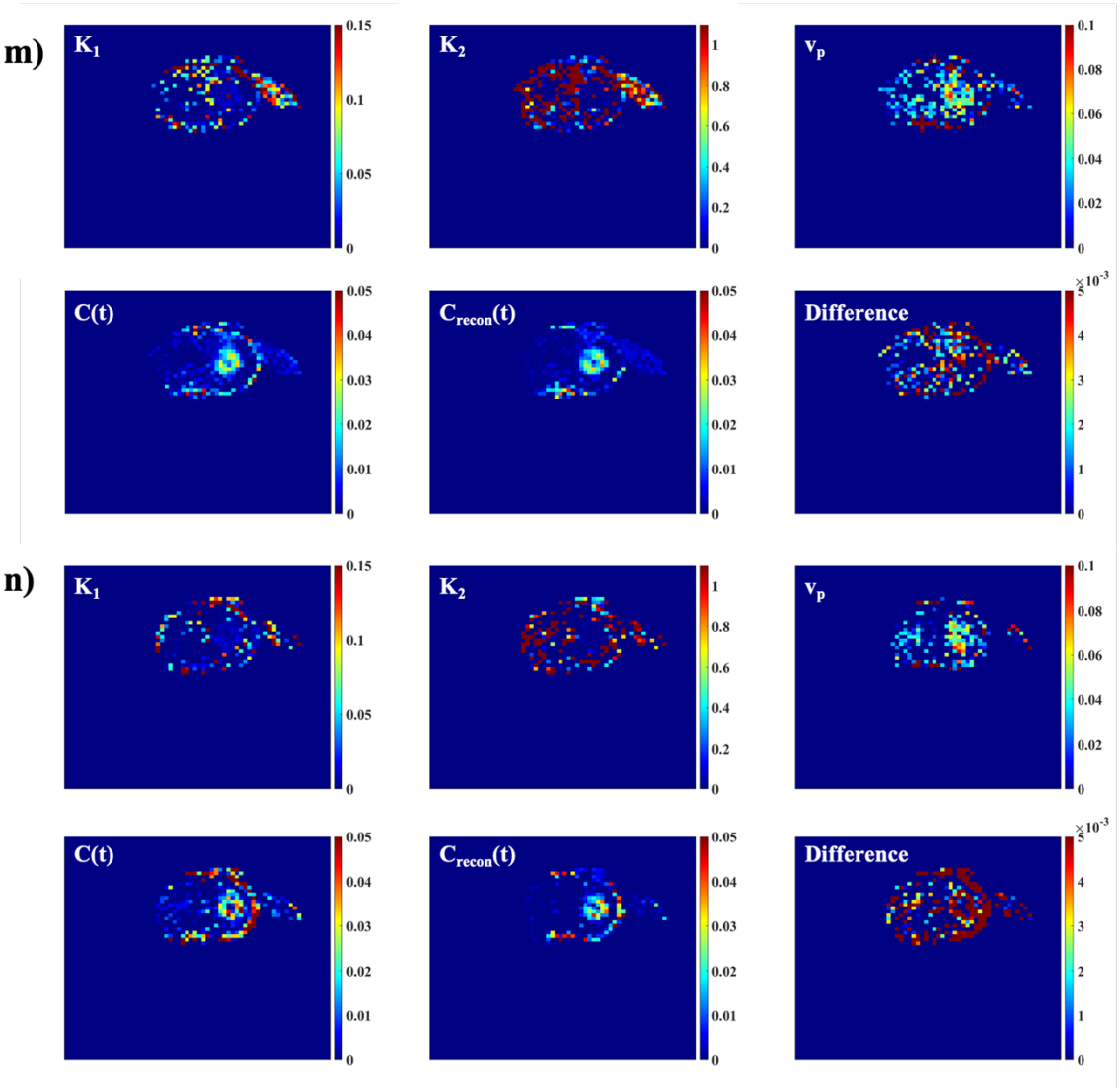
m)
K1
K2
vp
C(t)
Crecon(t)
Difference
n)
K1
K2
vp
C(t)
Crecon(t)
Difference

Animal# 8

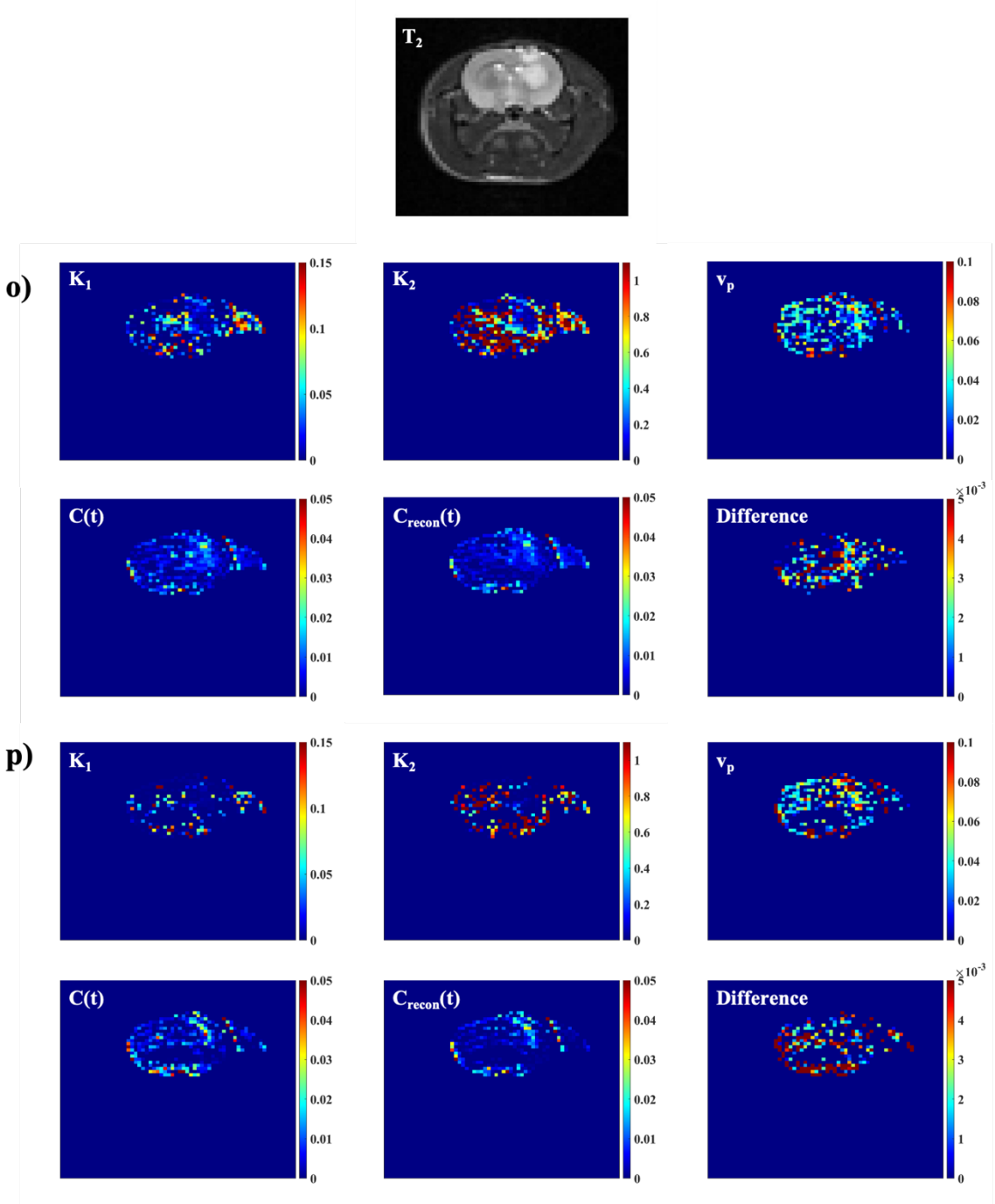

Figure 22 The T_2 weighted anatomical image and the pharmacokinetic maps and concentration maps of the individual animals in C6 cohort over 1h post-injection in a, c, e, g, i, k, m, o and 2h post-injection in b, d, f, h, j, l, n, p.

Table 5. Summarized K_1 values of each animal in 9L cohort 1h post injection in the tumor, contralateral brain, and muscle ROI s.

Animal K_1	Tumor	Contralateral	Muscle
Animal# 1 R1	0.0189 ± 0.0310	0.012 ± 0.0259	0.0710 ± 0.0882
Animal# 2 R2	0.0052 ± 0.0066	0.0086 ± 0.0161	0.0910 ± 0.0288
Animal# 3 R5	0.0175 ± 0.0117	0.0231 ± 0.0411	0.0894 ± 0.0614
Animal# 4 R204	0.0400 ± 0.0419	0.0443 ± 0.0644	0.0830 ± 0.0430
Animal# 5 R206	0.0037 ± 0.0057	0.0152 ± 0.0256	0.0781 ± 0.0518
Animal# 6 R208	0.0193 ± 0.0346	0.0168 ± 0.0265	0.0784 ± 0.0623
Animal# 7 R209	0.0246 ± 0.0326	0.0139 ± 0.0330	0.0826 ± 0.0567
Animal# 8 R210	0.0197 ± 0.0285	0.0485 ± 0.0706	0.0967 ± 0.0634
Cohort mean	0.0186 ± 0.0113	0.0229 ± 0.0151	0.0838 ± 0.0083

Table 6. Summarized K_2 values of each animal in 9L cohort 1h post injection in the tumor, contralateral brain, and muscle ROI s.

Animal K_2	Tumor	Contralateral	Muscle
Animal# 1 R1	0.5379 ± 1.3907	3.1197 ± 2.2234	0.5988 ± 0.7352
Animal# R2	3.4133 ± 3.4713	5.6350 ± 2.5224	1.0110 ± 0.2895
Animal# 3 R5	0.8097 ± 1.9030	5.6514 ± 2.0354	1.0333 ± 0.5510
Animal# 4 R204	0.8132 ± 1.0237	2.6153 ± 2.7842	1.0549 ± 0.5325
Animal# 5 R206	3.3135 ± 2.6132	1.7933 ± 2.0508	1.3900 ± 1.2676
Animal# 6 R208	1.8763 ± 1.9708	2.1081 ± 2.3536	0.9687 ± 0.4566
Animal# 7 R209	2.2036 ± 2.2016	2.9497 ± 2.1276	1.1155 ± 0.7839
Animal# 8 R210	2.3874 ± 2.2532	3.8402 ± 1.7293	1.4240 ± 0.9313
Cohort mean	1.9194 ±1.1238	3.4641 ± 1.4819	1.0745 ± 0.2583

Table 7. Summarized v_p values of each animal in 9L cohort 1h post injection in the tumor, contralateral brain, and muscle ROI s.

Animal v_p	Tumor	Contralateral	Muscle
Animal# 1 R1	0.0539 ± 0.0348	0.0329 ± 0.0141	0.0420 ± 0.0490
Animal# R2	0.0293 ± 0.0190	0.0173 ± 0.0066	0.0095 ± 0.0125
Animal# 3 R5	0.0515 ± 0.0280	0.0298 ± 0.0143	0.0205 ± 0.0331
Animal# 4 R204	0.0169 ± 0.0156	0.0173 ± 0.0244	0.0157 ± 0.0252
Animal# 5 R206	0.0457 ± 0.0168	0.0279 ± 0.0176	0.0175 ± 0.0228
Animal# 6 R208	0.0328 ± 0.0197	0.0239 ± 0.0175	0.0228 ± 0.0282
Animal# 7 R209	0.0275 ± 0.0185	0.0353 ± 0.0202	0.0190 ± 0.0294
Animal# 8 R210	0.0274 ± 0.0180	0.0196 ± 0.0175	0.0128 ± 0.0232
Cohort mean	0.0356 ± 0.0132	0.0255 ± 0.0070	0.0200 ±0.0099

Table 8. Summarized K_1 values of each animal in C6 cohort 1h post injection in the tumor, contralateral brain, and muscle ROI s.

Animal K_1	Tumor	Contralateral	Muscle
Animal# 1 R1	0.0363 ± 0.0532	0.0107 ± 0.0157	0.1058 ± 0.1015
Animal# 2 R2	0.0142 ± 0.0088	0.0267 ± 0.0272	0.0789 ± 0.0579
Animal# 3 R3	0.0111 ± 0.0358	0.0222 ± 0.0517	0.0821 ± 0.0943
Animal# 4 R4	0.0420 ± 0.0342	0.0495 ± 0.0486	0.0913 ± 0.0498
Animal# 5 R5	0.0151 ± 0.0295	0.0101 ± 0.0189	0.0969 ± 0.0631
Animal# 6 R200	0.0088 ± 0.0140	0.0242 ± 0.0321	0.0719 ± 0.0604
Animal# 7 R202	0.0166 ± 0.0402	0.0054 ± 0.0111	0.0899 ± 0.0322
Animal# 8 R203	0.0209 ± 0.0338	0.0302 ± 0.0543	0.0935 ± 0.0521
Cohort mean	0.0206 ± 0.0121	0.0224 ± 0.0141	0.0888 ± 0.0108

Table 9. Summarized K_2 values of each animal in C6 cohort 1h post injection in the tumor, contralateral brain, and muscle ROI s.

Animal K_2	Tumor	Contralateral	Muscle
Animal# 1 R1	0.6983 ± 1.5567	2.5268 ± 2.7867	1.2883 ± 0.9901
Animal# 2 R2	0.4831 ± 1.2446	5.6875 ± 2.5427	0.9960 ± 0.5625
Animal# 3 R3	1.3271 ± 2.5067	2.9507 ± 2.4156	0.7793 ± 0.6822
Animal# 4 R4	0.5544 ± 1.3954	2.3213 ± 2.7010	0.9763 ± 0.5368
Animal# 5 R5	0.8206 ± 1.9098	2.3684 ± 3.3732	0.9681 ± 0.5152
Animal# 6 R200	0.6373 ± 1.6319	4.1635 ± 2.4763	1.2589 ± 1.0672
Animal# 7 R202	0.1042 ± 0.3188	4.5847 ± 2.2974	1.0018 ± 0.2663
Animal# 8 R203	0.3860 ± 1.0324	3.6450 ± 2.8940	0.9857 ± 0.4420
Cohort mean	0.6264 ± 0.3566	3.5310 ± 1.2150	1.0318 ± 0.1659

Table 10. Summarized v_p values of each animal in C6 cohort 1h post injection in the tumor, contralateral brain, and muscle ROI s.

Animal v_p	Tumor	Contralateral	Muscle
Animal# 1 R1	0.0281 ± 0.0320	0.0153 ± 0.0120	0.0113 ± 0.0167
Animal# 2 R2	0.0267 ± 0.0200	0.0176 ± 0.0158	0.0263 ± 0.0358
Animal# 3 R3	0.0591 ± 0.0663	0.0295 ± 0.0161	0.0405 ± 0.0408
Animal# 4 R4	0.0152 ± 0.0180	0.0064 ± 0.0100	0.0077 ± 0.0117
Animal# 5 R5	0.0204 ± 0.0130	0.0176 ± 0.0099	0.0120 ± 0.0082
Animal# 6 R200	0.0529 ± 0.0259	0.0404 ± 0.0222	0.0342 ± 0.0494
Animal# 7 R202	0.0468 ± 0.0248	0.0247 ± 0.0126	0.0112 ± 0.0133
Animal# 8 R203	0.0257 ± 0.0282	0.0250 ± 0.0189	0.0122 ± 0.0169
Cohort mean	0.0344 ± 0.0162	0.0221 ± 0.0103	0.0194 ± 0.0125

Table 11. Summarized K_1 values of each animal in 9L cohort 2h post injection in the tumor, contralateral brain, and muscle ROI s.

Animal K_1	Tumor	Contralateral	Muscle
Animal# 1 R1	0.0104 ± 0.0218	0.0258 ± 0.0341	0.0024 ± 0.0012
Animal# 2 R2	0.0070 ± 0.0066	0.0040 ± 0.0119	0.0863 ± 0.0265
Animal# 3 R5	0.0216 ± 0.0140	0.0225 ± 0.0516	0.0777 ± 0.0586
Animal# 4 R204	0.0516 ± 0.0335	0.0406 ± 0.0228	0.0846 ± 0.0493
Animal# 5 R206	0.0300 ± 0.0274	0.0046 ± 0.0050	0.0548 ± 0.0563
Animal# 6 R208	0.0428 ± 0.0000	0.0249 ± 0.0300	0.0786 ± 0.0601
Animal# 7 R209	0.0208 ± 0.0275	0.0273 ± 0.0415	0.0503 ± 0.0563
Animal# 8 R210	0.0035 ± 0.0044	0.0133 ± 0.0328	0.0875 ± 0.0745
Cohort mean	0.0234 ± 0.0171	0.0204 ± 0.0124	0.0653 ± 0.0291

Table 12 Summarized K_2 values of each animal in 9L cohort 2h post injection in the tumor, contralateral brain, and muscle ROI s.

Animal K_2	Tumor	Contralateral	Muscle
Animal# 1 R1	0.5107 ± 1.6467	2.3650 ± 3.3422	0.0351 ± 0.0574
Animal# R2	1.8870 ± 2.4905	5.0424 ± 2.3428	0.9315 ± 0.2846
Animal# 3 R5	0.1966 ± 0.6423	4.9315 ± 2.4564	0.8208 ± 0.5706
Animal# 4 R204	1.7022 ± 1.5239	1.3046 ± 0.8083	1.1104 ± 0.6337
Animal# 5 R206	0.4218 ± 0.3824	1.3169 ± 2.5207	0.7630 ± 0.8604
Animal# 6 R208	0.5005 ± 0.0000	1.4376 ± 1.6415	0.8210 ± 0.5915
Animal# 7 R209	2.3337 ± 2.3680	1.8073 ± 1.9866	0.4236 ± 0.4437
Animal# 8 R210	2.0205 ± 3.2464	1.2407 ± 2.2267	0.7705 ± 0.5837
Cohort mean	1.1966 ± 0.8668	2.4307 ± 1.6204	0.7095 ± .3334

Table 13 Summarized v_p values of each animal in 9L cohort 2h post injection in the tumor, contralateral brain, and muscle ROI s.

Animal v_p	Tumor	Contralateral	Muscle
Animal# 1 R1	0.0944 ± 0.0514	0.0212 ± 0.0155	0.0617 ± 0.0280
Animal# R2	0.0282 ± 0.0233	0.0250 ± 0.0080	0.0137 ± 0.0148
Animal# 3 R5	0.0410 ± 0.0274	0.0329 ± 0.0204	0.0296 ± 0.0404
Animal# 4 R204	0.0084 ± 0.0131	0.0122 ± 0.0169	0.0122 ± 0.0169
Animal# 5 R206	0.0066 ± 0.0112	0.0238 ± 0.0102	0.0478 ± 0.0503
Animal# 6 R208	0.0001 ± 0.0000	0.0190 ± 0.0226	0.0203 ± 0.0340
Animal# 7 R209	0.0275 ± 0.0240	0.0173 ± 0.0194	0.0484 ± 0.0555
Animal# 8 R210	0.0367 ± 0.0172	0.0199 ± 0.0180	0.0288 ± 0.0497
Cohort mean	0.0304 ± 0.0299	0.0210 ± 0.0069	0.0331 ± 0.0177

Table 14 Summarized K_1 values of each animal in C6 cohort 2h post injection in the tumor, contralateral brain, and muscle ROI s.

Animal K_1	Tumor	Contralateral	Muscle
Animal# 1 R1	0.0096 ± 0.0179	0.0042 ± 0.0071	0.0635 ± 0.0917
Animal# 2 R2	0.0119 ± 0.0036	0.0540 ± 0.0505	0.0825 ± 0.0498
Animal# 3 R3	0.0092 ± 0.0297	0.0383 ± 0.0805	0.0508 ± 0.0694
Animal# 4 R4	0.0411 ± 0.0497	0.0776 ± 0.0727	0.0680 ± 0.0659
Animal# 5 R5	0.0071 ± 0.0187	0.0058 ± 0.0121	0.1089 ± 0.0808
Animal# 6 R200	0.0060 ± 0.0024	0.0128 ± 0.0178	0.0533 ± 0.0436
Animal# 7 R202	0.0076 ± 0.0037	0.0011 ± 0.0023	0.1119 ± 0.0712
Animal# 8 R203	0.0109 ± 0.0323	0.0185 ± 0.0424	0.0536 ± 0.0465
Cohort mean	0.0129 ± 0.0116	0.0265 ± 0.0276	0.0740 ± 0.0247

Table 15 Summarized K_2 values of each animal in C6 cohort 2h post injection in the tumor, contralateral brain, and muscle ROI s.

Animal K_2	Tumor	Contralateral	Muscle
Animal# 1 R1	0.5772 ± 1.7268	0.9968 ± 2.3267	0.7381 ± 0.9386
Animal# 2 R2	0.0232 ± 0.0048	5.0093 ± 2.1383	0.9771 ± 0.5227
Animal# 3 R3	0.8190 ± 2.0749	2.3988 ± 2.5897	1.3081 ± 2.5684
Animal# 4 R4	1.0360 ± 2.1310	2.3650 ± 2.5175	0.6076 ± 0.5452
Animal# 5 R5	0.8961 ± 2.4549	2.4966 ± 3.8431	1.2316 ± 0.7688
Animal# 6 R200	0.0024 ± 0.0039	1.6087 ± 2.8244	0.6975 ± 0.6109
Animal# 7 R202	0.0155 ± 0.0213	2.5276 ± 2.4039	1.0803 ± 0.5912
Animal# 8 R203	0.0995 ± 0.3273	1.8879 ± 2.6877	1.3385 ± 1.7518
Cohort mean	0.4336 ± 0.4451	2.4113 ± 1.1766	0.9973 ± 0.2889

Table 16 Summarized v_p values of each animal in C6 cohort 2h post injection in the tumor, contralateral brain, and muscle ROI s.

Animal v_p	Tumor	Contralateral	Muscle
Animal# 1 R1	0.0431 ± 0.0413	0.0226 ± 0.0143	0.0234 ± 0.0281
Animal# 2 R2	0.0427 ± 0.0201	0.0155 ± 0.0145	0.0238 ± 0.0347
Animal# 3 R3	0.0586 ± 0.0681	0.0219 ± 0.0155	0.0470 ± 0.0459
Animal# 4 R4	0.0262 ± 0.0320	0.0115 ± 0.0161	0.0261 ± 0.0329
Animal# 5 R5	0.0304 ± 0.0193	0.0144 ± 0.0087	0.0099 ± 0.0107
Animal# 6 R200	0.0472 ± 0.0243	0.0255 ± 0.0224	0.0509 ± 0.0734
Animal# 7 R202	0.0461 ± 0.0225	0.0294 ± 0.0102	0.0145 ± 0.0328
Animal# 8 R203	0.0549 ± 0.0371	0.0327 ± 0.0241	0.0301 ± 0.0504
Cohort mean	0.0436 ± 0.0110	0.0217 ± 0.0075	0.0282 ± 0.0144

4. Discussions and conclusion

GdDO3NI , due to reduction of the nitroimidazole moiety and subsequently binding to the thiol proteins in the hypoxic regions, can detect hypoxia. The retention of GdDO3NI has been shown to correlate with hypoxia in different tumor types[2,3]. Relaxivity of the contrast agent is its crucial properties in generating signal enhancement. The two batches of the synthesized contrast agent showed about one unit (~ 1 $s^{-1}mmol^{-1}L$) difference in r_1 relaxivity. To explain the discrepancy we looking into purification step would be the first step. The purification technique used in this study was column chromatography. Applying this technique to separate closely similar molecules is not trivial and based on the individual's expertise could result in slightly different purity of the desired molecule. In any chemical reaction there are always side reactions. These reactions result in molecules that are not favorable and influence the purity of the final product. The difference in relaxivity could be attributed to the different molecules in the final product i.e. the purity of the desired chelator molecule. In other words, the chelating molecule could also be molecules other than GdDO3NI , which have different relaxivity. The different relaxivities average out to a single value attributed to the mixture.

The gold standard techniques in detecting hypoxia, such as PET and IHC, which share the nitroimidazole targeting moiety, were used to verify the hypoxia targeting contrast agent. The main cause of hypoxia can be ascribed to the growth of the tumor. A tumor as a hyperactive system demands a lot of nutrients and oxygen; thus, the tumor begins angiogenesis, but the lack of the genetic checkpoints results in an immature, chaotic,

nonorganized, and leaky vasculature system. This generates regions deprived of enough oxygen and nutrients provided by the bloodstream. The retention of GdDO3NI in the big tumor shows the severity and distribution of hypoxia in the tumor, which is in good agreement with the other hypoxia detecting techniques. The integrity of the blood-brain barrier (BBB) prevents the contrast agent's extravasation to the brain tissue. However, BBB is mostly compromised in brain tumors. The MR results correlated well with the PET and IHC data for the same tumor. The time course data shows that the well-perfused muscle tissue has the faster uptake of the contrast agent than the normal and compromised brain tissue. However, the clearance process is distinctly different from the muscle and tumor tissue. The muscle and contralateral brain tissue show a sharp drop in contrast agent concentration than the tumor, especially in the larger tumors, implying a slower pharmacokinetic and retention of contrast agent in hypoxic regions. As the uncorrected data showed, there was some drift in the time course graphs. The slight increase in the signal can be attributed to the animal's reduced temperature over the 2h of the experiment. Even though the rats are placed in water heating beds, the heat exchange happens at the contact points, and the top part of the animals are exposed to the air inside the MR bore. The temperature in the bore is colder than the body temperature and cooler than the room temperature. The MR signal increase linearly is attributed to the decrease of the temperature over time[126]. The phantom experiment could confirm the temperature change hypothesis; the intensity of the signal consistently increases for about 40 min, and then it plateaus. The equation describing the relationship between magnetic moment and temperature is $M_z^0 = \left|\vec{M}\right| = \frac{\gamma^2 \bar{h}^2 B_0 N_s}{4KT_s}$ [126], where γ is the gyromagnetic ratio, h is the Plank's

constant N_s is the total number of spins, K is the Boltzman's constant, and T_s is the absolute temperature. The water phantom was kept at room temperature (25 °C), and using the intensity enhancement data for the phantom and the above equation for a change of ~1.5% enhancement in signal intensity rises from 19 °C temperature inside the magnet bore. The recorded temperature for the magnet bore was 19.5 °C, which is very close to the theoretically calculated temperature. It is also important to discuss the effect of temperature on the relaxation rates. In general, T_1 has a direct relation with temperature ($T_1 \propto \exp(-E_a/kT)$). However, to simplify the equations the relation is usually estimated as linear for for temperatures less than 50 degree Celsius. The $f(T_1,T)$ has different slopes and intercepts for different materials[127,128]. Using Equation 8 and the fact that any drop in temperature reduces the value of T_1 the signal intensity increases over time as the temperature decreases. The temperature coefficients of T_1 of different tissues are different, for example white mater has 3 ms/1 ºC and cortex has 17 ms/1 ºC[128] at 3T in a temperature range of 4-37 degree Celsius. These two phenomena which relate to the temperature drop could explain the drift of the signal over time. After applying the conditional smoothening approach to the data and eliminating the drift resulting from the temperature drop over time. Based on the definition, the NDE value is indicative of the contrast agent retention and hypoxia in the tumor site, which explains the enhancement of the tumor region in MR images. The correlation between the tumor size and the NDE value was assessed for the two cohorts. The C6 cohort did not display any linear correlation between the tumor size and the NDE values, even though the NDE values were positive, i.e., there were hypoxic regions in the tumor. This can imply the C6 tumors show hypoxia after a certain size and

are not correlated with its size, which is in good agreement with the published reports. It is reported the C6 tumors cause a minimal immune response in the body[129]. Besides, the hypoxic region in tumors increases their immune tolerance because of the impeded transportation and residence of immunocompetent cells in the tumor tissue[33]. Then C6 tumors develop hypoxic regions even in small sizes and increase their immune tolerance. On the other hand, the 9L cohort showed a weak correlation between the NDE value and tumor size. The NDE values of this cohort are comprised of positive and negative positive values. The 9L tumors are reported to be mostly normoxic compared to C6 tumors[109]. The positive values show the retention of the contrast agent, implying hypoxic regions. Suppose the positive values of the NDE were used to assess the correlation. In that case, there is a robust linear correlation between tumor size and the NDE value with r^2=0.99, meaning if the tumors are developing hypoxic regions, there is a relation between their size and severity of hypoxia. Pharmacokinetic modeling of the data allows more characterization of the tumor microenvironment and enables simultaneous assessment of perfusion and hypoxia parameters in the tumors. In DCE studies using conventional contrast agents, K_2 is defined as K^{trans}/v_e where v_e is the extravascular volume fraction; however, with hypoxia targeting contrast agents, K_2 implies different meanings in different locations. In the normoxic regions, K_2 reports the same information as the conventional DCE parameter (K^{trans}/v_e), but in hypoxic regions, the K_2 value is influenced by the hypoxia-dominated mechanism i.e. retention of contrast agents due to chemical bond. Stratification based on the tumor model did not show significant difference in the mean values of the parameters in tumor region.

CHAPTER 4

DEVELOPING A NOVEL HYPOXIA TARGETING CONTRAST AGENT

Purpose: In this study, we synthesized, characterized and tested a novel hypoxia targeting contrast agent (FOBNI) for imaging hypoxia using magnetic resonance imaging (MRI).

Methods: DFOBNI was synthesized and purified using reversed phase chromatography. After acquiring cytotoxicity data, the magnetic properties were studied to measure the relaxivity of the contrast agent. Relaxivity experiment was performed in a homemade designed phantom containing nine different concentrations, which was capable of adjusting the temperature. MR studies conducted in a preclinical magnet and at 7T magnetic field. The ability of the contrast agent in targeting hypoxic regions was studied in vitro with 3D cell structures under low levels of oxygen.

Results: The synthesis was validated by the NMR spectrum of the compound along with mass spectroscopy. The cytotoxic assay showed no significant changes to the cells' viability over the period of 8h exposure to the contrast agent. The relaxivity of FOBNI was measured to be r_1=0.51 $s^{-1}mmol^{-1}L$ and r_2=4.51 $s^{-1}mmol^{-1}L$. FOBNI retention in the hypoxic condition is an indication of its performance under the proposed mechanism, which was investigated with a series of in vitro studies under normoxic and hypoxic conditions.

Conclusion: FOBNI was successfully shown to visualize hypoxic regions.

1. Introduction

Inadequate supply of oxygen known as hypoxia is an environmental feature that can affect the outcome of different pathologies. It is also defined as constrained molecular oxygen electron transport [1]. Hypoxia influences the tissue microenvironment and deviates the tissue and cell function from normal. For instance, it negatively affects the immune system response [33], tumor invasiveness [131] and metastasis[36,132]. There are extensive studies on hypoxia in cancer, traumatic brain injury, and tissue implants research areas. Hypoxia can be the result of many factors including impaired oxygen delivery to the tissue because of abnormal angiogenesis, disruption of the blood vessels or limited oxygen diffusion. For example, in cancer the highly proliferating tumor cells demand more oxygen and nutrients, which results in the formation of new and disorganized blood vessels (neoangiogenesis). These vessels are not fully functional, are leaky and fail to rectify reduced oxygen levels. Some of the important complications known from and caused by hypoxia are resistance to chemo- and radiotherapy, increased tumor aggression, metastasis in cancer, alteration of therapy and neurological outcomes in TBI and success of transplanted tissue or implanted devices; these may have a direct impact on the patients' survival. Under hypoxic conditions cells' energy production pathway alters to glycolysis to reduces their need for oxygen. Due to lack of oxygen consequently lack of oxygen radicals the radiation is not very effective in hypoxic tumors. [133]

Considering the importance of hypoxia, it is become an important therapeutic target for monitoring tumor progression, the treatment response and developing hypoxia activated prodrugs. Since the hypoxic condition is harsh to survive for normal cells, the number of

surviving cells is limited; this requires very precise methods and techniques to detect and study hypoxia. There are mainly two distinct approaches to study hypoxia, using endogenous markers like HIF1-alpha[134], carbonic anhydrase IX (CA IX)[135], and endoplasmic reticulum disulphide oxidase 1α (ERO1α)[136] and or exogenous markers that target hypoxia. The manifestation of the extend of hypoxia in tissue depends on the applied techniques and methods [36]. For example, it is reported the detected hypoxic regions with endogenous markers do not exactly correlate with the result of the pimonidazole staining approach translating; the pimonidazole staining can detect severe hypoxic regions and may not accumulate in the HIF1 active regions[137].

It is shown nitroimidazoles accumulate in hypoxic tissues and hypoxic cells. The main proposed mechanism for the accumulation of these compounds follows the same reasoning for resistance to radiotherapy which is the lack of oxygen and oxygen radicals. Initially the nitroimidazoles undergo a bio-reduction by nitroreductase enzymes such as NADPH; in this process the nitro group acquire an electron and generate a radical in oxygen available (normoxic) conditions the molecular oxygen oxidizes the nitro radical to reproduce the inert molecule subsequently the superoxide anion is transformed to hydrogen peroxide by superoxide dismutase [8]; however, in the absence of oxygen they create a covalent bound with thiols groups. This important feature has been the main motive in generating hypoxia activated prodrugs, imaging agents and also antibiotics for anaerobic organisms [138]. Pimonidazole, the most successful member of the nitroimidazoles' family, has been used to study hypoxia in animals [139,140]and humans [44,141]. While there are pieces of evidence showing the binding of nitroimidazoles to hypoxic cells and the surrounding oxygen levels

are correlated, there is no published and known report on calibration for retention of these molecules and oxygen tension[142]. Moreover, there is no clear and detailed mechanism of the binding reaction of nitroimidazoles and cellular components [138,139].

Even though fluorescence spectroscopy and immunohistochemistry approaches to study hypoxia are very accurate and provide high spatial resolutions [143]. Noninvasive investigation of hypoxia with advanced techniques can eliminate the potential complications resulting from invasive procedures compensating the resolution and can provide further vital information about tissue microenvironment and tissue characteristics like pharmacokinetic properties shedding light on personalized therapy. The reported approaches to detect nitroimidazoles include scintigraphy[144], ^{19}F-MRI[145], positron emission tomography (PET) [146], immunohistochemistry [50], high-frequency ultra-sound microscopy[147], SPECT, near infrared (NRI) [148], Electron Paramagnetic Resonance (EPR)[149] and proton Magnetic resonance imaging (MRI) [61]. Owing to its unique package of features like high resolution, deep tissue penetration, providing anatomical and functional images and more importantly being noninvasive, MR based techniques to study hypoxia are safe and versatile and favorable to scientists[2]. The contrast in MR images which comes from the influence of intrinsic properties of the environment on the magnetic properties of protons can be tailored for specific purposes. For example, the presence of MR contrast agents alters the image contrast by changing the relaxation rate of the surrounding proton. The relaxation rate of tissue affected by the contrast agent is described by $R_i = [C]r_i + R_0$, where [C] is the concentration of the contrast agent, r_i is the relaxivity of the contrast agent, and R_0 is the inherent relaxation rate of the tissue[57]. There have been

multiple efforts to design novel contrast agents to address different biological and physiological questions[61,150,151]. Hypoxia, a therapeutic target, can be mapped with MRI if a hypoxia targeting contrast agent is introduced to the region of interest. Rojas-Quijano et al. developed gadolinium tetraazacyclododecanetetraacetic acid monoamide conjugate of 2-nitroimidazole (GdDO3NI) [61] to target hypoxia and visualize it utilizing MRI. Because GdDO3NI has the same targeting moiety of pimonidazole it is assumed to follow the same mechanism of reactivity under hypoxic conditions with proteins. The contrast agent has shown successful results in prior studies, in subcutaneous prostate cancer [2] and in lung tumors[3]. This successful study opens up the opportunity to use GdDO3NI in other pathologies like TBI[28].

Gd, which is a strongly paramagnetic heavy metal, is routinely and widely used as the MR contrast agent by chelation with a biocompatible ligand which is typically cleared through the kidneys. While widely used, there are serious concerns for patients with impaired kidney function as well as recent studies showed Gd accumulation in the bone and brain tissue even in patients with no renal impairment[152]. Moreover, The reported potential drawbacks of Gd based contrast agents include cytotoxicity, negative effects on cell proliferation, and low cellular uptake[153]. These are convincing enough for researchers to investigate and develop other non Gd based contrast agents to replace the existing contrast agents. Iron, a physiological ion, is capable of generating contrast in MR images due to its paramagnetic properties. Iron is the most abundant metal on earth, and it has important roles in physiological processes in the human body such as oxygen transport, DNA synthesis, and in the formation of several biologically important enzymes[153]. Iron-based

contrast agents are considered versatile and capable of being engineered for different applications with the highest sensitivity. Deferoxamine B (DFOB) is a linear trihydroxamic acid siderophore. Siderophores are compounds that are secreted in bacteria as a result of Fe (III) deficiency[154]. DFOB and other siderophores are very efficient in gleaning Fe (III) from an inorganic or biological source. DFOB is a well-known siderophore, because of its clinical applications in patients with transfusion-dependent blood disorders[155]. Among the important features of DFOB such as antioxidant[156], anti-Alzheimer[157] and antitumor activities[158] we will highlight the following with emphasis on imaging contrast agent. It is used in radiometal-based imaging; its low cost, solubility in water and organic solvents, and free amine moiety make DFOB a good and safe host for iron atoms to generate contrast in the MRI context. We have been inspired by these rich features of DFOB and have started an investigation of the potential iron-based hypoxia targeting contrast agent. Here we propose synthesis and characterization of an iron-based hypoxia targeting contrast agent, to eliminate Gd based complications and provide a cheaper and more economical alternative contrast agent to detect hypoxia using the mighty MR imaging modality. In this study we envisioned that the attachment of nitroimidazole moiety to DFOB, an FDA approved drug for patients with iron toxicity, and pre-chelation of the synthesized compound could be used as hypoxia targeting contrast agent for MRI. The purpose of this study was to synthesize an iron based hypoxia targeting agent, and to study its potential cytotoxicity, hypoxia targeting and relaxivity properties.

2. Materials and Methods

2.1. Materials

DFOB mesylate, HBTU, HOBT, DIPEA and reversed phase silica were purchased from Sigma-Aldrich (USA). TFA, DMF, Methylene chloride, Methanol, Acetonitrile were purchased from Oakwood Products, Inc. (USA) and used without further purification. Unless otherwise mentioned, the water used for all the experiments requiring water was ultrapure (Millipore) water. The dialysis tubes with a molecular weight cut-off of 100-500 Da were purchased from Spectrum Laboratories Inc. (USA). Cell culture media reagents were from Genesee (USA). Alamar blue was obtained from Bio-Rad Laboratories, Inc. (USA).

2.2. Synthesize

Synthesis of DFOBNI was performed through two major steps. In the first step the linker (6-(2-nitro-1H-imidazol-1-yl)hexanoic acid) was synthesized through the published report[61]. In brief, 2-nitroimidazole 1.05 equivalents of ethyl 6-bromohexanoate and 2.5 equivalents of potassium carbonate were mixed in acetonitrile. The mixture was stirred using a magnetic stirrer under reflux condition for one week. Afterwards, the mixture was cooled down to room temperature and filtered using gravity filtration and the solvent was removed under reduced pressure. The residual then was dissolved in ethyl acetate and followed by three times washing with water and drying with sodium sulfate. Finally, the solvent was removed under reduced pressure to yield (77%) the intermediate product, ethyl 6-(2-nitro-1H-imidazol-1-yl) hexanoate. The product was identified using ^{1}H NMR

spectroscopy with chloroform-d as the solvent. The linker was obtained by dissolving ethyl 6-(2-nitro-1H-imidazol-1-yl) hexanoate in a minimal amount of concentrated HCl and stirring overnight and removing the solvent under reduced pressure to yield (99%) a yellow oil. The linker was characterized using ^{1}H NMR spectroscopy with DMSO-d_6 as the solvent.

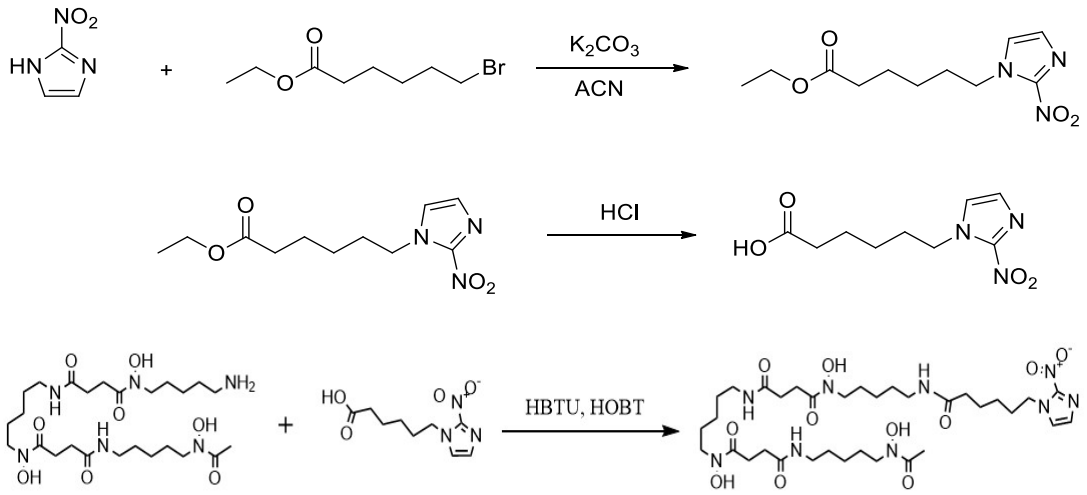

Scheme 3. General reaction scheme for conjugation of the linker to DFOB and the structure of DFOBNI.

To synthesize DFOBNI shown in Scheme 3 the carboxylic group of the linker was appended to the amine terminus of the DFOB. This reaction was conducted according to a published procedure with minor modifications[159]. The linker coupled to DBFO using HBTU/ HOBt/DIPEA coupling agent system. The used DFOB to linker ratio was 1-1.2. A suspension of the linker, DFOB, HBTU, and HOBt in DMF was heated under N_2 at 50 °C for 1 h. Then the mixture was cooled down to room temperature followed by addition of DIPEA and stirring the suspension under N_2 flow overnight at RT. The reaction was

stopped by placing the reactor in ice cold water. Later the solvent was removed under reduced pressure. The residue was suspended in cold acetonitrile by sonication and the precipitate was collected to eliminate HBTU, HOBt, and other side products, if any. This step was repeated three times. Nuclear magnetic resonance (NMR) spectra for characterization of the compound were recorded on two Bruker NMR systems operating at 400MHz and 500 MHz fields. Electrospray ionization mass spectrometry (ESI-MS) was performed on a Bruker system at Arizona state university. Performing ESI-MS and ^{1}H NMR on the solid confirmed the presence of DFOBNI. The collected solid from reversed phase silica column chromatography was then dissolved in water and further purified on a reversed phase silica column using a 1-1 ratio of water and methanol as elute system. The solvent was removed using a high vacuum and the solid was used to chelate iron.

2.3. Chelation

For chelation of DFOBNI a 1-1 ratio of DFOBNI and $FeCl_3$ was mixed and the mixture was stirred for 1 h. The pH of the stirred mixture was kept in acidic to neutral conditions to reduce the possibility of the formation of insoluble ferric ion in an aqueous medium[160]. Then the mixture was poured in a dialysis tube with a molecular weight cut-off of 500 Da and placed in water to remove the unchelated iron; the dialysis process was repeated three times to ensure the mixture has no free iron.

2.4. Cytotoxicity

To study the cytotoxicity of DFOB we used NIH-3T3 fibroblast cells. The cells were exposed to different concentrations of DFOB for 4,8 and 24h under either hypoxic or normoxic conditions. Afterwards, the cells were washed with PBS and exposed to 10%

Alamar blue in media for 4h in their respective conditions. To assess the viability of the cells 100 µl of the exposed Alamar blue was collected in a 96-well plate using the spectrophotometer the absorbance was measured at 570 nm and 600 nm excitations and using a published protocol[161] the viability of the cells was calculated.

2.5. Relaxometry

The basic paramagnetic properties i.e., relaxivity of chelated DFOB (FOB) and FOBNI was measured at 7T using a preclinical Bruker MRI scanner. The relaxivity of the two molecules were studied using a home-made 3D printed phantom capable of controlling temperature. The phantoms contained nine different concentrations of each contrast agents in water from 0-4 mM for FOB and 0-10 mM for FOBNI. The imaging parameters for this study were as matrix size 64 x 64, the field of view 2.56 cm x 2.56 cm and TR=205-5000 ms, TE=10 ms for the T_1 map and TR=5000 ms, TE=8-200 ms for the T_2 map. The MR images were later analyzed in a homemade MATLAB code to calculate the T_1 and T_2 values for each pixel. Using the T_1 and T_2 values for each concentration and $R_i = [C]r_i + R_i^0$ equation the relaxivity values were calculated by a linear fit on R_i and [C][58]. Where R_i (i=1 or 2) is the relaxation rate of the tissue, [C] is the concentration of the contrast agent, r_i is the relaxivity of the contrast agent and the R_i^0 is the intrinsic relaxation rate of the water.

2.6. In vitro studies

The in vitro study for hypoxia targeting efficiency of FOBNI was assessed in a hypoxia chamber glove box capable of adjusting oxygen concentration, temperature and CO_2 and equipped with a small centrifuge unit. The 3T3 fibroblast cells were grown in a T-150 flask

once they reached the confluency of 80% divided equally to five T-75 flasks to ensure the flasks were identical before being exposed to contrast agents and different conditions. The cells were supplied with Dulbecco's Modified Eagle Medium (DMEM), fetal bovine serum (10 %), and penicillin/streptomycin (1%). Once the five flasks reached the confluency of 75-80% the growth media were replaced with the following mediums.

Two flasks were supplied with fresh culture media supplemented with DFOB, two with fresh media and FOBNI and one with just fresh media as control. The control and one FOB and one FOBNI labeled flasks were placed in a regular cell incubator at 21% O_2, 5% CO_2 and 37 °C and the remaining two flasks were transferred to the hypoxia chamber at 1% O_2, 5% CO_2 and 37 °C. All the samples were kept at defined conditions for 4 h before removing the media. The cells were washed three times with phosphate buffered saline (PBS) at the end of four hour incubation and were detached by being exposed to trypsin for 5 min. The collected cell mixtures in Eppendorf Tube were centrifuged at 1000 rpm for 5 min and the medium was removed. Afterwards, the cell pellets were suspended in PBS and again centrifuged three times to ensure the removal of unbound or free DFOB or FOBNI. Finally, to keep the cell pellets intact the tubes were filled with low temperature liquid agar and placed in the fridge to solidify.

2.7. MRI imaging

The samples were imaged using a rat brain surface coil at 7 T. The voxel wise T_1 and T_2 maps of the samples were calculated using MATLAB based software and the images from Variable Repetition Time Fast Spin Echo (VTR) Sequence and multi-echo spin echo sequence, respectively. The VTR sequence was performed with TE=8 ms and thirteen TR

values ranging between (205-5000 ms). The images in multi-echo sequence were acquired with TE ranging between 8-200 ms and TR=5000 ms. The field of view was 2.56 cm x 2.56 cm and the matrix size of 64 x 64 for all the experiments. The ROI analysis to calculate the T_1 and T_2 values for cell pellets were performed in MATLAB.

2.8. Statistics

All results are reported as means ± standard deviations (SD). For statistical comparisons unpaired t-test was employed and confidence intervals $\alpha = 0.05$, 95% was used between specific means.

3. Results

Since the DFOB molecule comes with a free amine group we planned to perform a coupling reaction between the carboxylic group of the linker, the hypoxia targeting molecule, and the amine group of DFOB. The NMR data of the intermediate product showed characteristic peaks at the following chemical shifts, Figure 23, Figure 24. ^{1}H NMR (400 MHz, $CDCl_3$) δ 7.11 (m, 1H), 7.07 (d, J = 0.8 Hz, 1H), 4.39 (t, J = 7.3 Hz, 2H), 4.09 (q, J = 7.1 Hz, 2H), 2.28 (t, J = 7.1 Hz, 2H), 1.85 (m, 2H), 1.65 (m, 3H), 1.36 (m, 2H), 1.22 (t, J = 0.9 Hz, 3H). The NMR spectra of the linker revealed the chemical bonds and the presence of the carboxylic group at the modified end. ^{1}H NMR (400 MHz, DMSO) δ 7.69 (s, 1H), 7.16 (s, 1H), 4.36 (t, J = 7.3 Hz, 2H), 2.20 (t, J = 7.3 Hz, 2H), 1.76 (m, 2H), 1.52 (m, 2H), 1.27 (m, 2H).

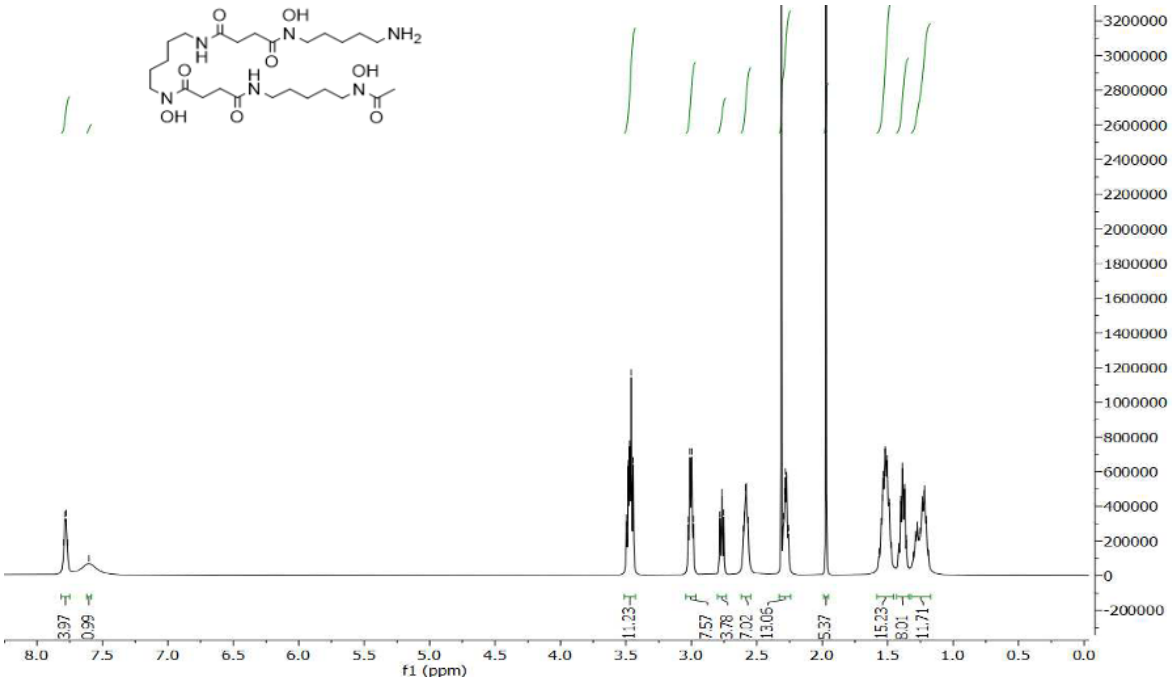

Figure 23 [1]H NMR (550 MHz, DMSO-d6): δ 7.8 (2H, amide), 3.46 (6H, -<u>CH2</u>-(N-OH)-), 3 (4H, -<u>CH2</u>-(NH)-). NMR spectra of DFOB in DMSO-d6 without further modifications.

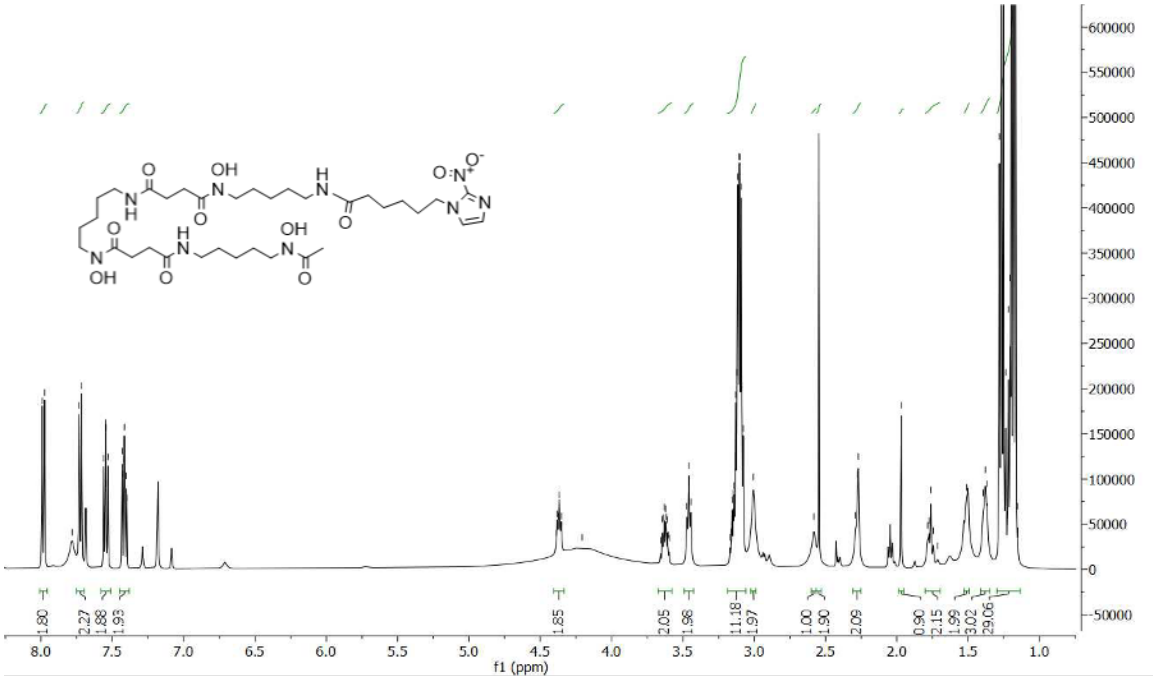

Figure 24 [1]H NMR (550 MHz, DMSO-d6): δ 7.8 (2H, amide), 3.46 (6H, -<u>CH2</u>-(N-OH)-), 3 (6H, -<u>CH2</u>-(NH)-). NMR spectra of DFOBNI in DMSO-d6 after column chromatography

To verify the synthesis of DFOBNI we recorded and compared the NMR spectra of DFOB and FOBNI. ESI-MS was able to detect the DFOB at 561.2 (Figure 25) in positive mode and showed a peak at 770 (Figure 26) that can be attributed to DFOBNI. The iron atom has a molar mass of about 56 g/mol, and when it is chelated by DFOBNI to generate FOBNI three hydrogens leave DFOBNI resulting in 823 molecular mass for FOBNI. Free iron ions can induce cytotoxicity and also influence paramagnetic properties. To eliminate the free iron ions from the product and small molecule impurities we used dialysis tubes with a molecular weight cut off of 500 Da. Dialysis was performed for an entire period of 48h in excess water. The water was stirred with a magnet stirrer and replace with fresh water three times to ensure the elimination of the free ions and impurities as shown in *Figure 26* b).

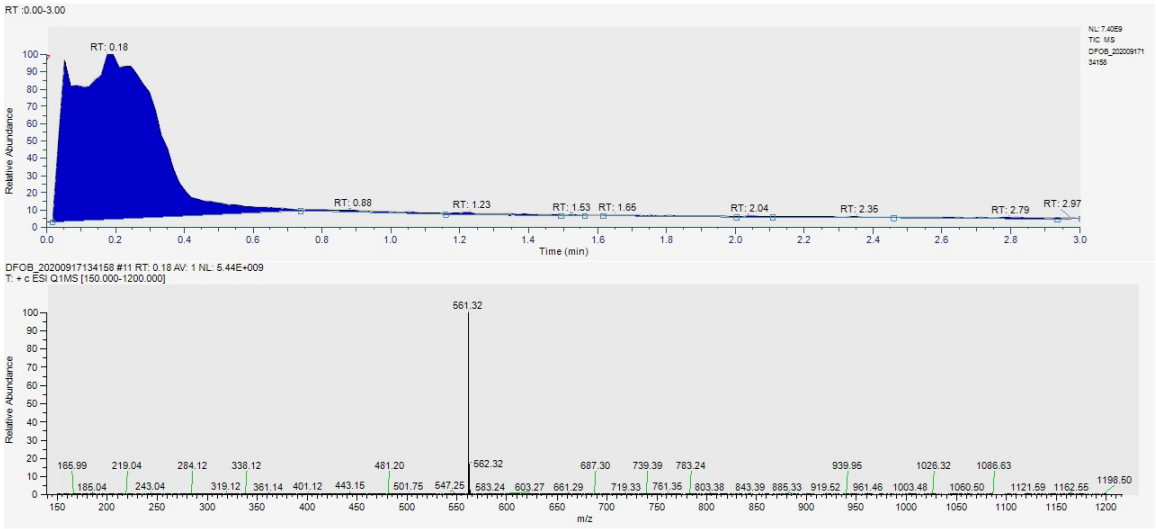

$[M+H]^+$ = 561.32, M = 560.32

Figure 25. Result of ESI-MS of DFOB. 50/50 A/B, A: 20 mM ammonium formate in water, and B: 20 mM ammonium formate in MeOH.

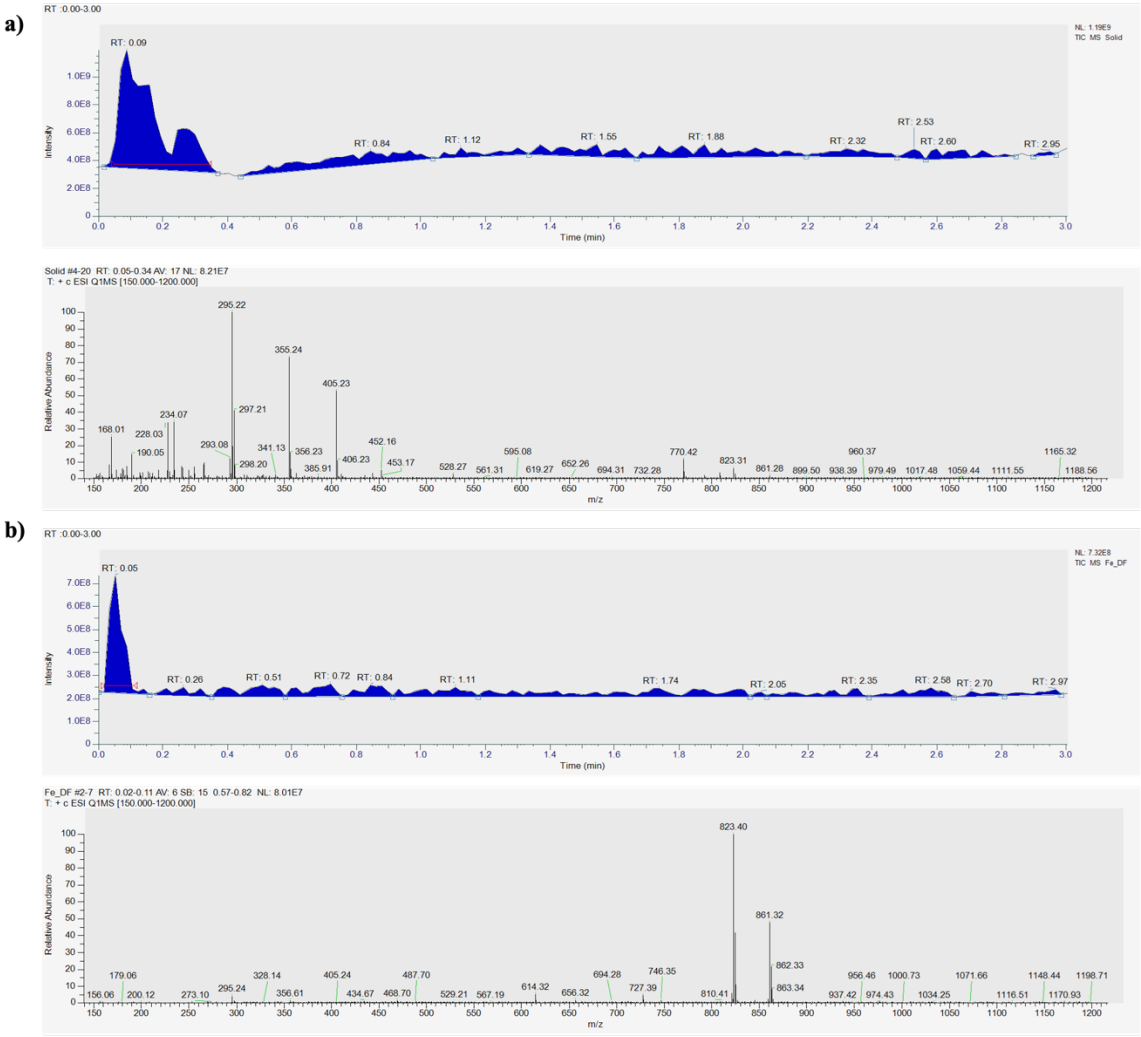

Figure 26. Result of ESI-MS of a)DFOBNI and b)FOBNI after dialysis. 50/50 A/B, A: 20 mM ammonium formate in water, and B: 20 mM ammonium formate in MeOH.

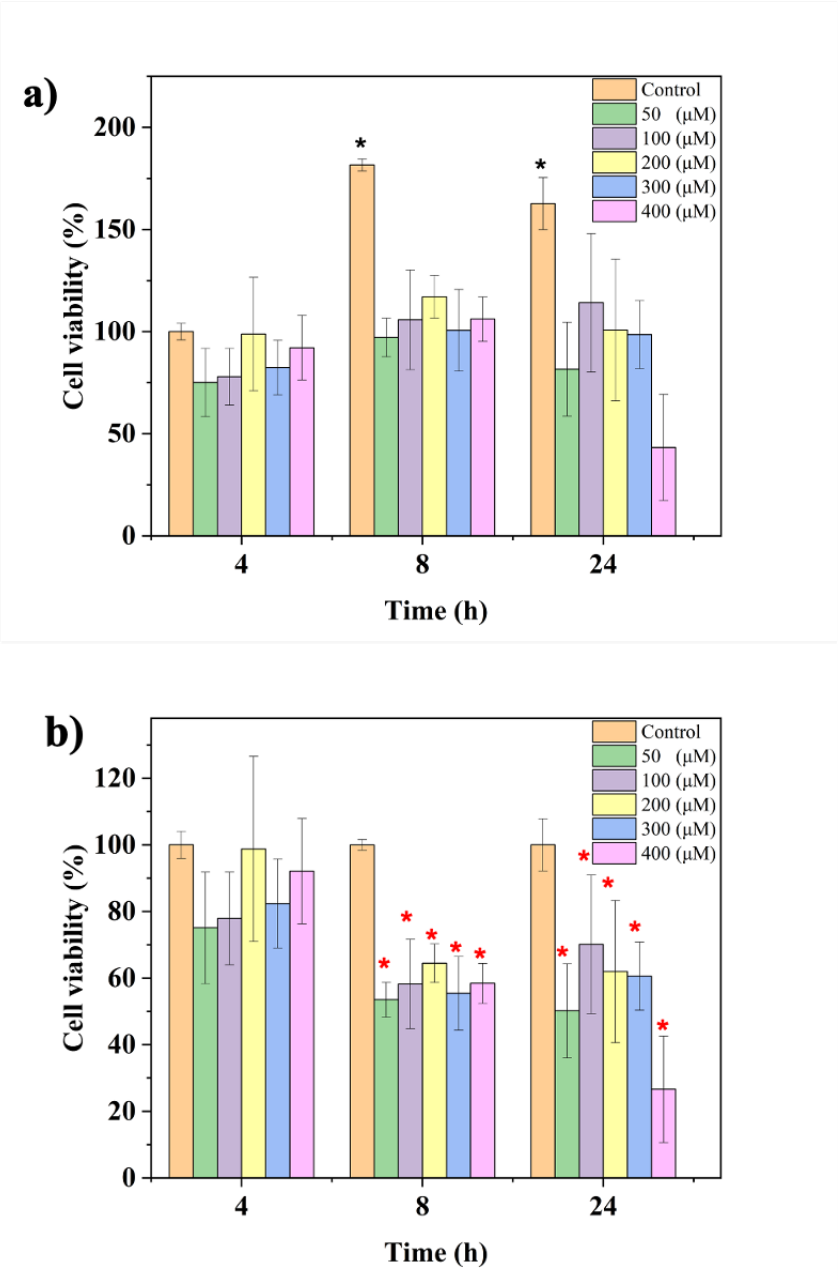

*Figure 27 Fibroblast 3T3 cell viability assay using Alamar blue after being exposed to FOBNI over different periods in normoxic condition a) represents the data using the control for 4h for all the time points and b) represents the data using the control in each time point the * in each case shows the statistical significance compared to control.*

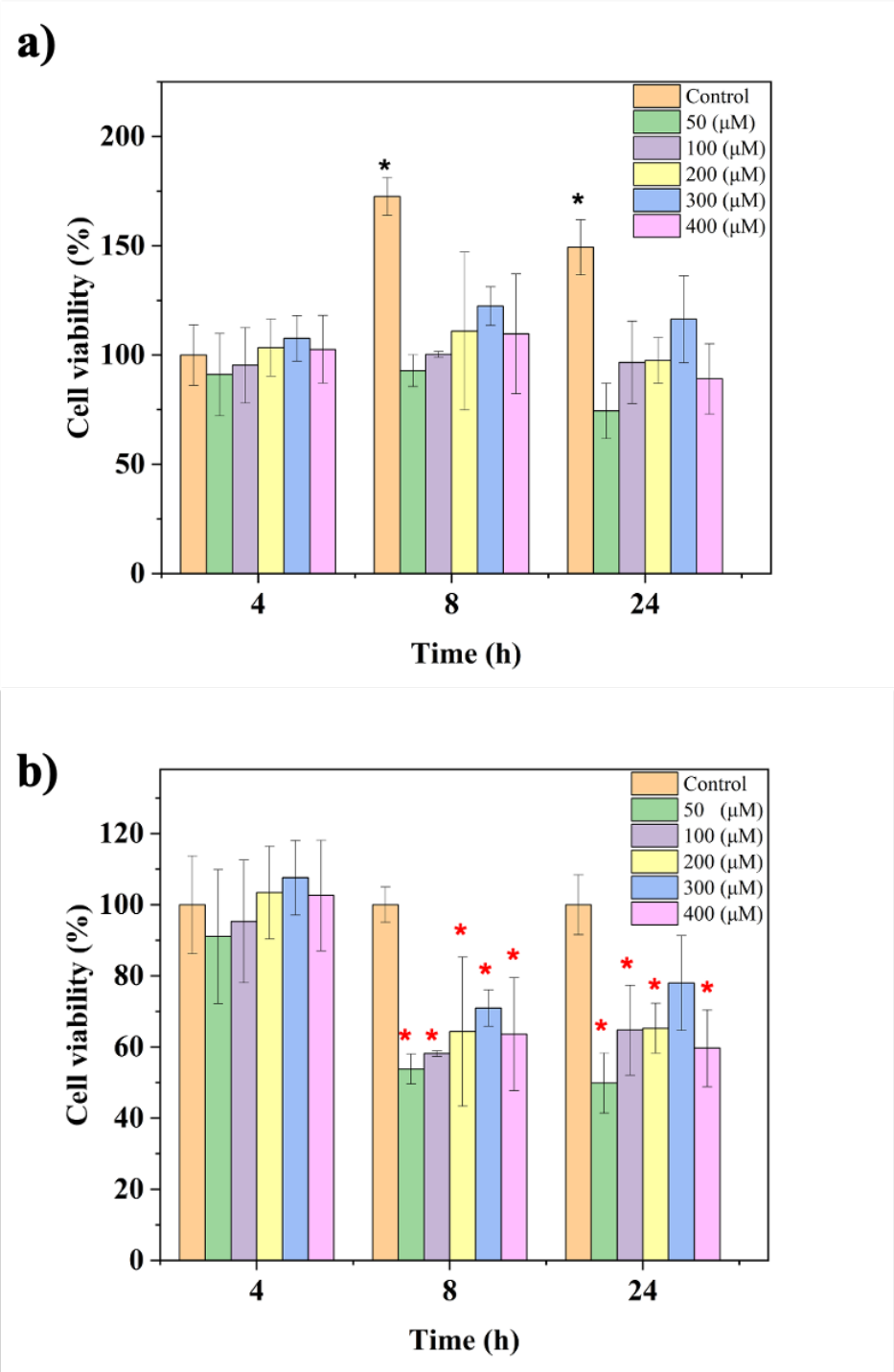

Figure 28 Fibroblast 3T3 cell viability assay using Alamar blue after being exposed to FOBNI over different periods in hypoxic condition a) represents the data using the

*control for 4h for all the time points and b) represents the data using the control in each time point the * in each case shows the statistical significance compared to control.*

Cytotoxicity assay for FOBNI was a viability test using Alamar blue. The results are summarized in Figure 27 for normoxic conditions and *Figure 28* for hypoxic conditions. The data showed no significant reduction (n=3) in the viability after up to 24h exposure of the cells to contrast agent at the concentrations of 100-400 μM in hypoxic and normoxic conditions when the control of the 4h exposure used to assess the viability. However, when the control of each time point used to assess the viability we noticed significant drop in cell viability after 8h and 24h of exposure in the fibroblast cells in hypoxic and normoxic conditions. The increased viability, which is a translation of reduced Alamar blue in control samples of 8h and 24h can be attributed to the increased number of the cells in the control wells. After seeding the cells the cell number in the control wells could increase and that can influence the amount of reduced compound in absorbance test.

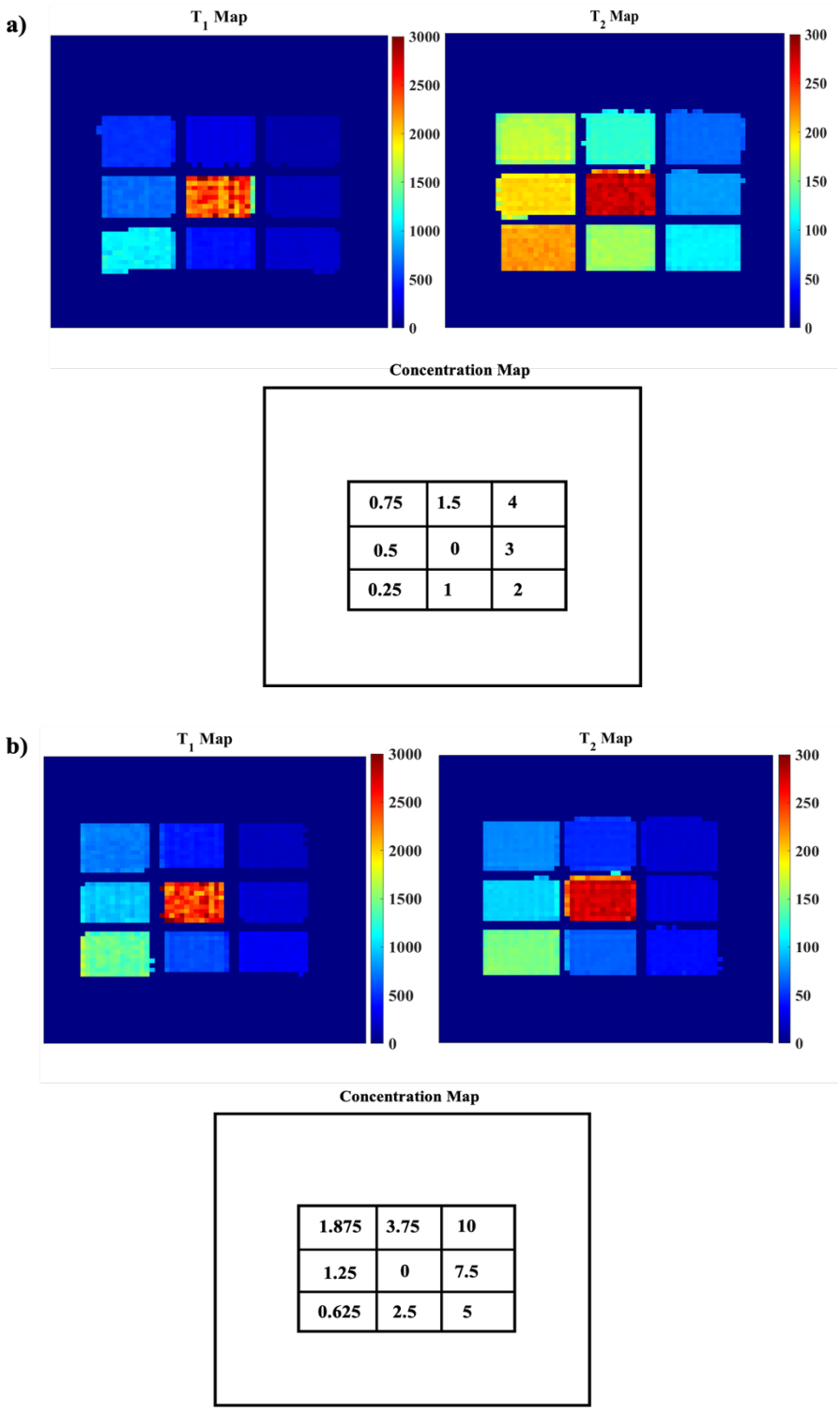

Figure 29 T_1, T_2 maps in ms and concentration maps in mM Fe for a) FOB and b) FOBNI.

Figure 29 a and b show the T_1 and T_2 maps for the phantom and a concentration map indicating the concentrations of FOB and FOBNI in each respective well.

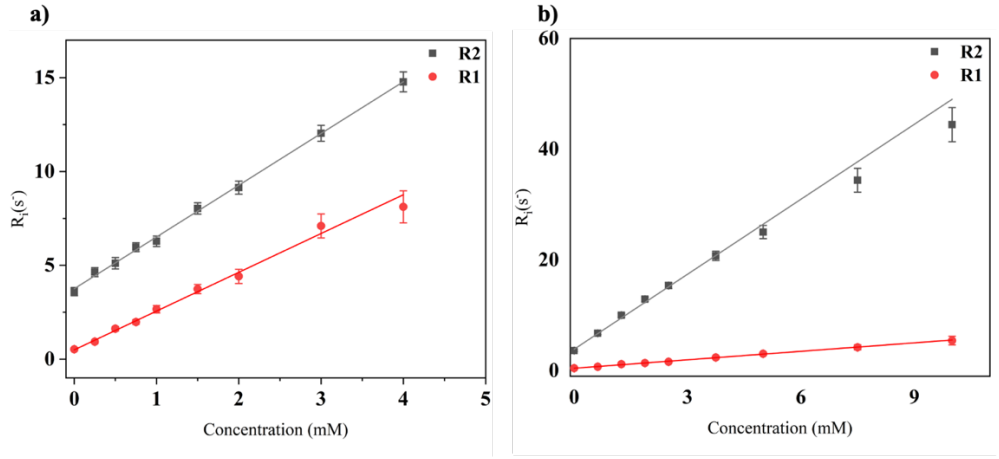

Figure 30. Relaxivity study of a) FOB with the fit curves representing the data as $\boldsymbol{R_1 = 2.06 \pm 0.06[C] + 0.49 \pm}$ *0.04(in red) and* $\boldsymbol{R_2 = 2.75 \pm 0.06[C] + 3.75 \pm 0.08}$ *(in gray) and b) FOBNI with the linear fit equations as* $\boldsymbol{R_1 = 0.51 \pm 0.1[C] + 0.44 \pm 0.03}$ *(in red) and* $\boldsymbol{R_2 = 4.51 \pm 0.14[C] + 3.87 \pm 0.19}$ *(in gray).*

Figure 30 a and b represent the result of the linear fit for R_1 and R_2 for the two contrast agents. The goodness of the fits assessed by the r^2 values and all the four data sets showed r^2>0.99. Using the linear fit function, the following equations are acquired for relaxation rate vs concentration, $R_1 = 2.06 \pm 0.06[C] + 0.49 \pm$ 0.04(in red) and $R_2 = 2.75 \pm 0.06[C] + 3.75 \pm 0.08$ (in gray) for FOB and $R_1 = 0.51 \pm 0.1[C] + 0.44 \pm 0.03$ (in red) and $R_2 = 4.51 \pm 0.14[C] + 3.87 \pm 0.19$ (in gray) for *FOBNI*.

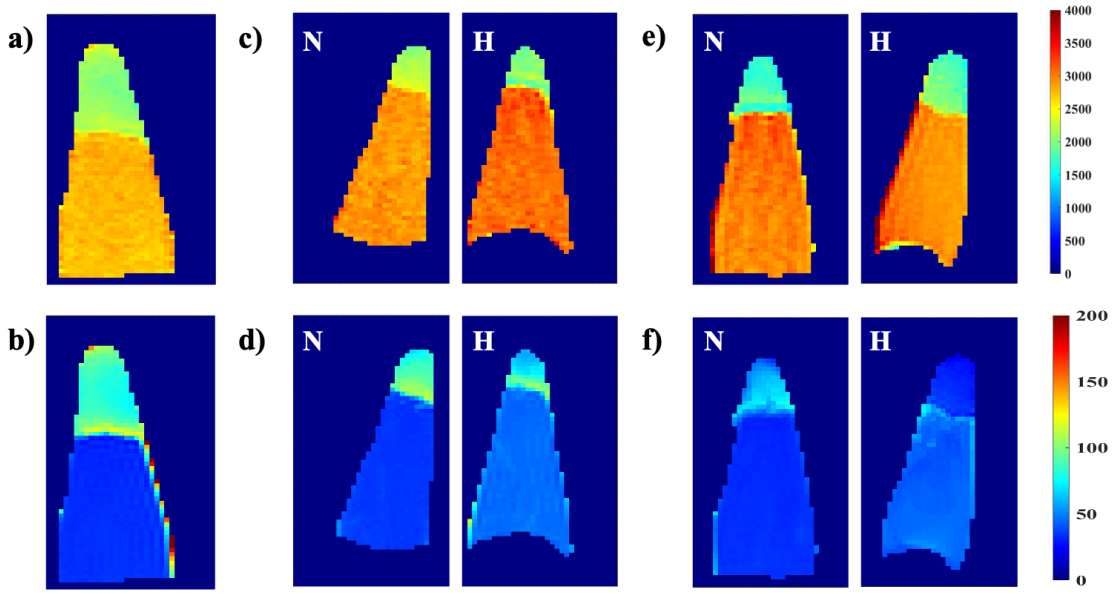

Figure 31. T_1 (upper row) and T_2 (lower row) maps of cell pellets, a) and b) control, c) and d) exposed to FOB, and e) and f) exposed to FOBNI.

Figure 31 represents the result of MRI for the in vitro experiment. The quantitative values are summarized in Table **17**.

Table 17 The relaxation times calculated for the control cells, FOB exposed cells under normoxic (N) and hypoxic (H) conditions and FOBNI exposed cells under normoxic (N) and hypoxic (H) conditions. The (*) shows statistical significance compared to the control.

Relaxation times (ms)	Control	FOB (N)	FOB (H)	FOBNI (N)	FOBNI (H)
T_1	2098±106	2280±222(*)	2002±143(*)	1793±165(*)	1909±162(*)
T_2	90.2±12.6	89.9±11.21	75.5±15.0(*)	59.3±9.3(*)	32.4±3.4(*)

The control cells showed a T_1 value of 2098±106 ms and T_2 value of 90.2±12.6 ms. The T_1 and T_2 values cells exposed to FOB under normoxic conditions were 2280±222 ms and 89.9±11.21 ms and under hypoxic conditions were 2002±143 ms and 75.5±15.0 ms respectively. However, normoxic values of the cells exposed to FOBNI for T_1 and T_2 were 1793±165 ms and 59.3±9.3 ms respectively, and under hypoxic conditions those were 1909±162 ms and 32.4±3.4 ms. The statistical analysis and unpaired t-test on the volumetric data i.e. taking into account the entire cell pellet (not just one slice) showed statistically significant changes in T_1 and T_2 values of the control cell sample compared to the exposed cells.

4. Discussion

There have been some reports on the complications and side effects of Gd based MR contrast agents in recent years[152,162]. Iron owing to its paramagnetic properties and its bio- and cytocompatibility can potentially replace Gd for design of contrast agents. DFOB as one of the clinically approved and available molecules has shown promising results in effectively and stably chelate iron ions. Furthermore, derivatives of 2-nitroimidazoles such as pimonidazole and ^{18}FMISO are extensively in practice to study hypoxia as the pimonidazole being the gold standard for invasive procedures and ^{18}FMISO for noninvasive PET imaging. Since the DFOB is already FDA approved developing a derivative of DFOB comprised of nitroimidazole moiety could serve as a safe MR imaging contrast agent. It will capture the advantages of MRI such as high resolution, being nonradioactive and providing anatomical information. The previously developed MR based contrast agent to study hypoxia, GdDO3NI , shows good sensitivity, results in high

resolution hypoxic regions and the hypoxic regions in MR images match the hypoxic region in pimonidazole staining. However, the general concern regarding gadolinium and its accumulation in bone and brain tissue[152] may be relevant here although no nonspecific accumulation has been reported for GdDO3NI . Here we seized the opportunity of the available primary amine group of DFOB and conjugated that with a 2-nitroimidazole derivative to synthesize DFOBNI, composed of a well-known iron chelator and hypoxia targeting moiety. The straightforward synthesis of DFOBNI is shown in *Scheme **3***, which was followed by purification steps. During the post processing steps the water-soluble product should be purified on either RP-HPLC or RP-column chromatography. RP-HPLC will result in fractions with higher purity; however, at times of inaccessibility of preparative scale RP-HPLC collecting the fraction on column chromatography will be sufficient. Assuming a successful coupling reaction the protons on the carbon connected to the primary amine would experience a different chemical shift, which appears in the NMR spectra as intensified peak at 3.46 ppm. The NMR spectra of the DFOB is characterized by a peak at 3.46 ppm for the protons bonded to carbon in $-CH_2-NH-$ group and a peak at 3 ppm for the protons bonded to carbon in $-CH_2-N(OH)-$ group. The chemical shift of protons on carbons bond to secondary amine at 3.46 ppm was used to monitor the conjugation reaction. The calculated ratio of the integration of the peaks at 3.46 ppm to the peak at 3 ppm for DFOB was 1.48. The ratio of the integration of the peaks at 3.46 ppm and 3 ppm resulted in 1.005, which was in good agreement with the theoretical value of 1 for the ratio. The chelation was performed with a 1:1 ratio of DFOBNI and Fe^{3+} to make FOBNI since it is shown the imidazole moiety does not influence the chelation properties of DFOB[163].

The relaxivity of a contrast agent is a well-known concept in studying contrast agents. Considering the Solomon–Bloembergen–Morgan (SBM) theory[55] one of the factors that affects the r_1 value of a chelating molecule is the number of inner sphere water molecules known as hydration (q). In a successful conjugation reaction it is assumed the primary amine group transforms to an amide group. The addition of the nitroimidazole moiety can influence the hydration of FOBNI, which is the dominant mechanism[57] in determining the longitudinal relaxivity of a contrast agent. The behavior of r_1 and r_2 in the direction of changes is usually the same meaning with the increase of the r_1 the r_2 also increases, or the decrease in r_1 is also followed by a decrease in r_2 values. This follows the simplified SBM equation that takes into account the hydration number. However, there are reports that do not follow this simplistic approach[164,165] and require more rigorous analysis and simulation. FOBNI shows about 75% decrease in r_1 value compare to FOB and about 65% increase in r_2 value. Generally, the MR contrast agents alter both T_1 and T_2 relaxation times. The extent to which a contrast agent is categorized as T_1 or T_2 (positive contrast or negative contrast) lies in the ratio of its transverse to longitudinal relaxivity[166]. The ratio $r_2/r_1 >> 1$ indicate a T_2 contrast agent while $r_2/r_1 < 1$ can imply a T_1 contrast agent[167]. However, as some endogenous factors and imaging artifacts result in negative contrast as well, the positive contrast is favorable in MR images and if a contrast agent is capable of producing strong T_1 contrast the discussion of the relaxivity ratio is overlooked. For example, GdDO3NI with a relaxivity ratio of 1.58 would generate a better contrast in T_2 images however with a longitudinal relaxivity r_1 of 4.75 $s^{-1}mmol^{-1}L$ it can furnish a strong positive contrast as shown in Gulaka et al. reports[2]. Here we report the relaxivity ratio of 8.84 for FOBNI with

longitudinal relaxivity of 0.51 $s^{-1}mmol^{-1}L$, which emphasizes its high performance to generate hypointense regions in T_2 weighted images.

The cell viability assay confirmed the cytocompatibility of the chelated DFOBNI up to 8h or direct exposure to the cells. The results are supported by previous studies characterizing similar derivatives of FOB for different purposes[168–170]. The body's immediate clearance response for the injected molecules[171] eliminates the contrast agent from the bloodstream culminating in no injected molecules in proximity to the normal cells for an extended period. This is ascribed to the functional blood circulatory system, eliminating the perfusion and diffusion-limited hypoxic regions in normal and healthy organs. It is reported the circulation half-time for DFOB is about 5 min in mouse[172]. On the other hand, the prolonged exposure of the contrast agent affected the cells' viability, which could be considered the auxiliary effect of the molecule. It can mainly provide spatial distribution maps of hypoxia in MR modality and serve as a toxic molecule for hypoxic cells due to the covalent bond of the nitroimidazole moiety and the thiol proteins and the continued exposure of the cells to the contrast agent. The cytotoxicity assay under normoxic and hypoxic conditions did not show any significant difference in the final result this could indicate the toxicity is just resulting from prolonged exposure to the contrast agent. The retention would happen when the contrast is chemically bond to the hypoxic regions in the organs.

DFOB has very low cell permeability; one approach to improve its permeability is modifying the molecule by adding chemical groups to the molecule that enhances the

cellular uptake. Pramanik et al. showed conjugation of DFOB and imidazole significantly improved the cell permeability compare to DFOB[173]. Our results also showed the addition of nitroimidazole moiety to DFOB increased the cellular uptake of FOBNI, which manifested itself in the T_2 values of the exposed cells to FOB (T_2=89.9±11.2 ms) and FOBNI (T_2=59.3±9.3 ms) under normoxic conditions. Using the relaxivity equation for transverse relaxation rate the pellet of normoxic FOB exposed cells shows contrast agent concentration of 2.67 mM and FOBNI exposed cells show 2.88 mM concentration of contrast, which lends credence to increased cell permeability of the contrast agent after the addition of nitroimidazole group. The most significant change in concentration of iron was obtained when cells experienced hypoxic conditions. The concentration for cells under the hypoxic conditions, which were exposed to FOB was 3.45 mM and for the cells exposed to FOBNI was 5.98 mM showing 1.73 fold increase under hypoxic condition. This increased uptake can be ascribed to improvement in cell permeability after addition of nitroimidazole moiety and more importantly can be an indication of the successful reduction and binding of nitroimidazole moiety in FOBNI to the thiol groups under hypoxic condition[174,175].

5. Conclusion

We developed a novel derivative of DFOB. We used DFOBNI to chelate iron ions and successfully studied its properties as a potential hypoxia targeting contrast agent. The relaxivity studies showed promising results for FOBNI (r_2=4.51 $s^{-1}mmol^{-1}L$) to be a T_2 weighted contrast agent. Cytotoxicity assay showed no significant changes in viability of

the cells exposed to FOBNI with concentrations up to 400 uM for 8 h. The in vitro studies showed the T_2 values of exposed cells under the hypoxic conditions significantly was reduced, which was attributed to the chemical reduction and binding of the nitroimidazole moiety on the molecule to thiol groups in the cell.

CHAPTER 5

CONCLUSIONS AND FUTURE DIRECTIONS

In the chapters 2 and 3 of this study, we extensively studied the performance of GdDO3NI as a T_1-based hypoxia targeting MRI contrast agent. Our results show GdDO3NI can successfully detect hypoxic regions in traumatic brain injury and brain tumors. A noninvasively generated hypoxia map for different pathologies in individuals is critical in developing personalized treatments, which results in the highest possible affectatious approaches with the least possible side effects. The importance of studying hypoxia requires novel methods to assess it. These methods are usually answering the drawbacks of the existing techniques. For example, noninvasive techniques are utilized to eliminate the invasive methods' complications, or novel noninvasive approaches are being employed to acquire more information from the tissue microenvironment, like improving spatial resolution. The performance of GdDO3NI in detecting hypoxia is promising. GdDO3NI has been successfully tested in subcutaneous prostate and lung tumors in our group, and in this study, we investigated its efficacy in TBI and brain tumors. The possible challenges in the TBI study regarding pharmacokinetic modeling can be listed as inadequate temporal resolution, inconsistent injection rate and the dynamic nature of the injury. The acquired images for TBI had a frequency of 10 min; however, the recommended temporal resolution for pharmacokinetic modeling is 5-10 seconds[176]. Another challenge in TBI study could be the inconsistence injection time of the contrast agent. The injections were performed manually, the manually injection could suffer nonrepeatable injection rates. In the TBI study the imaging took place immediately after the modeled injury. The dynamic nature of

the injury could affect the result of the hypoxia assessment. The primary assumption that GdDO3NI binding to thiol groups under hypoxic conditions is irreversible covalent bond, might influence the interpretation of the final results. The enhanced regions because of the Gd retention could be hypoxic in the beginning, but not hypoxic and still hyperintense at the end of the imaging period due to the dynamic changes in injured tissue microenvironment. GdDO3NI could be routinely used in the clinic upon receiving clinical trial approvals in detecting and mapping hypoxia. For example, it is reported the injured brain tissue in most TBI patients experience hypoxia; to detect hypoxia in these patients, doctors could use a shot of GdDO3NI and perform MRI on the patients' brain to detect the high-intensity regions in the brain tissue. Here we also developed and synthesized a novel iron-based contrast agent to detect hypoxia. The main incentive was to eliminate the Gd molecule from the body and use a biologically safe paramagnetic atom. FOBNI showed promising results in detecting hypoxia in cells exposed to the hypoxic condition. The 2D cell culture due to simplification of the cell environment completely eliminates the 3D interaction of the cells with each other and extracellular matrix (ECM). This simplification usually comes with the expense of nonpredictive responses for in vivo studies[177]. The common practice in drug discovery and drug test includes 2D cell culture experiments, ensued by in vivo studies and finally clinical trials. However, this approach in selecting the efficacious drug or molecule is not cost effective. Most failed projects happen in in vivo testing stage because of in vivo toxicity or ineffectiveness. In addition, animal testing is time consuming and a costly procedure. Cell spheroids could serve as simplified tumor models. To avoid squandering the resources, addition of a 3D tissue culture model before

in vivo studies would be a judicious step since it can serve as a confirmatory step in translating in vitro experiments to in vivo experiment. To give researchers confidence to use FOBNI to study hypoxia in the future, we would study it in 3D tissue culture models and if the results were satisfactory we would perform in vivo animal models. For example, a mouse brain tumor models used in chapter 3 could serve as the first step to assess the contrast agent's efficacy.

REFERENCES

1. Varia MA, Calkins-Adams DP, Rinker LH, et al. Pimonidazole: A Novel Hypoxia Marker for Complementary Study of Tumor Hypoxia and Cell Proliferation in Cervical Carcinoma. *Gynecol Oncol*. 1998;71(2):270-277. doi:10.1006/gyno.1998.5163

2. Gulaka PK, Rojas-Quijano F, Kovacs Z, Mason RP, Sherry AD, Kodibagkar VD. GdDO3NI , a nitroimidazole-based T1 MRI contrast agent for imaging tumor hypoxia in vivo. *JBIC J Biol Inorg Chem*. 2014;19(2):271-279. doi:10.1007/s00775-013-1058-5

3. Agarwal S, Kodibagkar VD, Inge LJ, et al. MRI Guided Analysis of Changes in Tumor Oxygenation in Response to Hypoxia Activated/Targeted Therapeutics. In: *ASU Electronic Theses and Dissertations*. Arizona State University; 2017. Accessed November 21, 2020. http://hdl.handle.net/2286/R.I.44236

4. Brábek J, Mierke CT, Rösel D, Veselý P, Fabry B. The role of the tissue microenvironment in the regulation of cancer cell motility and invasion. *Cell Commun Signal*. 2010;8(1):22. doi:10.1186/1478-811X-8-22

5. Kan EM, Ling E-A, Lu J. Microenvironment changes in mild traumatic brain injury. *Brain Res Bull*. 2012;87(4):359-372. doi:10.1016/j.brainresbull.2012.01.007

6. Papkovsky DB, Dmitriev RI. Biological detection by optical oxygen sensing. *Chem Soc Rev*. 2013;42(22):8700-8732. doi:10.1039/C3CS60131E

7. Michiels C. Physiological and Pathological Responses to Hypoxia. *Am J Pathol*. 2004;164(6):1875-1882. doi:10.1016/S0002-9440(10)63747-9

8. Anoxia - Abstract - Europe PMC. Accessed March 14, 2021. https://europepmc.org/article/nbk/nbk482316

9. Hanahan D, Weinberg RA. Hallmarks of Cancer: The Next Generation. *Cell*. 2011;144(5):646-674. doi:10.1016/j.cell.2011.02.013

10. Höckel M, Vaupel P. Tumor Hypoxia: Definitions and Current Clinical, Biologic, and Molecular Aspects. *JNCI J Natl Cancer Inst*. 2001;93(4):266-276. doi:10.1093/jnci/93.4.266

11. Tatum JL. Hypoxia: Importance in tumor biology, noninvasive measurement by imaging, and value of its measurement in the management of cancer therapy. *Int J Radiat Biol*. 2006;82(10):699-757. doi:10.1080/09553000601002324

12. Michiels C, Tellier C, Feron O. Cycling hypoxia: A key feature of the tumor microenvironment. *Biochim Biophys Acta BBA - Rev Cancer*. 2016;1866(1):76-86. doi:10.1016/j.bbcan.2016.06.004

13. Thomlinson RH, Gray LH. The Histological Structure of Some Human Lung Cancers and the Possible Implications for Radiotherapy. *Br J Cancer*. 1955;9(4):539-549. doi:10.1038/bjc.1955.55

14. Brown JM. Evidence for acutely hypoxic cells in mouse tumours, and a possible mechanism of reoxygenation. *Br J Radiol*. 1979;52(620):650-656. doi:10.1259/0007-1285-52-620-650

15. Vaupel P, Mayer A. Hypoxia in Tumors: Pathogenesis-Related Classification, Characterization of Hypoxia Subtypes, and Associated Biological and Clinical Implications. In: Swartz HM, Harrison DK, Bruley DF, eds. *Oxygen Transport to Tissue XXXVI*. Advances in Experimental Medicine and Biology. Springer; 2014:19-24. doi:10.1007/978-1-4939-0620-8_3

16. Yan EB, Satgunaseelan L, Paul E, et al. Post-Traumatic Hypoxia Is Associated with Prolonged Cerebral Cytokine Production, Higher Serum Biomarker Levels, and Poor Outcome in Patients with Severe Traumatic Brain Injury. *J Neurotrauma*. 2013;31(7):618-629. doi:10.1089/neu.2013.3087

17. Chesnut RM, Marshall SB, Piek J, Blunt BA, Klauber MR, Marshall LF. Early and Late Systemic Hypotension as a Frequent and Fundamental Source of Cerebral Ischemia Following Severe Brain Injury in the Traumatic Coma Data Bank. In: Unterberg AW, Schneider G-H, Lanksch WR, eds. *Monitoring of Cerebral Blood Flow and Metabolism in Intensive Care*. Acta Neurochirurgica. Springer; 1993:121-125. doi:10.1007/978-3-7091-9302-0_21

18. Jeremitsky E, Omert L, Dunham CM, Protetch J, Rodriguez A. Harbingers of Poor Outcome the Day after Severe Brain Injury: Hypothermia, Hypoxia, and Hypoperfusion. *J Trauma Acute Care Surg*. 2003;54(2):312-319. doi:10.1097/01.TA.0000037876.37236.D6

19. Mrozek S, Luzi A, Gonzalez L, Kerhuel L, Fourcade O, Geeraerts T. Cerebral and extracerebral vulnerability to hypoxic insults after diffuse traumatic brain injury in rats. *Brain Res*. 2016;1646:334-341. doi:10.1016/j.brainres.2016.06.007

20. Alves JL. Blood–brain barrier and traumatic brain injury. *J Neurosci Res*. 2014;92(2):141-147. doi:https://doi.org/10.1002/jnr.23300

21. Ishige N, Pitts LH, Berry I, et al. The Effect of Hypoxia on Traumatic Head Injury in Rats: Alterations in Neurologic Function, Brain Edema, and Cerebral Blood Flow. *J Cereb Blood Flow Metab*. 1987;7(6):759-767. doi:10.1038/jcbfm.1987.131

22. McDonald DM, Choyke PL. Imaging of angiogenesis: from microscope to clinic. *Nat Med*. 2003;9(6):713-725. doi:10.1038/nm0603-713

23. Konerding MA, Fait E, Gaumann A. 3D microvascular architecture of pre-cancerous lesions and invasive carcinomas of the colon. *Br J Cancer*. 2001;84(10):1354-1362. doi:10.1054/bjoc.2001.1809

24. Siemann DW, Horsman MR. Modulation of the tumor vasculature and oxygenation to improve therapy. *Pharmacol Ther*. 2015;153:107-124. doi:10.1016/j.pharmthera.2015.06.006

25. Krock BL, Skuli N, Simon MC. Hypoxia-Induced Angiogenesis. *Genes Cancer*. 2011;2(12):1117-1133. doi:10.1177/1947601911423654

26. Feng J, Zhao X, Gurkoff GG, Van KC, Shahlaie K, Lyeth BG. Post-traumatic hypoxia exacerbates neuronal cell death in the hippocampus. *J Neurotrauma*. 2012;29(6):1167-1179. doi:10.1089/neu.2011.1867

27. Feng J-F, Gurkoff GG, Van KC, et al. NAAG peptidase inhibitor reduces cellular damage in a model of TBI with secondary hypoxia. *Brain Res*. 2012;1469:144-152. doi:10.1016/j.brainres.2012.06.021

28. Moghadas B, Bharadwaj VN, Tobey JP, Tian Y, Stabenfeldt SE, Kodibagkar VD. GdDO3NI allows imaging of hypoxia after brain injury. *bioRxiv*. Published online March 17, 2021:2021.03.16.435723. doi:10.1101/2021.03.16.435723

29. Brahimi-Horn MC, Chiche J, Pouysségur J. Hypoxia and cancer. *J Mol Med*. 2007;85(12):1301-1307. doi:10.1007/s00109-007-0281-3

30. Ferdinand P, Roffe C. Hypoxia after stroke: a review of experimental and clinical evidence. *Exp Transl Stroke Med*. 2016;8(1):9. doi:10.1186/s13231-016-0023-0

31. Ruan K, Song G, Ouyang G. Role of hypoxia in the hallmarks of human cancer. *J Cell Biochem*. 2009;107(6):1053-1062. doi:https://doi.org/10.1002/jcb.22214

32. Petrova V, Annicchiarico-Petruzzelli M, Melino G, Amelio I. The hypoxic tumour microenvironment. *Oncogenesis*. 2018;7(1):1-13. doi:10.1038/s41389-017-0011-9

33. Noman MZ, Hasmim M, Messai Y, et al. Hypoxia: a key player in antitumor immune response. A review in the theme: cellular responses to hypoxia. *Am J Physiol-Cell Physiol*. 2015;309(9):C569-C579.

34. Finger EC, Giaccia AJ. Hypoxia, inflammation, and the tumor microenvironment in metastatic disease. *Cancer Metastasis Rev*. 2010;29(2):285-293. doi:10.1007/s10555-010-9224-5

35. Shannon AM, Bouchier-Hayes DJ, Condron CM, Toomey D. Tumour hypoxia, chemotherapeutic resistance and hypoxia-related therapies. *Cancer Treat Rev*. 2003;29(4):297-307. doi:10.1016/S0305-7372(03)00003-3

36. Wilson WR, Hay MP. Targeting hypoxia in cancer therapy. *Nat Rev Cancer*. 2011;11(6):393-410.

37. Muz B, Puente P de la, Azab F, Azab AK. The role of hypoxia in cancer progression, angiogenesis, metastasis, and resistance to therapy. *Hypoxia*. 2015;3:83-92. doi:10.2147/HP.S93413

38. Moulder JE, Rockwell S. Tumor hypoxia: its impact on cancer therapy. *Cancer Metastasis Rev*. 1987;5(4):313-341. doi:10.1007/BF00055376

39. Kizaka-Kondoh S, Inoue M, Harada H, Hiraoka M. Tumor hypoxia: A target for selective cancer therapy. *Cancer Sci*. 2003;94(12):1021-1028. doi:https://doi.org/10.1111/j.1349-7006.2003.tb01395.x

40. Vaupel P, Mayer A. Hypoxia in cancer: significance and impact on clinical outcome. *Cancer Metastasis Rev*. 2007;26(2):225-239. doi:10.1007/s10555-007-9055-1

41. Clark LC, Wolf R, Granger D, Taylor Z. Continuous Recording of Blood Oxygen Tensions by Polarography. *J Appl Physiol*. 1953;6(3):189-193. doi:10.1152/jappl.1953.6.3.189

42. Peterson JI, Fitzgerald RV, Buckhold DK. Fiber-optic probe for in vivo measurement of oxygen partial pressure. *Anal Chem*. 1984;56(1):62-67. doi:10.1021/ac00265a017

43. Aoyagi T. Pulse oximetry: its invention, theory, and future. *J Anesth*. 2003;17(4):259-266. doi:10.1007/s00540-003-0192-6

44. Kennedy AS, Raleigh JA, Perez GM, et al. Proliferation and hypoxia in human squamous cell carcinoma of the cervix: First report of combined immunohistochemical assays. *Int J Radiat Oncol Biol Phys*. 1997;37(4):897-905. doi:10.1016/S0360-3016(96)00539-1

45. Halpern HJ, Yu C, Peric M, Barth E, Grdina DJ, Teicher BA. Oxymetry deep in tissues with low-frequency electron paramagnetic resonance. *Proc Natl Acad Sci*. 1994;91(26):13047-13051. doi:10.1073/pnas.91.26.13047

46. Jerabek PA, Patrick TB, Kilbourn MR, Dischino DD, Welch MJ. Synthesis and biodistribution of 18F-labeled fluoronitroimidazoles: Potential in vivo markers of hypoxic tissue. *Int J Rad Appl Instrum [A]*. 1986;37(7):599-605. doi:10.1016/0883-2889(86)90079-1

47. Baudelet C, Gallez B. How does blood oxygen level-dependent (BOLD) contrast correlate with oxygen partial pressure (pO2) inside tumors? *Magn Reson Med*. 2002;48(6):980-986. doi:https://doi.org/10.1002/mrm.10318

48. Mason RP, Rodbumrung W, Antich PP. Hexafluorobenzene: a Sensitive 19F NMR Indicator of Tumor Oxygenation. *NMR Biomed*. 1996;9(3):125-134. doi:https://doi.org/10.1002/(SICI)1099-1492(199605)9:3<125::AID-NBM405>3.0.CO;2-F

49. Kodibagkar VD, Cui W, Merritt ME, Mason RP. Novel 1H NMR approach to quantitative tissue oximetry using hexamethyldisiloxane. *Magn Reson Med*. 2006;55(4):743-748. doi:https://doi.org/10.1002/mrm.20826

50. Raleigh JA, Miller GG, Franko AJ, Koch CJ, Fuciarelli AF, Kelly DA. Fluorescence immunohistochemical detection of hypoxic cells in spheroids and tumours. *Br J Cancer*. 1987;56(4):395-400. doi:10.1038/bjc.1987.213

51. Peeters SGJA, Zegers CML, Lieuwes NG, et al. A Comparative Study of the Hypoxia PET Tracers [18F]HX4, [18F]FAZA, and [18F]FMISO in a Preclinical Tumor Model. *Int J Radiat Oncol*. 2015;91(2):351-359. doi:10.1016/j.ijrobp.2014.09.045

52. Takasawa Masashi, Moustafa Ramez Reda, Baron Jean-Claude. Applications of Nitroimidazole In Vivo Hypoxia Imaging in Ischemic Stroke. *Stroke*. 2008;39(5):1629-1637. doi:10.1161/STROKEAHA.107.485938

53. Jacques V, Dumas S, Sun W-C, Troughton JS, Greenfield MT, Caravan P. High relaxivity MRI contrast agents part 2: Optimization of inner- and second-sphere relaxivity. *Invest Radiol*. 2010;45(10):613-624. doi:10.1097/RLI.0b013e3181ee6a49

54. Dumas S, Jacques V, Sun W-C, et al. High Relaxivity Magnetic Resonance Imaging Contrast Agents Part 1: Impact of Single Donor Atom Substitution on Relaxivity of Serum Albumin-Bound Gadolinium Complexes. *Invest Radiol*. 2010;45(10):600-612. doi:10.1097/RLI.0b013e3181ee5a9e

55. Caravan P, Farrar CT, Frullano L, Uppal R. Influence of molecular parameters and increasing magnetic field strength on relaxivity of gadolinium- and manganese-based T1 contrast agents. *Contrast Media Mol Imaging*. 2009;4(2):89-100. doi:10.1002/cmmi.267

56. Tóth É, Helm L, Merbach AE. Relaxivity of MRI Contrast Agents. In: Krause W, ed. *Contrast Agents I: Magnetic Resonance Imaging*. Topics in Current Chemistry. Springer; 2002:61-101. doi:10.1007/3-540-45733-X_3

57. Jacques V, Dumas S, Sun W-C, Troughton JS, Greenfield MT, Caravan P. High-relaxivity magnetic resonance imaging contrast agents. Part 2. Optimization of inner- and second-sphere relaxivity. *Invest Radiol*. 2010;45(10):613-624. doi:10.1097/RLI.0b013e3181ee6a49

58. Dumas S, Jacques V, Sun W-C, et al. High Relaxivity Magnetic Resonance Imaging Contrast Agents Part 1: Impact of Single Donor Atom Substitution on Relaxivity of Serum Albumin-Bound Gadolinium Complexes. *Invest Radiol*. 2010;45(10):600-612. doi:10.1097/RLI.0b013e3181ee5a9e

59. Freed JH. Dynamic effects of pair correlation functions on spin relaxation by translational diffusion in liquids. II. Finite jumps and independent T1 processes. *J Chem Phys*. 1978;68(9):4034-4037. doi:10.1063/1.436302

60. Tang J, Sheng Y, Hu H, Shen Y. Macromolecular MRI contrast agents: Structures, properties and applications. *Prog Polym Sci*. 2013;38(3):462-502. doi:10.1016/j.progpolymsci.2012.07.001

61. Rojas-Quijano FA, Tircsó G, Tircsóné Benyó E, et al. Synthesis and Characterization of a Hypoxia-Sensitive MRI Probe. *Chem – Eur J*. 2012;18(31):9669-9676. doi:https://doi.org/10.1002/chem.201200266

62. Ye F, Jeong E-K, Jia Z, Yang T, Parker D, Lu Z-R. A Peptide Targeted Contrast Agent Specific to Fibrin-Fibronectin Complexes for Cancer Molecular Imaging with MRI. *Bioconjug Chem*. 2008;19(12):2300-2303. doi:10.1021/bc800211r

63. Pais A, Gunanathan C, Margalit R, et al. In Vivo Magnetic Resonance Imaging of the Estrogen Receptor in an Orthotopic Model of Human Breast Cancer. *Cancer Res*. 2011;71(24):7387-7397. doi:10.1158/0008-5472.CAN-11-1226

64. McIntosh, Saatman, Raghupathi, et al. gThe Dorothy Russell Memorial Lecture* The molecular and cellular sequelae of experimental traumatic brain injury: pathogenetic mechanisms. *Neuropathol Appl Neurobiol*. 1998;24(4):251-267. doi:https://doi.org/10.1046/j.1365-2990.1998.00121.x

65. Langlois JA, Rutland-Brown W, Wald MM. The Epidemiology and Impact of Traumatic Brain Injury: A Brief Overview. *J Head Trauma Rehabil*. 2006;21(5):375-378.

66. Chi JH, Knudson MM, Vassar MJ, et al. Prehospital Hypoxia Affects Outcome in Patients With Traumatic Brain Injury: A Prospective Multicenter Study. *J Trauma Acute Care Surg*. 2006;61(5):1134-1141. doi:10.1097/01.ta.0000196644.64653.d8

67. Flanagan SR. Invited Commentary on “Centers for Disease Control and Prevention Report to Congress: Traumatic Brain Injury in the United States: Epidemiology

and Rehabilitation." *Arch Phys Med Rehabil*. 2015;96(10):1753-1755. doi:10.1016/j.apmr.2015.07.001

68. Bryant RA, O'Donnell ML, Creamer M, McFarlane AC, Clark CR, Silove D. The psychiatric sequelae of traumatic injury. *Am J Psychiatry*. 2010;167(3):312-320. doi:10.1176/appi.ajp.2009.09050617

69. Emery DL, Royo NC, Fischer I, Saatman KE, McIntosh TK. Plasticity following injury to the adult central nervous system: is recapitulation of a developmental state worth promoting? *J Neurotrauma*. 2003;20(12):1271-1292. doi:10.1089/089771503322686085

70. Masel BE, DeWitt DS. Traumatic brain injury: a disease process, not an event. *J Neurotrauma*. 2010;27(8):1529-1540. doi:10.1089/neu.2010.1358

71. Simon DW, McGeachy MJ, Bayır H, Clark RSB, Loane DJ, Kochanek PM. The far-reaching scope of neuroinflammation after traumatic brain injury. *Nat Rev Neurol*. 2017;13(3):171-191. doi:10.1038/nrneurol.2017.13

72. Spiotta AM, Stiefel MF, Gracias VH, et al. Brain tissue oxygen-directed management and outcome in patients with severe traumatic brain injury. *J Neurosurg*. 2010;113(3):571-580. doi:10.3171/2010.1.JNS09506

73. Sinha RP, Ducker TB, Perot PL. Arterial oxygenation. Findings and its significance in central nervous system trauma patients. *JAMA*. 1973;224(9):1258-1260. doi:10.1001/jama.224.9.1258

74. Oddo M, Levine JM, Mackenzie L, et al. Brain Hypoxia Is Associated With Short-term Outcome After Severe Traumatic Brain Injury Independently of Intracranial Hypertension and Low Cerebral Perfusion Pressure. *Neurosurgery*. 2011;69(5):1037-1045. doi:10.1227/NEU.0b013e3182287ca7

75. Bardt TF, Unterberg AW, Härtl R, Kiening KL, Schneider GH, Lanksch WR. Monitoring of brain tissue PO2 in traumatic brain injury: effect of cerebral hypoxia on outcome. *Acta Neurochir Suppl*. 1998;71:153-156. doi:10.1007/978-3-7091-6475-4_45

76. Yan EB, Satgunaseelan L, Paul E, et al. Post-traumatic hypoxia is associated with prolonged cerebral cytokine production, higher serum biomarker levels, and poor outcome in patients with severe traumatic brain injury. *J Neurotrauma*. 2014;31(7):618-629. doi:10.1089/neu.2013.3087

77. Eltzschig HK, Carmeliet P. Hypoxia and Inflammation. *N Engl J Med*. 2011;364(7):656-665. doi:10.1056/NEJMra0910283

78. Prakash R, Carmichael ST. Blood-brain barrier breakdown and neovascularization processes after stroke and traumatic brain injury. *Curr Opin Neurol*. 2015;28(6):556-564. doi:10.1097/WCO.0000000000000248

79. Stiefel MF, Spiotta A, Gracias VH, et al. Reduced mortality rate in patients with severe traumatic brain injury treated with brain tissue oxygen monitoring. *J Neurosurg*. 2005;103(5):805-811. doi:10.3171/jns.2005.103.5.0805

80. Aribisala BS, Cowie CJA, He J, et al. Multi-parametric Classification of Traumatic Brain Injury Patients Using Automatic Analysis of Quantitative MRI Scans. In: Liao H, Edwards PJ "Eddie," Pan X, Fan Y, Yang G-Z, eds. *Medical Imaging and Augmented Reality*. Lecture Notes in Computer Science. Springer; 2010:51-59. doi:10.1007/978-3-642-15699-1_6

81. Galloway NR, Tong KA, Ashwal S, Oyoyo U, Obenaus A. Diffusion-weighted imaging improves outcome prediction in pediatric traumatic brain injury. *J Neurotrauma*. 2008;25(10):1153-1162. doi:10.1089/neu.2007.0494

82. Mayer AR, Ling J, Mannell MV, et al. A prospective diffusion tensor imaging study in mild traumatic brain injury. *Neurology*. 2010;74(8):643-650. doi:10.1212/WNL.0b013e3181d0ccdd

83. Lee B, Newberg A. Neuroimaging in traumatic brain imaging. *NeuroRx J Am Soc Exp Neurother*. 2005;2(2):372-383. doi:10.1602/neurorx.2.2.372

84. Lindsey HM, Wilde EA, Caeyenberghs K, Dennis EL. Longitudinal Neuroimaging in Pediatric Traumatic Brain Injury: Current State and Consideration of Factors That Influence Recovery. *Front Neurol*. 2019;10. doi:10.3389/fneur.2019.01296

85. Raleigh null, Dewhirst null, Thrall null. Measuring Tumor Hypoxia. *Semin Radiat Oncol*. 1996;6(1):37-45. doi:10.1053/SRAO0060037

86. Zhao D, Jiang L, Mason RP. Measuring changes in tumor oxygenation. *Methods Enzymol*. 2004;386:378-418. doi:10.1016/S0076-6879(04)86018-X

87. Piert M, Machulla H-J, Picchio M, et al. Hypoxia-specific tumor imaging with 18F-fluoroazomycin arabinoside. *J Nucl Med Off Publ Soc Nucl Med*. 2005;46(1):106-113.

88. Evans SM, Kachur AV, Shiue CY, et al. Noninvasive detection of tumor hypoxia using the 2-nitroimidazole [18F]EF1. *J Nucl Med Off Publ Soc Nucl Med*. 2000;41(2):327-336.

89. Yang DJ, Wallace S, Cherif A, et al. Development of F-18-labeled fluoroerythronitroimidazole as a PET agent for imaging tumor hypoxia. *Radiology*. 1995;194(3):795-800. doi:10.1148/radiology.194.3.7862981

90. Krohn KA, Link JM, Mason RP. Molecular imaging of hypoxia. *J Nucl Med Off Publ Soc Nucl Med*. 2008;49 Suppl 2:129S-48S. doi:10.2967/jnumed.107.045914

91. Zhou H, Chiguru S, Hallac RR, et al. Examining correlations of oxygen sensitive MRI (BOLD/TOLD) with [18F]FMISO PET in rat prostate tumors. *Am J Nucl Med Mol Imaging*. 2019;9(2):156-167.

92. Hallac RR, Zhou H, Pidikiti R, et al. Correlations of noninvasive BOLD and TOLD MRI with pO2 and relevance to tumor radiation response. *Magn Reson Med*. 2014;71(5):1863-1873. doi:10.1002/mrm.24846

93. Ding Y, Mason RP, McColl RW, et al. Simultaneous measurement of tissue oxygen level-dependent (TOLD) and blood oxygenation level-dependent (BOLD) effects in abdominal tissue oxygenation level studies. *J Magn Reson Imaging JMRI*. 2013;38(5):1230-1236. doi:10.1002/jmri.24006

94. Procissi D, Claus F, Burgman P, et al. In vivo 19F magnetic resonance spectroscopy and chemical shift imaging of tri-fluoro-nitroimidazole as a potential hypoxia reporter in solid tumors. *Clin Cancer Res Off J Am Assoc Cancer Res*. 2007;13(12):3738-3747. doi:10.1158/1078-0432.CCR-06-1563

95. Chapman JD. Measurement of tumor hypoxia by invasive and non-invasive procedures: a review of recent clinical studies. *Radiother Oncol J Eur Soc Ther Radiol Oncol*. 1991;20 Suppl 1:13-19. doi:10.1016/0167-8140(91)90181-f

96. Gulaka PK, Rastogi U, McKay MA, Wang X, Mason RP, Kodibagkar VD. Hexamethyldisiloxane-based nanoprobes for (1) H MRI oximetry. *NMR Biomed*. 2011;24(10):1226-1234. doi:10.1002/nbm.1678

97. Kodibagkar VD, Wang X, Pacheco-Torres J, Gulaka P, Mason RP. Proton imaging of siloxanes to map tissue oxygenation levels (PISTOL): a tool for quantitative tissue oximetry. *NMR Biomed*. 2008;21(8):899-907. doi:10.1002/nbm.1279

98. Smith DH, Soares HD, Pierce JS, et al. A model of parasagittal controlled cortical impact in the mouse: cognitive and histopathologic effects. *J Neurotrauma*. 1995;12(2):169-178. doi:10.1089/neu.1995.12.169

99. Dixon CE, Clifton GL, Lighthall JW, Yaghmai AA, Hayes RL. A controlled cortical impact model of traumatic brain injury in the rat. *J Neurosci Methods*. 1991;39(3):253-262. doi:10.1016/0165-0270(91)90104-8

100. Osier ND, Dixon CE. The Controlled Cortical Impact Model: Applications, Considerations for Researchers, and Future Directions. *Front Neurol*. 2016;7. doi:10.3389/fneur.2016.00134

101. Jonkers BW, Sterk JC, Wouterlood FG. Transcardial perfusion fixation of the CNS by means of a compressed-air-driven device. *J Neurosci Methods*. 1984;12(2):141-149. doi:10.1016/0165-0270(84)90013-x

102. Li W, Long JA, Watts LT, et al. A quantitative MRI method for imaging blood-brain barrier leakage in experimental traumatic brain injury. *PloS One*. 2014;9(12):e114173. doi:10.1371/journal.pone.0114173

103. Kording F, Weidensteiner C, Zwick S, et al. Simultaneous assessment of vessel size index, relative blood volume, and vessel permeability in a mouse brain tumor model using a combined spin echo gradient echo echo-planar imaging sequence and viable tumor analysis. *J Magn Reson Imaging JMRI*. 2014;40(6):1310-1318. doi:10.1002/jmri.24513

104. Shlosberg D, Benifla M, Kaufer D, Friedman A. Blood-brain barrier breakdown as a therapeutic target in traumatic brain injury. *Nat Rev Neurol*. 2010;6(7):393-403. doi:10.1038/nrneurol.2010.74

105. Kallehauge JF, Tanderup K, Duan C, et al. Tracer kinetic model selection for dynamic contrast-enhanced magnetic resonance imaging of locally advanced cervical cancer. *Acta Oncol Stockh Swed*. 2014;53(8):1064-1072. doi:10.3109/0284186X.2014.937879

106. Bharadwaj VN, Lifshitz J, Adelson PD, Kodibagkar VD, Stabenfeldt SE. Temporal assessment of nanoparticle accumulation after experimental brain injury: Effect of particle size. *Sci Rep*. 2016;6(1):29988. doi:10.1038/srep29988

107. Klatzmann D, Valéry CA, Bensimon G, et al. A phase I/II study of herpes simplex virus type 1 thymidine kinase “suicide” gene therapy for recurrent glioblastoma. Study Group on Gene Therapy for Glioblastoma. *Hum Gene Ther*. 1998;9(17):2595-2604. doi:10.1089/hum.1998.9.17-2595

108. Pistollato F, Abbadi S, Rampazzo E, et al. Intratumoral hypoxic gradient drives stem cells distribution and MGMT expression in glioblastoma. *Stem Cells Dayt Ohio*. 2010;28(5):851-862. doi:10.1002/stem.415

109. Stokes AM, Hart CP, Quarles CC. Hypoxia Imaging With PET Correlates With Antitumor Activity of the Hypoxia-Activated Prodrug Evofosfamide (TH-302) in Rodent Glioma Models. *Tomography*. 2016;2(3):229-237. doi:10.18383/j.tom.2016.00259

110. Amberger-Murphy V. Hypoxia helps glioma to fight therapy. *Curr Cancer Drug Targets*. 2009;9(3):381-390. doi:10.2174/156800909788166637

111. Rasey JS, Grunbaum Z, Magee S, et al. Characterization of radiolabeled fluoromisonidazole as a probe for hypoxic cells. *Radiat Res*. 1987;111(2):292-304.

112. Rajendran JG, Wilson DC, Conrad EU, et al. [(18)F]FMISO and [(18)F]FDG PET imaging in soft tissue sarcomas: correlation of hypoxia, metabolism and VEGF expression. *Eur J Nucl Med Mol Imaging*. 2003;30(5):695-704. doi:10.1007/s00259-002-1096-7

113. Rajendran JG, Mankoff DA, O'Sullivan F, et al. Hypoxia and Glucose Metabolism in Malignant Tumors: Evaluation by [18F]Fluoromisonidazole and [18F]Fluorodeoxyglucose Positron Emission Tomography Imaging. *Clin Cancer Res*. 2004;10(7):2245-2252. doi:10.1158/1078-0432.CCR-0688-3

114. Kumar P, Stypinski D, Xia H, McEwan AJB, Machulla H-J, Wiebe LI. Fluoroazomycin arabinoside (FAZA): synthesis, 2H and 3H-labelling and preliminary biological evaluation of a novel 2-nitroimidazole marker of tissue hypoxia. *J Label Compd Radiopharm*. 1999;42(1):3-16. doi:https://doi.org/10.1002/(SICI)1099-1344(199901)42:1<3::AID-JLCR160>3.0.CO;2-H

115. Yankeelov TE, Luci JJ, Lepage M, et al. Quantitative pharmacokinetic analysis of DCE-MRI data without an arterial input function: a reference region model. *Magn Reson Imaging*. 2005;23(4):519-529. doi:10.1016/j.mri.2005.02.013

116. Tofts PS, Brix G, Buckley DL, et al. Estimating kinetic parameters from dynamic contrast-enhanced T(1)-weighted MRI of a diffusable tracer: standardized quantities and symbols. *J Magn Reson Imaging JMRI*. 1999;10(3):223-232. doi:10.1002/(sici)1522-2586(199909)10:3<223::aid-jmri2>3.0.co;2-s

117. Daldrup-Link HE, Rydland J, Helbich TH, et al. Quantification of breast tumor microvascular permeability with feruglose-enhanced MR imaging: initial phase II multicenter trial. *Radiology*. 2003;229(3):885-892. doi:10.1148/radiol.2293021045

118. Leach MO, Brindle KM, Evelhoch JL, et al. The assessment of antiangiogenic and antivascular therapies in early-stage clinical trials using magnetic resonance imaging: issues and recommendations. *Br J Cancer*. 2005;92(9):1599-1610. doi:10.1038/sj.bjc.6602550

119. Faranesh AZ, Yankeelov TE. Incorporating a vascular term into a reference region model for the analysis of DCE-MRI data: a simulation study. *Phys Med Biol*. 2008;53(10):2617-2631. doi:10.1088/0031-9155/53/10/012

120. Bruehlmeier M, Roelcke U, Schubiger PA, Ametamey SM. Assessment of hypoxia and perfusion in human brain tumors using PET with 18F-fluoromisonidazole and 15O-H2O. *J Nucl Med Off Publ Soc Nucl Med*. 2004;45(11):1851-1859.

121. Scarpelli ML, Healey DR, Fuentes A, Kodibagkar VD, Quarles CC. Correlation of Tumor Hypoxia Metrics Derived from 18F-Fluoromisonidazole Positron Emission Tomography and Pimonidazole Fluorescence Images of Optically Cleared Brain

Tissue. *Tomogr Ann Arbor Mich*. 2020;6(4):379-388. doi:10.18383/j.tom.2020.00046

122. Susaki EA, Tainaka K, Perrin D, Yukinaga H, Kuno A, Ueda HR. Advanced CUBIC protocols for whole-brain and whole-body clearing and imaging. *Nat Protoc*. 2015;10(11):1709-1727. doi:10.1038/nprot.2015.085

123. van den Hoff J. Principles of quantitative positron emission tomography. *Amino Acids*. 2005;29(4):341-353. doi:10.1007/s00726-005-0215-8

124. Murase K. Efficient method for calculating kinetic parameters using T1-weighted dynamic contrast-enhanced magnetic resonance imaging. *Magn Reson Med*. 2004;51(4):858-862. doi:10.1002/mrm.20022

125. Kuwatsuru R, Shames DM, Mühler A, et al. Quantification of tissue plasma volume in the rat by contrast-enhanced magnetic resonance imaging. *Magn Reson Med*. 1993;30(1):76-81. doi:10.1002/mrm.1910300112

126. Principles of Magnetic Resonance Imaging: A Signal Processing Perspective | IEEE eBooks | IEEE Xplore. Accessed April 2, 2021. https://ieeexplore.ieee.org/book/5264284

127. Nelson TR, Tung SM. Temperature dependence of proton relaxation times in vitro. *Magn Reson Imaging*. 1987;5(3):189-199. doi:10.1016/0730-725x(87)90020-8

128. Birkl C, Langkammer C, Haybaeck J, et al. Temperature Dependency of T1 Relaxation Time in Unfixed and Fixed Human Brain Tissue. *Biomed Tech (Berl)*. 2013;58 Suppl 1. doi:10.1515/bmt-2013-4290

129. Giakoumettis D, Kritis A, Foroglou N. C6 cell line: the gold standard in glioma research. *Hippokratia*. 2018;22(3):105-112.

130. Höckel M, Vaupel P. Tumor Hypoxia: Definitions and Current Clinical, Biologic, and Molecular Aspects. *JNCI J Natl Cancer Inst*. 2001;93(4):266-276. doi:10.1093/jnci/93.4.266

131. Pennacchietti S, Michieli P, Galluzzo M, Mazzone M, Giordano S, Comoglio PM. Hypoxia promotes invasive growth by transcriptional activation of the met protooncogene. *Cancer Cell*. 2003;3(4):347-361. doi:10.1016/S1535-6108(03)00085-0

132. Hypoxic control of metastasis | Science. Accessed November 19, 2020. https://science.sciencemag.org/content/352/6282/175.abstract

133. Bonnitcha PD, Bayly SR, Theobald MB, Betts HM, Lewis JS, Dilworth JR. Nitroimidazole conjugates of bis (thiosemicarbazonato) 64Cu (II)–Potential

combination agents for the PET imaging of hypoxia. *J Inorg Biochem*. 2010;104(2):126-135.

134. Hypoxia-Inducible Factor-1 (HIF-1) | Molecular Pharmacology. Accessed November 20, 2020. https://molpharm.aspetjournals.org/content/70/5/1469

135. Endogenous Markers of Tumor Hypoxia | SpringerLink. Accessed November 20, 2020. https://link.springer.com/article/10.1007/s00066-003-1150-9

136. ERO1α is a novel endogenous marker of hypoxia in human cancer cell lines | BMC Cancer | Full Text. Accessed November 20, 2020. https://bmccancer.biomedcentral.com/articles/10.1186/s12885-019-5727-9

137. Kizaka-Kondoh S, Konse-Nagasawa H. Significance of nitroimidazole compounds and hypoxia-inducible factor-1 for imaging tumor hypoxia. *Cancer Sci*. 2009;100(8):1366-1373.

138. Arteel GE, Thurman RG, Yates JM, Raleigh JA. Evidence that hypoxia markers detect oxygen gradients in liver: pimonidazole and retrograde perfusion of rat liver. *Br J Cancer*. 1995;72(4):889-895. doi:10.1038/bjc.1995.429

139. Cobb LM, Nolan J, Butler SA. Distribution of pimonidazole and RSU 1069 in tumour and normal tissues. *Br J Cancer*. 1990;62(6):915-918. doi:10.1038/bjc.1990.408

140. Kim IH, Lemmon MJ, Brown JM. The Influence of Irradiation of the Tumor Bed on Tumor Hypoxia: Measurements by Radiation Response, Oxygen Electrodes, and Nitroimidazole Binding. *Radiat Res*. 1993;135(3):411-417. doi:10.2307/3578883

141. Dhani NC, Serra S, Pintilie M, et al. Analysis of the intra- and intertumoral heterogeneity of hypoxia in pancreatic cancer patients receiving the nitroimidazole tracer pimonidazole. *Br J Cancer*. 2015;113(6):864-871. doi:10.1038/bjc.2015.284

142. Gross MW, Karbach U, Groebe K, Franko AJ, Mueller-Klieser W. Calibration of misonidazole labeling by simultaneous measurement of oxygen tension and labeling density in multicellular spheroids. *Int J Cancer*. 1995;61(4):567-573.

143. Li Z, Li X, Gao X, Zhang Y, Shi W, Ma H. Nitroreductase detection and hypoxic tumor cell imaging by a designed sensitive and selective fluorescent probe, 7-[(5-nitrofuran-2-yl) methoxy]-3 H-phenoxazin-3-one. *Anal Chem*. 2013;85(8):3926-3932.

144. Wiebe LI. Radiohalogenated Nitroimidazoles for Single-photon Scintigraphic Imaging of Hypoxic Tissues. In: Machulla H-J, ed. *Imaging of Hypoxia: Tracer*

Developments. Developments in Nuclear Medicine. Springer Netherlands; 1999:155-176. doi:10.1007/978-94-017-1828-8_9

145. Raleigh JA, Franko AJ, Treiber EO, Lun JA, Allen PS. Covalent binding of a fluorinated 2-nitroimidazole to emt-6 tumors in Balb/C mice: detection by f-19 nuclear magnetic resonance at 2.35 T. *Int J Radiat Oncol Biol Phys*. 1986;12(7):1243-1245. doi:10.1016/0360-3016(86)90268-3

146. Rasey JS, Koh W-J, Grierson JR, Grunbaum Z, Krohn KA. Radiolabeled fluoromisonidazole as an imaging agent for tumor hypoxia. *Int J Radiat Oncol Biol Phys*. 1989;17(5):985-991. doi:10.1016/0360-3016(89)90146-6

147. Bérubé LR, Harasiewicz K, Foster FS, Dobrowsky E, Sherar MD, Rauth AM. Use of a high frequency ultrasound microscope to image the action of 2-nitroimidazoles in multicellular spheroids. *Br J Cancer*. 1992;65(5):633-640. doi:10.1038/bjc.1992.137

148. Okuda K, Okabe Y, Kadonosono T, et al. 2-Nitroimidazole-Tricarbocyanine Conjugate as a Near-Infrared Fluorescent Probe for in Vivo Imaging of Tumor Hypoxia. *Bioconjug Chem*. 2012;23(3):324-329. doi:10.1021/bc2004704

149. Mahy P, De Bast M, Gallez B, et al. In vivo colocalization of 2-nitroimidazole EF5 fluorescence intensity and electron paramagnetic resonance oximetry in mouse tumors. *Radiother Oncol*. 2003;67(1):53-61. doi:10.1016/S0167-8140(03)00028-8

150. Helm PA, Caravan P, French BA, et al. Postinfarction Myocardial Scarring in Mice: Molecular MR Imaging with Use of a Collagen-targeting Contrast Agent. *Radiology*. 2008;247(3):788-796. doi:10.1148/radiol.2473070975

151. Zhou Z, Qutaish M, Han Z, et al. MRI detection of breast cancer micrometastases with a fibronectin-targeting contrast agent. *Nat Commun*. 2015;6(1):7984. doi:10.1038/ncomms8984

152. Rogosnitzky M, Branch S. Gadolinium-based contrast agent toxicity: a review of known and proposed mechanisms. *BioMetals*. 2016;29(3):365-376. doi:10.1007/s10534-016-9931-7

153. Abbaspour N, Hurrell R, Kelishadi R. Review on iron and its importance for human health. *J Res Med Sci Off J Isfahan Univ Med Sci*. 2014;19(2):164-174.

154. Codd R, Richardson-Sanchez T, Telfer TJ, Gotsbacher MP. Advances in the Chemical Biology of Desferrioxamine B. *ACS Chem Biol*. 2018;13(1):11-25. doi:10.1021/acschembio.7b00851

155. Modell B, Khan M, Darlison M. Survival in beta-thalassaemia major in the UK: data from the UK Thalassaemia Register. *Lancet Lond Engl*. 2000;355(9220):2051-2052. doi:10.1016/S0140-6736(00)02357-6

156. Olivieri NF, Brittenham GM. Iron-Chelating Therapy and the Treatment of Thalassemia. *Blood*. 1997;89(3):739-761. doi:10.1182/blood.V89.3.739

157. Would decreased aluminum ingestion reduce the incidence of Alzheimer's disease? Accessed November 22, 2020. https://www.ncbi.nlm.nih.gov/pmc/articles/PMC1335899/

158. Antineuroblastoma Activity of Desferoxamine in Human Cell Lines | Cancer Research. Accessed November 22, 2020. https://cancerres.aacrjournals.org/content/47/7/1749.short

159. Cell Penetrating Peptide (CPP)-Conjugated Desferrioxamine for Enhanced Neuroprotection: Synthesis and in Vitro Evaluation | Bioconjugate Chemistry. Accessed November 22, 2020. https://pubs.acs.org/doi/abs/10.1021/bc5004197

160. Characterization of the Sol−Gel Formation of Iron(III) Oxide/Hydroxide Nanonetworks from Weak Base Molecules | Chemistry of Materials. Accessed March 3, 2021. https://pubs.acs.org/doi/abs/10.1021/cm0609101

161. Kumar P, Nagarajan A, Uchil PD. Analysis of Cell Viability by the alamarBlue Assay. *Cold Spring Harb Protoc*. 2018;2018(6):pdb.prot095489. doi:10.1101/pdb.prot095489

162. Bower DV, Richter JK, von Tengg-Kobligk H, Heverhagen JT, Runge VM. Gadolinium-Based MRI Contrast Agents Induce Mitochondrial Toxicity and Cell Death in Human Neurons, and Toxicity Increases With Reduced Kinetic Stability of the Agent. *Invest Radiol*. 2019;54(8):453-463. doi:10.1097/RLI.0000000000000567

163. Cell Permeable Imidazole-Desferrioxamine Conjugates: Synthesis and In Vitro Evaluation | Bioconjugate Chemistry. Accessed December 7, 2020. https://pubs.acs.org/doi/10.1021/acs.bioconjchem.8b00924

164. Jahanbin T, Sauriat-Dorizon H, Spearman P, Benderbous S, Korri-Youssoufi H. Development of Gd(III) porphyrin-conjugated chitosan nanoparticles as contrast agents for magnetic resonance imaging. *Mater Sci Eng C*. 2015;52:325-332. doi:10.1016/j.msec.2015.03.007

165. Nguyen HV-T, Chen Q, Paletta JT, et al. Nitroxide-Based Macromolecular Contrast Agents with Unprecedented Transverse Relaxivity and Stability for Magnetic Resonance Imaging of Tumors. *ACS Cent Sci*. 2017;3(7):800-811. doi:10.1021/acscentsci.7b00253

166. Zairov R, Khakimullina G, Podyachev S, et al. Hydration number: crucial role in nuclear magnetic relaxivity of Gd(III) chelate-based nanoparticles. *Sci Rep*. 2017;7(1):14010. doi:10.1038/s41598-017-14409-6

167. Estelrich J, Sánchez-Martín MJ, Busquets MA. Nanoparticles in magnetic resonance imaging: from simple to dual contrast agents. International Journal of Nanomedicine. Published March 6, 2015. Accessed December 7, 2020. https://www.dovepress.com/nanoparticles-in-magnetic-resonance-imaging-from-simple-to-dual-contra-peer-reviewed-article-IJN

168. Becton DL, Bryles P. Deferoxamine Inhibition of Human Neuroblastoma Viability and Proliferation. *Cancer Res*. 1988;48(24 Part 1):7189-7192.

169. Xu J, Sun T, Zhong R, You C, Tian M. PEGylation of Deferoxamine for Improving the Stability, Cytotoxicity, and Iron-Overload in an Experimental Stroke Model in Rats. *Front Bioeng Biotechnol*. 2020;8. doi:10.3389/fbioe.2020.592294

170. Yu B, Yang Y, Liu Q, Zhan A, Yang Y, Liu H. A Novel Star Like Eight-Arm Polyethylene Glycol-Deferoxamine Conjugate for Iron Overload Therapy. *Pharmaceutics*. 2020;12(4):329. doi:10.3390/pharmaceutics12040329

171. Muetterties KA, Hoener B-A, Engelstad BL, et al. Ferrioxamine B derivatives as hepatobiliary contrast agents for magnetic resonance imaging. *Magn Reson Med*. 1991;22(1):88-100. doi:https://doi.org/10.1002/mrm.1910220110

172. Imran ul-haq M, Hamilton JL, Lai BFL, et al. Design of Long Circulating Nontoxic Dendritic Polymers for the Removal of Iron in Vivo. *ACS Nano*. 2013;7(12):10704-10716. doi:10.1021/nn4035074

173. Pramanik S, Chakraborty S, Sivan M, Patro BS, Chatterjee S, Goswami D. Cell Permeable Imidazole-Desferrioxamine Conjugates: Synthesis and In Vitro Evaluation. *Bioconjug Chem*. 2019;30(3):841-852. doi:10.1021/acs.bioconjchem.8b00924

174. Lord EM, Harwell L, Koch CJ. Detection of Hypoxic Cells by Monoclonal Antibody Recognizing 2-Nitroimidazole Adducts. *Cancer Res*. 1993;53(23):5721-5726.

175. Brown JM. The mechanisms of cytotoxicity and chemosensitization by misonidazole and other nitroimidazoles. *Int J Radiat Oncol*. 1982;8(3):675-682. doi:10.1016/0360-3016(82)90711-8

176. Winfield JM, Payne GS, Weller A, deSouza NM. DCE-MRI, DW-MRI, and MRS in Cancer: Challenges and Advantages of Implementing Qualitative and

Quantitative Multi-parametric Imaging in the Clinic. *Top Magn Reson Imaging*. 2016;25(5):245-254. doi:10.1097/RMR.0000000000000103

177. Langhans SA. Three-Dimensional in Vitro Cell Culture Models in Drug Discovery and Drug Repositioning. *Front Pharmacol*. 2018;9. doi:10.3389/fphar.2018.00006

APPENDIX A

GDDO3NI ALLOWS IMAGING OF HYPOXIA AFTER BRAIN INJURY

Submitted to Journal of Magnetic Resonance Imaging (JMR), Pre-print online on BioRxiv: https://doi.org/10.1101/2021.03.16.435723

Babak Moghadas[1], Vimala N. Bharadwaj[1], John P. Tobey[1], Yanqing Tian[2], Sarah E. Stabenfeldt[1] and, Vikram D. Kodibagkar[1*]

[1]School of Biological and Health Systems Engineering, Arizona State University

[2] Department of Materials Science and Engineering, Southern University of Science and Technology, Shenzhen, Guangdong, 518055, China

ABSTRACT:

Background: Brain tissue hypoxia is a common consequence of traumatic brain injury (TBI) due to the rupture of blood vessels during impact and it correlates with poor outcome.

Purpose: To investigate whether GdDO3NI , a nitroimidazole-based T_1 MRI contrast agent, allows imaging hypoxia in the injured brain after experimental TBI.

Study Type: Animal study.

Animal Model: TBI induced mice (controlled cortical impact model) were intravenously injected with either conventional T_1 agent (gadoteridol) or GdDO3NI at 0.3 mmol/kg dose (n=5 for each cohort) along with pimonidazole (60 mg/kg) at 1hr post injury.

Field Strength/Sequence: 7T/ T_2-wt fast spin echo and T_1-wt spin echo.

Assessment: Injured animals were imaged with T_2 weighted fast spin-echo sequence to estimate the extent of the injury. The mice were then were then imaged pre- and post-contrast using a T_1-weighted spin-echo sequence for 3hrs post contrast. Regions of interests were drawn on the brain injury region, the contralateral brain as well as on the cheek muscle

region for comparison of contrast kinetics. Brains were harvested immediately post imaging for immunohistochemical analysis.

Statistical Tests: One-way analysis of variance and two-sample *t*-tests were performed.

Results: GdDO3NI is retained in the injury region for up to 3 hours post-injection ($p < 0.05$ compared to gadoteridol) while it rapidly clears out of the muscle region. On the other hand, conventional MRI contrast agent gadoteridol clears out of both the injury region and muscle rapidly, although with a relatively more delayed wash out in the injury region than in muscle. Minimal contrast enhancement was seen for both agents in the contralateral hemisphere. Pimonidazole staining confirms the presence of hypoxia in both gadoteridol and GdDO3NI cohorts, and the later cohort shows good agreement with MRI contrast enhancement.

Data Conclusion: GdDO3NI was successfully shown to visualize hypoxia in the brain post-TBI using T1-wt MRI.

KEYWORDS: Hypoxia, Traumatic brain injury, GdDO3NI , Targeted contrast agent

APPENDIX B

EMERGING TRENDS IN MR BASE CELL LABELING AND TRACKING TECHNIQUES (IN PREPARATION)

Babak Moghadas[1], Vimala N. Bharadwaj[1], Vikram D. Kodibagkar[1,*]

[1]School of Biological and Health Systems Engineering at Arizona State University

Abstract:

Currently personalized treatment is one of the central topics in the medical and biomedical fields. Cellular therapy has shown promise in preclinical studies; however, translating the technics and knowledge from preclinical to clinical cases has not shown a very successful path. Efforts to address the issue have oriented towards the efficacy of cell delivery, migration of cells from the transplanted site, and survival of the transplanted cells. Exploiting noninvasive methods and techniques has always attracted researchers' attention in preclinical and clinical studies. Imaging as the first in the line, has helped scientists and researchers gather vital information without introducing new complications to patients. Magnetic resonance imaging (MRI) as the most versatile imaging technique with high resolution, which provides images laden with information serves as the first choice for evaluating the issues around cellular therapy. In this review, we briefly discuss cell labeling, different available MRI contrast agents and their merits and drawbacks based on the most recent developments and achievements in cellular MRI.

APPENDIX C

DFOBNI: AN IRON-BASED HYPOXIA TARGETING CONTRAST AGENT (IN PREPARATION)

Babak Moghadas[1], C. Chad Quarles and Vikram D. Kodibagkar[1*]

[1]School of Biological and Health Systems Engineering, Arizona State University

ABSTRACT:

Purpose: In this study, we synthesized, characterized and tested a novel hypoxia targeting contrast agent ferrioxamine B nitroimidazole (FOBNI) for imaging hypoxia using magnetic resonance imaging (MRI). The maps of hypoxic regions using FOBNI were evaluated by comparing them to the maps of the previously tested GdDO3NI contrast agent.

Methods: FOBNI was synthesized and purified using reversed phase chromatography. After acquiring cytotoxicity data, the magnetic properties were studied to measure the relaxivity of the contrast agent. The relaxivity experiment was performed in a custom phantom containing nine different concentrations of the agent. MR studies were conducted in at 7T field. The ability of the contrast agent in targeting hypoxic regions was studied in vitro with 3D cell structures under low levels of oxygen.

Results: The synthesis was validated by the NMR spectrum of the compound along with mass spectroscopy. The cytotoxic assay showed no significant changes to the cells' viability over the period of 8h exposure to the contrast agent. FOBNI retention in the hypoxic condition is an indication of its performance under the proposed mechanism. The result was in good agreement with the data collected from GdDO3NI group.

Conclusion: FOBNI was successfully synthesized as a small molecular MR contrast agent and showed high T_2 relaxivity and the ability to target hypoxia.

KEYWORDS: HYPOXIA, MRI, CONTRAST AGENT, Iron-based contrast agent, DFOB, DFOBNI

APPENDIX D

QUANTITATIVE MAPPING OF BRAIN TISSUE OXYGENATION AROUND NEURAL INTERFACES (IN PREPARATION)

Babak Moghadas[1], Livia De Mesquita Teixeira[1], Arati Sridharan[1], Yuka Sugamura[1], Jitendran Muthuswamy[1], and Vikram D. Kodibagkar[1, *]

[1]School of Biological and Health Systems Engineering at Arizona State University

ABSTRACT:

The ability to spatially map the pO_2 levels around chronically implanted neural interfaces can help assess their impact on surrounding tissue. Here, by applying Proton Imaging of Siloxanes to map Tissue Oxygenation Levels (PISTOL) approach, we successfully achieved a sensitive and quantitative spatial mapping of pO_2 around neural interfaces. Tetradecamethylhexasiloxane (L6) is identified and characterized as a MR pO_2 probe. The spin-lattice relaxation rate, R_1 of L6, showed a linear dependence on pO_2 levels. *In vivo* studies were conducted by implanting L6 soaked polydimethylsiloxane (PDMS) coated electrode arrays in mice brains. Tissue pO_2 in response to air and oxygen breathing was successfully measured from around implanted electrodes. This novel technique is a valuable tool to investigate pO_2 levels around implanted neural interfaces, which could aid the assessment of changes that may occur at the recording site. Future studies will combine single-unit electrophysiology with quantitative, high-resolution spatial maps of pO_2 levels *in vivo*.

KEYWORDS: Oximetry, Oxygen tension, Brain, Neural implants, ^{1}H MRI, Tetradecamethylhexasiloxane, L6

APPENDIX E

MAPPING HYPOXIA IN BRAIN TUMORS USING GDDO3NI : VALIDATION WITH PET AND IHC (IN PREPARATION)

Babak Moghadas[1], Matthew Scarpelli[2], Christopher Rock[1], Alberto Fuentes[2], Debbie Healey[2], Chad Quarles[2], and Vikram D. Kodibagkar[1,*]

[1] School of Biological and Health Systems Engineering at Arizona State University

[2] Barrow Neurological Institute, St. Joseph's Hospital and Medical Center

ABSTRACT

In this study we have used the hypoxia-targeting MRI contrast agent GdDO3NI , (a nitroimidazole-based T1 contrast agent) to image the development of hypoxia in rodent brain tumors at two different sizes. Our results indicate a range of signal enhancements from 5-20% over baseline in the 9L tumor using GdDO3NI with clearance from the contralateral brain and muscle tissue. Furthermore, the GdDO3NI enhancement correlates with PET imaging using hypoxia targeting ^{18}F-FMISO and immunohistochemistry based on pimonidazole. This study further demonstrates the utility of GdDO3NI in non-invasive imaging of tissue hypoxia with high resolution. The pharmacokinetic parameters are calculated for the hypoxia targeting contrast agent to enhance the understanding of tumor microenvironment.